The refractive index of single aerosol particles: Measurements and models

Alison Bain

A thesis submitted to McGill University
in partial fulfillment of the requirements for the degree of
Doctor of Philosophy

Department of Chemistry, McGill University
Montreal, Quebec, Canada
April 2021

Abstract

Aerosol is ubiquitous in our atmosphere, yet it still poses great uncertainty to radiative forcing and climate models. Central to accurate predictions of aerosol radiative forcing is an accurate description of the scattering and absorption of solar radiation by aerosol, which can be described by the complex refractive index. The refractive index of aerosol depends on the wavelength of incident light and the temperature as well as its chemical composition. In the atmosphere, aerosol may contain a number of different organic and inorganic components. Furthermore, as aerosol is transported though the atmosphere and encounters air of varying relative humidity its water content will change to remain at equilibrium with its surroundings. All of these factors must be taken into consideration in order to accurately determine the refractive index of atmospheric aerosol.

The refractive index of single, optically trapped particles can be determined through the collection and fitting of Mie scattered light. By monitoring optically trapped particles it is possible to mimic atmospheric conditions. Importantly for investigating the refractive index of aerosol, single particle experiments allow for the characterization of supersaturated states not accessible through bulk measurements. Throughout this thesis, the refractive indices of various aerosol types are determined using optical trapping methods.

First, in order to find the most accurate method of determining the refractive index of aerosol, retrieval using the morphology-dependent resonances in the Mie scattering spectrum is compared to phase function fitting. Using the morphology-dependent resonances is found to be more accurate and less computationally demanding than phase function fitting.

Morphology-dependent resonances and the Mie scattering spectrum are then used throughout the rest of this thesis to determine the optical properties of aerosol.

Next, the optical properties of absorbing particles are investigated. Single, absorbing particles are held in a photophoretic trap, illuminated with a broadband light source and the broadband Mie scattering spectrum is collected. Here, the full Mie scattering spectrum is fit using Lorentzian oscillators to describe the absorption features observed as scattering minima in the spectra. Using the causal relationship between the real and imaginary parts of the refractive index described by the Kramers-Kronig relation, the wavelength-dependent complex refractive index is determined for these particles.

The complex refractive index of weakly absorbing particles is then considered. Using cavity-enhanced Raman spectroscopy, while slowly heating the particle by increasing the trapping beam power, both the real and imaginary parts of the refractive index of several aqueous solutions whose optical properties are relevant to aqueous sea-salt particles and aqueous organic aerosol are measured. The far-UV transitions that give rise to the refractive index in the visible region for weak absorbers is modeled with an effective Lorentzian oscillator. The effective oscillator model accurately describes both the real and imaginary parts of the refractive index of aqueous solutions across a wide range of water activities and optical wavelengths. It is shown that mixing rule calculations utilizing oscillator parameters from solutions containing a single solute and water can be used to predict the optical properties of aqueous solutions containing multiple solutes.

Finally, this model is extended to consider the contributions of individual ions to the refractive index of aerosol. Since the absorption of weakly absorbing aerosol is small and is

often neglected, broadband scattering is utilized to determine only the real part of the refractive index. The oscillator parameters determined for ions accurately predict the refractive index as a function of both water content and wavelength for aqueous salts and strong acids. Furthermore, the refractive index of ternary organic-inorganic mixtures using these oscillator parameters agree with experimentally determined refractive indices. In addition, the effect of temperature on the refractive index within the framework of the effective oscillator model is also explored.

Résumé

Les aérosols sont omniprésents dans l'atmosphère, mais ils posent toujours une grande incertitude pour le forçage radiatif et les modèles climatiques. Une description précise de la diffusion et de l'absorption du rayonnement solaire par les aérosols, qui peuvent être décrites par l'indice de réfraction complexe, est au cœur des prévisions précises du forçage radiatif des aérosols. L'indice de réfraction de l'aérosol dépend de sa composition chimique, de la longueur d'onde de la lumière incidente, ainsi que de la température. Dans l'atmosphère, l'aérosol peut contenir plusieurs composants organiques et inorganiques différents. De plus, au fur et à mesure que l'aérosol est transporté à travers l'atmosphère et qu'il rencontre de l'air dont l'humidité relative varie, sa teneur en eau changera pour rester en équilibre avec l'air ambiant. Tous ces facteurs doivent être pris en considération afin de déterminer avec précision l'indice de réfraction des aérosols atmosphériques.

Des particules uniques peuvent être piégées optiquement, et leur indice de réfraction déterminé par la collecte et l'ajustement de leur diffusion Mie. En surveillant les particules optiquement piégées, il est possible d'imiter les conditions atmosphériques. De grande importance pour l'étude des indices de réfraction des aérosols, les expériences sur une seule particule permettent de caractériser les états sursaturés non accessibles par des méthodes traditionnelles. Tout au long de cette thèse, l'indice de réfraction de différents types d'aérosols

Tout d'abord, deux méthodes - extraction en utilisant les résonances dépendantes de la morphologie dans le spectre de diffusion de Mie ainsi que l'ajustement de la fonction de phase - ont été comparées pour identifier celle qui permet une détermination plus précise de l'indice de réfraction de l'aérosol. L'utilisation des résonances dépendantes de la morphologie

s'avère plus précise et moins exigeante en termes de calcul que l'ajustement de fonction de phase. Les résonances dépendantes de la morphologie et le spectre de diffusion de Mie sont donc utilisés tout au long de cette thèse pour déterminer les propriétés optiques de l'aérosol.

Les propriétés optiques des particules absorbantes ont ensuite été étudiées. Des particules absorbantes uniques sont maintenues dans un piège photophorétique, éclairées avec une source de lumière à large bande et le spectre de diffusion Mie à large bande est collecté. Ici, le spectre de diffusion Mie complet est ajusté à l'aide d'oscillateurs lorentziens afin de décrire les caractéristiques d'absorption observées comme des minima de diffusion dans les spectres. En utilisant la relation causale entre les parties réelle et imaginaire de l'indice de réfraction, comme décrite par la relation de Kramers-Kronig, l'indice de réfraction complexe dépendant de la longueur d'onde est déterminé pour ces particules.

L'indice de réfraction complexe des particules faiblement absorbantes est alors considéré. Particulièrement, plusieurs solutions aqueuses dont les propriétés optiques sont pertinentes pour les particules aqueuses de sel marin et l'aérosol organique aqueux sont étudiées. Les parties réelles et imaginaires de l'indice de réfraction de ces solutions sont mesurées en utilisant la spectroscopie Raman améliorée par cavité, tout en chauffant lentement les particules en augmentant la puissance du faisceau de piégeage. Les transitions UV lointaines qui donnent lieu à l'indice de réfraction dans la région visible pour les absorbeurs faibles sont modélisées avec un oscillateur Lorentzien efficace. Le modèle d'oscillateur efficace décrit avec précision les parties réelles et imaginaires de l'indice de réfraction des solutions aqueuses sur une large gamme d'activités de l'eau et de longueurs d'onde optiques. Il est montré que les propriétés optiques des solutions aqueuses contenant plusieurs solutés peuvent être prédites en utilisant

une combinaison linéaire d'oscillateurs à partir de solutions aqueuses d'un seul soluté.

Enfin, ce modèle est étendu pour prendre en compte les contributions des ions individuels à l'indice de réfraction des aérosols. Étant donné que l'absorption de l'aérosol faiblement absorbant est faible et souvent négligée, la diffusion à large bande est utilisée pour déterminer uniquement la partie réelle de l'indice de réfraction. Les paramètres de l'oscillateur déterminés pour les ions prédisent avec précision l'indice de réfraction en fonction à la fois de la teneur en eau et de la longueur d'onde des sels aqueux et des acides forts. De plus, l'indice de réfraction des mélanges ternaires organiques-inorganiques déterminé en utilisant ces paramètres d'oscillateur est en accord avec les indices de réfraction déterminés expérimentalement. En outre, l'effet de la température sur l'indice de réfraction dans le cadre du modèle d'oscillateur est également étudié.

Acknowledgments

There are countless people who have helped and encouraged me over these past five years at McGill and without them I can confidently say, I would not have ever made it to the finish line. For their help in the design, construction and maintenance of aerosol trapping cells and heat sinks, I would like to thank Jean-Philippe Guay and Pascal Bourseguin from the chemistry and physics machine shops. I would also like to thank Richard Rossi and Weinhua Wang from the electronics shop for their help fixing RH sensors and input on power conversion for one of the nebulizers used in some experiments. All of these people were of great help in building and maintaining the experimental setups used throughout this thesis.

I would like to thank Chantal Marotte, the graduate program administrator, who always had the answer when trying to navigate funding applications, registering for courses and anything and everything else related to graduate studies in chemistry at McGill. On more than one occasion Chantal was there to talk it seemed like everything was going wrong and I am grateful for her advice and words of encouragement.

I would like to thank the members of my group at McGill both past and present; Aidan Rafferty, Brandon Wallace, Benjamin Vennes, Alex Logozzo and Dr. Kyle Gorkowski, for their helpful discussion and for contributing to a friendly work environment. I would especially like to thank Aidan Rafferty for his help in data collection for the work discussed in Chapter 2 and 4, for the building and maintaining of the dual-beam optical setup used in much of this work, and proof reading the work in this thesis as well as presentations and applications I wrote along the way. Aidan was also always willing to offers his expertise or

let me bounce ideas off him when I could not get my experiment or analysis to work.

There are also a number of graduate students in the department of chemistry who offered me their help over the past five years. I would like to thank Dr. Samantha Gateman for her willingness to edit abstracts and proposals and her help with optical microscopy; Aya Sakaya for her help in proofreading french translations and her UV-vis and fluorescence expertise; Dr. Lisa Stephens for lending her expertise in image analysis with MATLAB; and Tristan Borchers for his willingness to share hardware, chemicals and instruments.

I would like to thank my family for their continued support over my academic career, especially my father for blindly believing I could achieve my goal of a PhD and insisting that every setback was only minor.

I would like to thank my review committee members Prof. Amy Blum and Prof. Christopher Barrett, for their encouragement and willingness to help me over the course of my PhD.

Finally, I would like to thank my supervisor, Prof. Thomas Preston, for all his support over the past five years. I appreciate the opportunity he gave me to learn something completely new, as well as the freedom he gave me to run with my own ideas. Prof. Preston was always happy to support my applications for funding and gave me many opportunities to present my research. With his guidance, I have become a more confident scientist and I am grateful for his tuition.

Contribution to original knowledge

Throughout this thesis, the refractive index (RI) of aerosol is explored, first through a comparison of methods for determining the RI of single particles, then through a collection and modeling of RI data. In Chapter 2 we present an algorithm for fitting the 2D phase function to determine the RI and size of a single particle. We also compare the accuracy of this fitting algorithm to a 1D phase function fitting algorithm and fitting morphology dependent resonances in cavity-enhanced Raman spectra. This is the only such comparison of fitting algorithms in the literature.

In Chapter 3 we present the first example in the literature of collecting Mie scattering spectra for particles which have strong absorption bands in the scattering spectrum. For these particles, we provide a method to determine both the size and complex RI.

In Chapter 4 we present a model to determine the complex RI of weakly absorbing aerosol using an effective Lorentzian oscillator to model the core electron transitions of the solute and the known complex RI of water. This is the first model to determine the real and imaginary components of the RI over the full visible spectrum and range of aerosol water contents in the literature. This model, based on electronic transitions, is a great improvement over the empirical parameterizations used to determine the real part of the RI over the visible spectrum currently available in the literature.

In Chapter 5 we extend on the work in Chapter 4 to determine the RI of a aqueous mixture using an effective oscillator for individual ions in solution. This is a substantial improvement to other RI models as ambient aerosol characterization yields the fraction of each ion present, making this model employable for climate modeling. Additionally, we have

provided oscillator parameters to model the RI as a function of water content and visible wavelength for a number of weakly absorbing organic solutes previously unavailable in the literature.

Contents

List of Figures

List of Tables

List of abbreviations

Table 1: Abbreviations used throughout this thesis.

Abbreviation	Full Name
1D	One-dimensional
2D	Two-dimensional
3D	Three-dimensional
AAC	Absorption Ångstrom coefficient
ATR-FUV	Attenuated total reflection far-UV
CERS	Cavity-enhanced Raman spectroscopy
CFC	Chlorofluorocarbons
CRDS	Cavity ring down spectroscopy
DM	Dichroic mirror
EDB	Electrodynamic balance
FWHM	Full-width at half-maximum
GLMT	Generalized Lorenz-Mie theory
IR	Infrared
RFE	Radiative forcing efficiency
RH	Relative humidity
RI	Refractive index
MDR	Morphology dependent resonance
NA	Numerical aperture
NIR	Near infrared
SOA	Secondary organic aerosol
TE	Transverse electric
TM	Transverse magnetic
UV	Ultraviolet

Table 1: Continued.

Abbreviation	Full Name
VOC	Volatile organic compound
WGM	Whispering gallery mode

Contributions

Chapter 2 author contributions

Chapter 2 was reproduced from Alison Bain, Aidan Rafferty and Thomas C. Preston, Determining the size and refractive index of single aerosol particles using angular light scattering and Mie resonances, *J. Quant. Spectrosc. Rad. Transf.* (2018) 221, 61-70. Aidan Rafferty performed all experimental measurements. I analyzed experimental data and interpreted results with the help of Dr. Preston. Dr. Preston wrote the fitting algorithms used to determine the size and refractive index of single particles. Figures were created by myself and Dr. Preston. Dr. Preston and I jointly wrote the manuscript. Aidan Rafferty contributed to editing the manuscript.

Chapter 3 author contributions

Chapter 3 was reproduced from Alison Bain and Thomas C. Preston, Mie scattering from strongly absorbing airborne particles in a photophoretic trap, *J. Appl. Phys.* (2019) 125, 093101. I built the experimental setup and performed all of the experiments. I analyzed all experimental results. Dr. Preston wrote code to model the complex refractive index of strongly absorbing particles used in analysis and performed theoretical calculations describing the impact of absorption on the Mie resonance spectrum. The manuscript was written and the figures were made jointly by myself and Dr. Preston.

Chapter 4 author contributions

Chapter 4 was reproduced with the permission of John Wiley and Sons from Alison Bain, Aidan Rafferty and Thomas C. Preston, The wavelength-dependent complex refractive index of hygroscopic aerosol particles and other aqueous media: An effective oscillator model, *Geophys. Res. Lett.* (2019) 46, 10636 – 10645. Experiments were performed by myself and Aidan Rafferty. Data analysis was performed by Dr. Preston and myself. The code used to fit experimental data determine oscillator parameters was written by Dr. Preston. The manuscript was written and the figures were made by myself and Dr. Preston. Aidan Rafferty contributed to editing the manuscript.

Chapter 5 author contributions

Chapter 5 was republished with permission of the Royal Society of Chemistry from Alison Bain and Thomas C. Preston, The wavelength-dependent optical properties of weakly absorbing aqueous aerosol particles, *Chem. Comm.*, 2020, 56, 8928 - 8931. Permission conveyed through Copyright Clearance Center,Inc. I performed all experiments. Data analysis was performed by myself and Dr. Preston. The manuscript was written by me and edited with the help of Dr. Preston. The figures were made by myself and Dr. Preston.

Thesis outline

The work in this thesis aims to characterize the refractive index of single particles and provide models for the refractive index of aerosol as a function of atmospherically relevant parameters such as frequency, aerosol water content and temperature. Chapter 1 introduces the necessary background for this work and discusses the importance of accurate models for aerosol refractive index. In Chapter 2, the accuracy of three refractive index and radius retrieval methods based on Mie scattering are compared in order to determine the best method for determining the refractive index of optically trapped particles.

Once the most accurate method for retrieval is determined, in Chapter 3, the broadband Mie scattering spectrum is used to determine the refractive index of microbeads which absorb in the visible region. Photophoretic trapping and broadband Mie scattering are combined to, for the first time, characterize the wavelength-dependent complex refractive index of single, strongly absorbing particles. A model for the imaginary component of the refractive index using Lorentzian oscillators to describe absorption bands in the visible region and an offset to account for transitions in the far-UV is introduced. Employing the Kramers-Kronig transform, an equation for the real part of the refractive index is generated. Mie scattering spectra are fit with this model to determine the Lorentzian oscillator parameters describing the absorption bands, yielding equations for the complex refractive index. It is shown that the model developed here can be used to accurately determine the size and refractive index of particles with strong absorption bands in the visible region.

In Chapter 4, the model is extended to weakly absorbing particles. A single, effective

Lorentzian oscillator is now used to model the far-UV transitions. Again, applying the Kramers-Kronig transform, an equation is determined for both the real and imaginary parts of the refractive index. It is shown that with the oscillator parameters retrieved from particles containing a single solute in water, the refractive index of ternary mixtures can accurately be predicted. In Chapter 5, the oscillator model is further extended to predict the refractive index of a solution using mass fractions of individual ions. The effect of temperature on the effective oscillator is also investigated by fitting temperature-dependent refractive index data found in the literature. Finally, Chapter 6 concludes the work in this thesis and provides insight into future work.

Chapter 1

Introduction

1.1 Atmospheric aerosol

Aerosol is a ubiquitous component of our atmosphere. It can be found over every continent and ocean, and exists both at the surface and high in the troposphere.[1,2] Atmospheric aerosol refers to particles suspended in the atmosphere. These particles can be in the liquid or solid phase and range in size from tens of nanometers to several microns.[2–4] Solid particles can take on complex geometries, but liquid particles are spherical.[5,6]

There are many sources of atmospheric aerosol. Primary aerosol is emitted directly into the atmosphere (e.g. volcanic ash emissions, sea spray, and soot from biomass burning). Additionally, aerosol can be formed from semi-volatile organic molecules present in the atmosphere (e.g. terpenes emitted by trees). These molecules can be oxidized in the gas phase by atmospheric oxidants, such as ozone and the hydroxyl radical, leading to reduced volatility. The lower volatility products then condense, often onto seed particles already suspended in the atmosphere. Aerosol formed by this process is termed secondary organic aerosol (SOA).[7–10] Both primary aerosol and SOA can be anthropogenic or biogenic in origin.

Aerosol near the surface contributes to haze in polluted environments, which both decreases visibility and has been found to cause adverse health effects.[11–14] Aerosol also impacts our climate through interactions with sunlight and clouds. These impacts are categorized into direct and indirect effects.[4,7]

1.1.1 Aerosol direct and indirect effects

The direct effect of aerosol on our climate comes from its interactions with solar radiation. Scattering and absorption cross-sections depend on chemical composition as well as particle size and shape. The scattering of electromagnetic radiation leads to a net cooling effect as light that would have travelled to Earth's surface can now be scattered back to space. In contrast, absorption by aerosol leads to warming.[4,7,15] Much of the aerosol in the atmosphere predominantly scatters radiation and is considered weakly absorbing, leading to a net cooling of our climate. However, absorption by brown and black carbon cannot be neglected and has a warming effect that may completely counteract the cooling effect in some regions.[16,17]

Aerosol radiative forcing

Radiative forcing describes the energy transfer between the Sun and Earth and is used in climate modeling to predict how changes in gas concentrations or aerosol distributions affect the climate. Radiative forcing efficiency (RFE) is often used to predict the direct impact of aerosol on radiative forcing through the equation[18,19]

$$\mathrm{RFE} = \mathrm{SD}(1-\mathrm{A_{cld}})\mathrm{T_{atm}^2}(1-\mathrm{R_{sfc}})^2\left[2\mathrm{R_{sfc}}\frac{1-\omega}{(1-\mathrm{R_{sfc}})^2}-\beta\omega\right]. \tag{1.1}$$

RFE has dimensions of power per length squared (e.g. $\mathrm{W/m^2}$ in SI units). Many of the terms required to calculate the RFE are set as constants; S is the solar constant, D is the fractional day length, $\mathrm{A_{cld}}$ is the fractional cloud cover, $\mathrm{T_{atm}}$ is the solar atmospheric transmittance

and R_{sfc} is the surface albedo. Only β, the upscatter fraction, and ω, the single scattering albedo, depend on aerosol properties.

The fraction of light scattered upwards depends on the angular scattering pattern, and requires knowledge of the complex refractive index (RI) and the distribution in size parameter,[18,19] the latter of which is defined as[20]

$$x = \frac{2\pi r}{\lambda}, \tag{1.2}$$

where r is the particle radius and λ is the incident wavelength. The single scattering albedo is the ratio of the scattering efficiency and the extinction efficiency (i.e. the sum of the scattering and absorption efficiencies), and again requires knowledge of the complex RI and range in size parameter.[21]

Positive RFE values indicate an increase in upward scattering due to the presence of aerosol (resulting in cooling) while negative values indicate a decrease in upward scattering (resulting in warming).[19] For hygroscopic particles, size and composition are highly dependent on the ambient relative humidity (RH). Since a change in particle composition leads to a change in RI, radiative forcing will also be highly dependent on RH. For example, Pilinis *et al.* found an increase in the RFE of a factor of 2.1 for $(NH_4)_2SO_4$ aerosol when the RH was increased from 40 to 80%.[22]

The effect of uncertainties and inaccuracies in the RI on RFE have been investigated for $(NH_4)_2SO_4$ aerosol.[18,19,23,24] The simplest method for predicting the real part of the RI of an aqueous mixture is a volume mixing rule using the RI of pure water and pure solid solute

components. This approach can result in inaccurate RIs, as the RI of a solid and a solvated solid are not the same.[25] Fig. 1.1, reproduced from Erlick *et al.*,[19] highlights this point. They compare the RI determined by the volume mixing rule to a molar refraction mixing rule from the Lorentz-Lorenz equation to experimental data from the CRC handbook[26] and the parameterization from Tang and Munkelwitz[27] for aqueous $(NH_4)_2SO_4$ solutions at $\lambda = 633$ nm. Fig. 1.1 shows that the volume mixing rule is inaccurate over most of the mass fraction range considered, with errors of more than 0.01 RI units at high solute mass fractions. In contrast, the molar refraction mixing rule closely agrees with both the parameterization from Tang and Munkelwitz[27] and the experimental data from the CRC handbook.[26]

Erlick *et al.* go on to calculate the RFE at 550 nm for $(NH_4)_2SO_4$ particles for RHs between 37 – 99% RH.[19] They find that the volume fraction mixing rule underpredicts the RFE by up to 0.42 W/m^2 at 37% RH and over predicts by up to 0.24 W/m^2 at 90% RH while being accurate at 70 and 99.9% RH.[19]

It is clear that accurate predictions of aerosol radiative forcing rely heavily on accurate knowledge of aerosol RI. In fact, Zarzana *et al.* found that errors in the real part of the RI should be less than 0.003 for $(NH_4)_2SO_4$ aerosol in order to obtain errors of less than 1% in RFE.[23] As will be discussed in Section 1.2, there are few high quality RI parameterizations for atmospherically relevant solutes over the full solar spectrum and range of water activities experienced by aerosol in the atmosphere. This makes accurate RFE predictions challenging or impossible for many aerosol compositions.

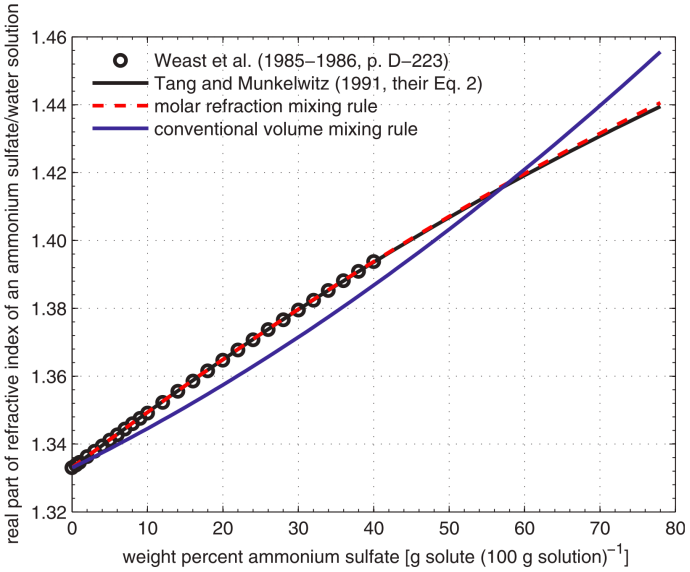

Figure 1.1: Real part of the refractive index at 633 nm of a solution of $(NH_4)_2SO_4$ with water as a function of the mass fraction of $(NH_4)_2SO_4$. The open black circles are data from Weast *et al.* (1985, p. D-223).[26] The solid black line is the parametric formula of Tang and Munkelwitz[27] based on their empirical results for supersaturated solutions. The dashed red line is the molar refraction mixing rule. The solid blue line is the conventional volume mixing rule. Reproduced from Erlick, C., Abbatt, J. P. D., & Rudich, Y. (2011). How different calculations of the refractive index affect estimates of the RFE of ammonium sulfate aerosols. *Journal of the Atmospheric Sciences*, 68(9), 1845–1852. ©American Meteorological Society. Used with permission.

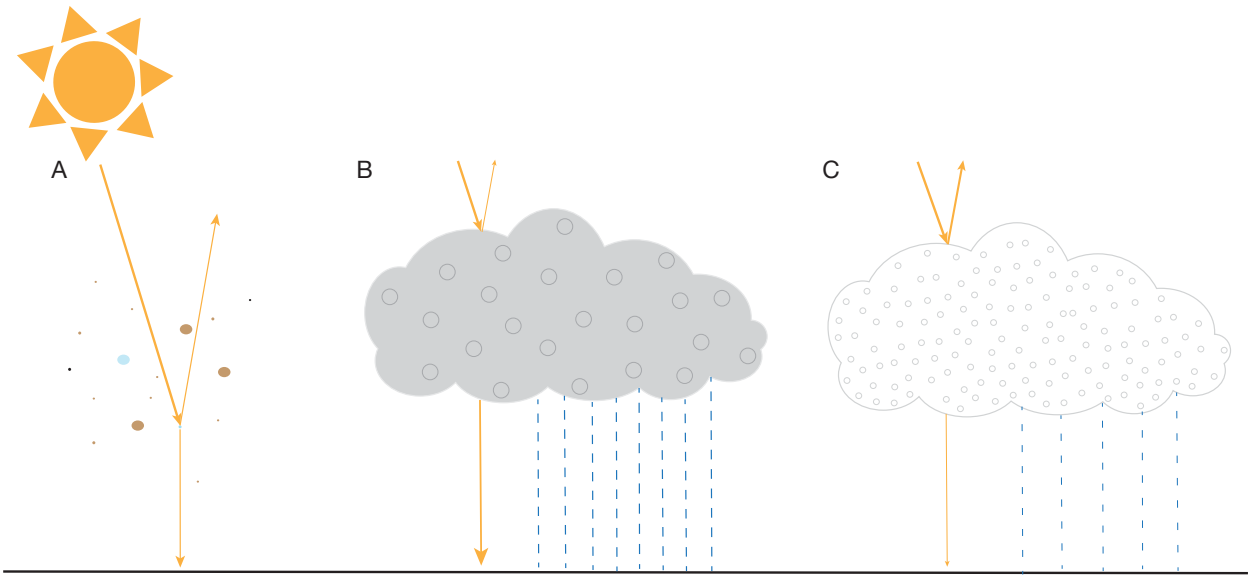

Figure 1.2: A) Aerosol particles scatter and absorb solar radiation. B) Cloud without the presence of aerosol having large cloud droplets. C) Cloud formed in the presence of aerosol having more numerous, smaller cloud droplets leading to increased cloud reflectively and decreased precipitation.

Aerosol indirect effects

Aerosol can also affect the climate through mechanisms that are referred to as being indirect. For example, clouds formed in clean air or high aerosol concentration conditions will contain different numbers and sizes of cloud droplets. These changes, in turn, affect cloud reflectivity as well as cloud lifetime and precipitation[7] as shown in the schematic in Fig. 1.2. Further, aerosol which is no longer suspended in the atmosphere, but has deposited onto the surface, can still alter the climate. For instance, strongly absorbing soot deposits on ice pack and snow greatly decreases surface albedo.[4,15] Unlike the impact of gases such as chlorofluorocarbons (CFCs),[28] CO_2[29] and CH_4[30] on our atmosphere and climate, the complexity of aerosol-climate interactions leave much uncertainty surrounding aerosol's impact.[31]

1.1.2 Composition of aerosol

Ambient aerosol is a complex mixture of both organic and inorganic components. The physical properties of aerosol are dynamic as its composition changes with aging processes (oxidation by O_3 and OH radicals as well as photochemical processes).[32–34] Aerosol water content also changes during its atmospheric lifetime of a few days to a few weeks, as aerosol is transported through air of varying temperature and RH.[35]

The components of aerosol are also highly dependent on their source. Biogenic aerosol formed over forests contains many complex organic molecules which readily undergo oxidation,[36,37] while aerosol generated from dust storms in desert regions and by wind erosion of soil may contain iron complexes.[38] Additionally, wave breaks generate sea spray aerosol which contains mostly sea salt but also bacteria, algae and other dissolved organic material.[39] Moreover, aerosol originating from anthropogenic sources, such as industrial or agricultural activity, can have high concentrations of SO_4^{2-} and NH_4^+.[40]

Aerosol from different sources can become mixed over its atmospheric lifetime as it is transported through the atmosphere.[2] Mixing may be external, where aerosol particles in a population have different compositions, or internal, where the contents of aerosol particles become mixed.[41] Fig. 1.3 shows a schematic of different aerosol mixing types. It is important to note that properties such as water uptake and light scattering of internally and externally mixed aerosol, even with the same mass fraction of each component overall, will not be identical.[42]

Internally mixed aerosol can exist in many different phases depending on composition

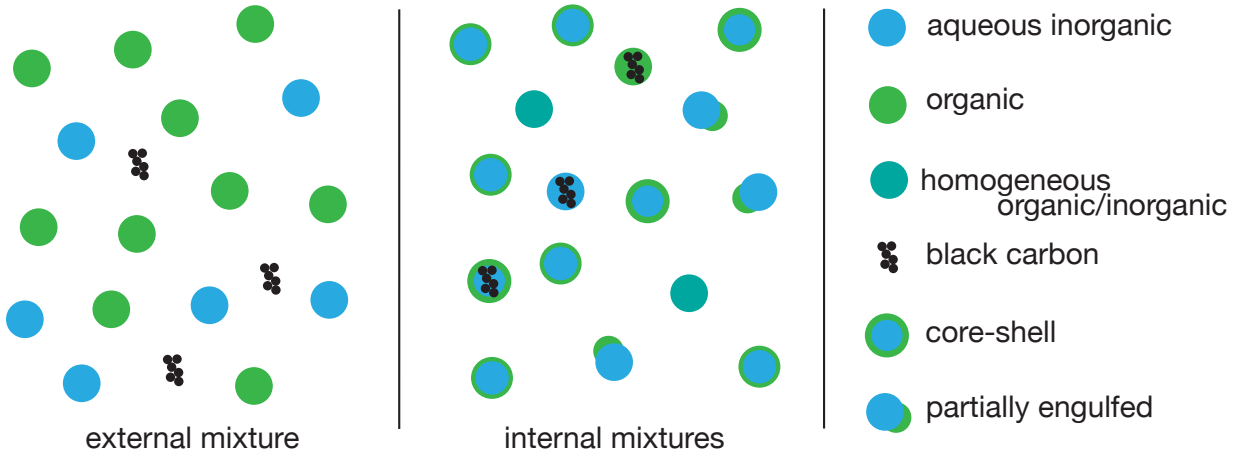

Figure 1.3: Schematic of an external mixture of aqueous inorganic, organic and black carbon aerosol and internal mixtures of these components mixed homogeneously, with solid inclusions and having core-shell and partially engulfed morphologies.

(e.g. homogeneously mixed, phase separate into core-shell particles or containing solid inclusions). Examples of these internally mixed aerosol types are shown in Fig. 1.3. Core-shell particles are the focus of many active investigations that aim to determine when these phase transitions occur, and how this alters aerosol properties such as mass transport and surface tension.[34,43–46] This is, however, beyond the scope of this thesis. Here, only the case of homogeneously mixed particles is considered.

Sea spray is one of the most abundant types of aerosol in the atmosphere.[39] Due to the hygroscopic nature of inorganic salt, sea spray aerosol undergoes large changes in size and optical properties with varying RH. Over 99% of sea salt by mass is made up of only seven ions, with Cl^- and Na^+ being the most dominant components. Table 1.1 shows the mass percentages of the seven most abundant ions in sea salt.

Atmospheric aerosol containing inorganic salts may exist in supersaturated states. The

Table 1.1: Mass percentages for most abundant sea salt components[4]

Species	Mass Percent (%)
Cl^-	55.04
Na^+	30.61
SO_4^{2-}	7.68
Mg^+	3.69
Ca^+	1.16
K^+	1.10
Br^-	0.19

supersaturated state lies between the deliquescence and efflorescence points.[47] The deliquescence point is the RH where a dry particle will begin to take up water from the surrounding air if the RH around a trapped particle is slowly increased.[48] Conversely, the efflorescence point is the RH where an aqueous particle suddenly loses all of its water as the ambient RH is slowly decreased.[49] Different solutes have unique efflorescence and deliquescence points and a number of salts undergo hysteresis in their hydration and drying curves.[48] However, not all hygroscopic solutes undergo efflorescence and deliquescence. For example, aqueous sugar particles and other highly soluble organics retain some moisture below 5% RH.[50,51]

Fig. 1.4 shows the hydration (blue points) and dehydration (red points) for $(NH_4)_2SO_4$ determined by Estillore *et al.*[47] It is common to plot growth factor, the ratio of dry diameter (D_0) to the diameter of the particle at a given RH (D_p) as a function of RH. Fig. 1.4 shows the supersaturated region for $(NH_4)_2SO_4$ between approximately 40–80% RH.

There is also a substantial fraction of organic components in ambient aerosol. More than 10,000 unique organic molecules have been identified in ambient aerosol.[52] Understanding

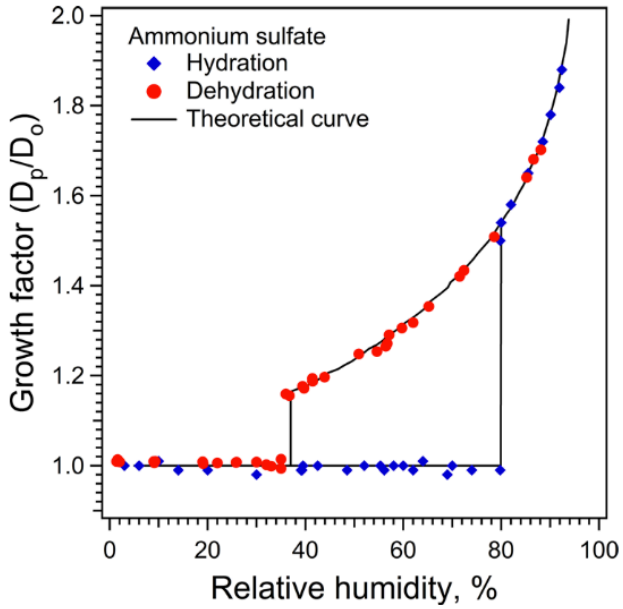

Figure 1.4: Hydration and dehydration curves for $(NH_4)_2SO_4$ aerosol particles with D_0 = 100 nm as a function of RH. Reprinted with permission from Estillore, A. D., Hettiyadura, A. P. S., Qin, Z., Leckrone, E., Wombacher, B., Humphry, T., Stone, E. A., Grassian, V. H. (2016). Water Uptake and Hygroscopic Growth of Organosulfate Aerosol. *Environmental Science and Technology*, 50(8), 4259–4268. Copyright 2016 American Chemical Society.

how each of these individual molecules affects the physical properties of aerosol is currently an insurmountable task. To address this problem, the aerosol community often uses predictors such as functional groups, molecular mass, double bond equivalent and ratios of atoms (e.g. O:C, H:C which are the ratios of oxygen to carbon and hydrogen to carbon atoms in a molecule, respectively) to categorize organic molecules and find trends in their physical properties (e.g. hygroscopicity, viscosity, glass transition temperature and optical properties).[25,33,52–56] These predictors can be determined from mass spectrometry measurements which are routinely preformed both on ambient aerosol and aerosol created in the lab.[57]

Some organic components are more prevalent in ambient aerosol than others. Aerosol physical chemists often use these, along with a number of model systems, when studying aerosol in the lab setting. One of the most abundant organic aerosol components, often found in large abundances during field campaigns, is levoglucosan, which is formed from the pyrolysis of carbohydrates.[58,59] Another common model system is sucrose, which is also produced from biomass burning.[60] Unlike levoglucosan, sucrose is a dimer and is a good surrogate for highly viscous and glassy aerosol.[50,61] Furthermore, citric and tartaric acids are commonly used in the lab-based studies as proxies for aged organics due to their high O:C ratios, water solubility and low volatility.[58] Fig. 1.5 shows the structures for these organic model systems.

Laboratory aerosol measurements performed with model systems (e.g. a single solute with water) do not capture the complexity of atmospheric aerosol.[55] Recently, effort has been made to study ternary aerosol systems consisting of water and two solutes, especially those consisting of both inorganic and organic components.[16,58,62–71] The work in Chapters

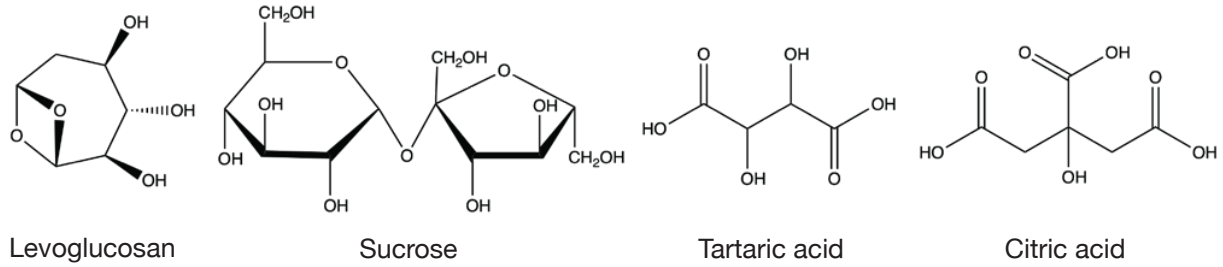

Figure 1.5: Chemical structures for model systems and abundant organic aerosol components.

4 and 5 investigates the optical properties of ternary aerosol, including organic-inorganic mixtures.

Multicomponent aerosol and mixing rules

Models for determining the properties of multisolute aerosol usually rely on bulk phase mixing rules (e.g. mole, mass or volume fraction combinations of single solute properties).[58,63,70] These mixing rules have been applied to many aerosol properties including hygroscopicity,[72] viscosity[54] and density,[73,74] as well as optical properties.[62] For optical properties, the molar refraction mixing rule,

$$R = \sum R_i x_i, \tag{1.3}$$

is often used, where R is the molar refraction of the solution and R_i is the partial molar refraction and x_i is the mole fraction for the ith component of the solution. Mixing rules, such as the one given in Eq. 1.3, assume that solutions remain ideal upon mixing. Although aerosol is not always an ideal solution, these mixing rules have been found to satisfactorily describe many aerosol properties.[54,62,73,74]

In Chapter 4 weighted densities are used as the densities of many aqueous solutions are nearly linear with respect to solute mass fraction. Throughout this work, the density of an aqueous solution will often be determined by fitting density data from the CRC handbook[75] as a function of mass fraction to a third-order polynomial. The density of multicomponent aerosol containing water can be found with a mole fraction weighting of binary solution densities.[74]

1.1.3 Water activity

At high RH, aerosol particles, especially those containing large concentrations of inorganic salts, take up water. When an aqueous spherical aerosol particle is in equilibrium with the surrounding RH, the water activity throughout the particle, a_w, will be related to the RH through

$$a_w \exp\left(\frac{2\sigma V_w}{rRT}\right) = \frac{\text{RH}}{100\%}, \tag{1.4}$$

where a_w is the water activity throughout the particle, σ is the surface tension, V_w is the molar volume of water, R is the gas constant, and T is the temperature. The exponential term on left-hand side of Eq. 1.4 accounts for the role of surface curvature on vapor pressure at the air-particle interface (the Kelvin effect). When curvature can be neglected, Eq. 1.4 can be simplified to $a_w = \text{RH}/100\%$.[4]

Aerosol particles under ambient RH conditions are often non-ideal solutions. The water activity as a function of solute mole or mass fraction for different types of aerosol can be determined with thermodynamic models. In this work, we will make extensive use of the Aerosol

Inorganic-Organic Mixtures Functional groups Activity Coefficients (AIOMFAC).[76–78] The water activity as a function of solute mass fraction in a binary particle can be parameterized by fitting the output of such a model. It is then possible to determine the expected solute mass fraction in the particle at a given RH.

1.2 The refractive index

The RI, m, is a complex quantity that describes the interaction of light with matter. In the context of aerosol, the real part of the RI, n, describes the scattering and the imaginary part, k, describes the absorption. Both real and imaginary components depend on the wavenumber, ν, or wavelength, λ ($\nu = 1/\lambda$), of light

$$m(\nu) = n(\nu) + ik(\nu). \tag{1.5}$$

The Sun emits a broad range of wavelengths with an intensity peak at around 500 nm.[79] Absorption by gases in the stratosphere greatly reduces the amount of IR light which passes through to the troposphere.[4] The transmission of higher energy UV wavelengths is also reduced in the stratosphere due to attenuation by atmospheric ozone.[4] Earth's atmosphere does, however, possess an optical window that allows visible wavelengths to reach the surface with little attenuation. It is across the visible region where we are most interested in the interactions between light and aerosol.

1.2.1 Models for the real part of the refractive index

Lorentz-Lorenz equation

The microscopic origin of the RI can be understood in terms of atomic or molecular polarizability. Mixing rules should apply to the RI so long as no chemical reaction occurs upon mixing and changes in concentration does not greatly vary these polarizabilities.[80] Although it does not offer any direct information about the dispersion in the RI, the Lorentz-Lorenz relation is often used predict the real part of aerosol RI.[25,56,81] For a solution containing N components (including the solvent), the Lorentz-Lorenz relation can be written as

$$\sum_{i=1}^{N} x_i \frac{\alpha_i}{V_{m,i}} = \frac{3}{4\pi}\left(\frac{n^2-1}{n^2+2}\right), \tag{1.6}$$

where n is the real part of the RI for the solution (often at the sodium-D line, $\lambda = 589$ nm) $V_{m,i}$ is the molar volume, α_i is the molar polarizability and x_i is the mole fraction of the ith component.

Tang and coworkers performed single particle experiments on a number of atmospherically relevant aqueous inorganic solutes ($(NH_4)_2SO_4$, Na_2SO_4, $NaNO_3$, NH_4HSO_4, $(NH_4)_3H(SO_4)_2$, $NaHSO_4$, NaCl, $MgCl_2$ and $MgSO_4$) in the 1990's and determined their RIs as a function of water content at $\lambda = 633$ nm as well as partial molar refractions for the solutes.[27,82,83] The determined RIs can then be fit with a polynomial with y-intercept equal to the RI of pure water.[27] These measurements have become the standard to which all other RI models are compared.

Lienhard *et al.* also performed single particle measurements to determine RI as a function of water content.[58] Unlike Tang *et al.*, Lienhard *et al.* focused on organic solutes (raffionose, citric acid, tartaric acid, tannic acid and levoglucosan) as well as ternary mixtures of levoglucosan and ammonium salts.[58]

Krieger *et al.* used the Lorentz-Lorenz equation to model the RI of H_2SO_4-HNO_3-H_2O mixtures relevant to polar stratospheric aerosol.[84] This model includes both temperature and wavelength dependence. They incorporate the temperature dependence through a change in solution density and the wavelength dependence through wavelength-dependent partial molar refractivities. They measured the densities of binary (H_2SO_4-H_2O and HNO_3-H_2O) and ternary (H_2SO_4-HNO_3-H_2O) mixtures at temperatures between -60 and 30°C and the RI at four wavelengths spanning the visible region as a function of temperature. This model covers a range in temperature from -88 to 97°C, wavelengths from 0.25 to 2 μm and total acid contents between 0.05 and 0.7 by mass fraction.[84] Although only parameterized for one ternary system, this is one of the most comprehensive aerosol RI models available. It is also very complicated as a total of 64 fitting parameters were required to determine the wavelength, concentration and temperature dependence of the RI for this three-component system.[84]

Cauchy expression

The most commonly used expression to describe RI dispersion for weakly absorbing aqueous aerosol is the Cauchy expression:

$$n(\lambda) = n_0 + \frac{n_1}{\lambda^2} + \frac{n_2}{\lambda^4} + ... + \frac{n_N}{\lambda^{2N}}, \tag{1.7}$$

where n_0, n_1, n_2 ... n_N are fitting parameters and λ is the wavelength of light. The Cauchy expression is usually truncated after $N = 1$ or $N = 2$ depending on the range of wavelengths over which the dispersion is to be determined.[43,85–89] Note that the Cauchy expression is an empirical expression relating the real part of the RI and wavelength of a dielectric material, and although quite accurate across the visible region, becomes unreliable in the UV and IR regions.

Cotterell *et al.* provide parameterizations for the real part of the RI based on the Cauchy expression for five inorganic salts of atmospheric importance: NaCl, $NaNO_3$, $(NH_4)_2SO_4$, NH_4HSO_4 and Na_2SO_4.[86] They took RI measurements at five discrete wavelengths between 405 and 650 nm and in RH steps of 10% between 100% RH and the efflorescence point of the solute. Their model fits the RI with two Cauchy parameters, n_0 and n_1. They then incorporated the RH dependence on the RI by fitting n_0 and n_1 to fourth and third order polynomials of water activity, respectively. These parameterizations are used throughout this thesis to compare experimental and modeled RIs. However, it should be noted that some of the data sets from Cotterell *et al.* contain only a small number of data points for certain RHs. The parameterization for Na_2SO_4 uses a particularly small data set. We have

found this parameterization to be inconsistent with single-wavelength parameterizations for Na_2SO_4 by Tang and Munkelwitz,[82] as well as our own experimental data at low water activities.

Sellmeier equation

The Sellmeier equation can be used to describe the RI of a weakly absorbing medium:

$$n^2(\lambda) = 1 + \sum_i \frac{B_i \lambda^2}{\lambda^2 - C_i}, \tag{1.8}$$

where B_i and C_i are experimentally determined Sellmeier coefficients. The Sellmeier coefficients for the real part of the RI of distilled water have been determined by Daimon and Masumura and are used throughout this thesis.[90]

The Sellmeier equation is capable of describing the RI dispersion over a larger region of the electromagnetic spectrum than the Cauchy expression. However, over the visible region, the Cauchy and Sellmeier equations produce similar descriptions of the RI dispersion. Fig. 1.6 shows the RI of water and Sellmeier equation fit from Daimon and Masumura[90] and two- and three-term Cauchy expression fits of this data over the same spectral range. We see that the two-term Cauchy expression does not accurately describe the data. Contrarily, the three-term Cauchy expression describes the RI in the visible region, shaded in Fig. 1.6, quite well but becomes unreliable at longer wavelengths.

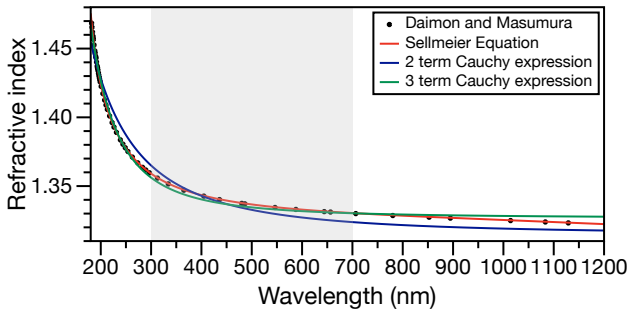

Figure 1.6: The refractive index of distilled water at 24°C from Daimon and Masumura with Sellmeier equation[90] and two- and three-term Cauchy expression fits. Shaded box highlights the visible region.

1.2.2 Models for the imaginary part of the refractive index

The absorption of weakly absorbing aerosol (e.g. aqueous NaCl, $(NH_4)_2SO_4$ and citric acid) is often neglected as the imaginary part of the RI is on the order of 10^{-9} in the visible region.[91,92] However, for strongly absorbing aerosol, such as brown carbon, the imaginary part of the RI must be considered.

The imaginary part of the RI is often determined in the bulk by collecting a UV-vis spectrum of the solute of interest dissolved in water. Assuming that the Beer-Lambert law is valid, the absorption spectrum can then be converted to the imaginary part of the RI[21]

$$\alpha(\lambda) = \frac{A(\lambda)}{l} = 4\pi\frac{k}{\lambda}, \tag{1.9}$$

where A is the measured absorbance at λ, l is the path length, and α is the wavelength-dependent absorption coefficient. Alternatively, it has been shown that the complex RI of an ensemble of absorbing particles can be determined with cavity ring down spectroscopy

(CRDS)[93] or using ellipsometry to characterize solid films of absorbing aerosol material.[88]

Brown carbon aerosol often has a distinct absorption profile, with the strongest absorption being found in the near-UV tailing off through the visible region. This absorption profile is most often described by a power law exponent called the absorption Ångstrom coefficient (AAC):[21,94]

$$\frac{\alpha(\lambda_1)}{\alpha(\lambda_2)} = \left(\frac{\lambda_1}{\lambda_2}\right)^{-\mathrm{AAC}}. \tag{1.10}$$

The AAC model is not valid over the full UV-vis spectrum, but only the portion where the wavelenght-dependent absorbance is linear on a log-log plot.[94]

1.3 Single particle experiments

Single particle techniques offer unique advantages over bulk aerosol measurements. By monitoring aerosol at the single particle level, statistics can be built up about the population instead of measuring its average.[42] These experiments can also be performed with RH and/or temperature control to mimic atmospheric conditions.[95,96] When combined with the surface-free environment that many single particle experiments employ, this control allows access to metastable states (e.g. supersaturated, supercooled) which can be experienced by aerosol in the atmosphere.[73]

Single particle experiments can be performed with particles on a substrate or by contactless methods, which have the added advantage of no substrate-particle interactions.[95] The two most common methods for three-dimensional (3D) confinement of aerosol particles are with an electrodynamic balance (EDB) and with optical tweezers.

EDBs trap particles using electric fields and are able to confine large particles under high flow rates of gas, but require the particle to be charged.[69,97] Optical tweezers use focused laser light to trap particles.[98] Expanding on standard optical tweezers, there have been new designs for many different purposes including loose focus traps to observe particle motion,[99] the trapping and manipulating of multiple particles with the use of a spatial light modulator,[100] the heating of particles to determine the imaginary part of the RI,[91,92] the stretching of particles to determine the surface tension,[101] and even the trapping of strongly absorbing particles by the photophoretic force.[102]

1.3.1 Radiation pressure optical trapping

Since 1970, when Arthur Ashkin discovered that particles can be confined with light,[103–105] optical trapping has become a useful tool to study single particles in atmospheric and biological sciences.[42,102,106–108] In a standard gradient force optical trap, also referred to as optical tweezers, a laser beam propagating vertically is tightly focused with a high numerical aperture (NA) lens.[98,109] A schematic of gradient force optical tweezers is shown in Fig. 1.7.

A focused beam imparts three forces on a particle: the gradient force, the scattering force, and spin-curl. Spin-curl is weak compared to the other two forces and is often neglected.[110] The scattering force occurs in the direction of beam propagation[110] and is a destabilizing force.[111] The gradient force arises from the spatial variation of electric field in the focused Gaussian beam.[111] The gradient force pushes a particle towards the most intense part of the beam. Stable trapping requires the net force on the particle to be equal to zero and occurs when the forces imparted by the focused laser beam equal that of gravity acting in

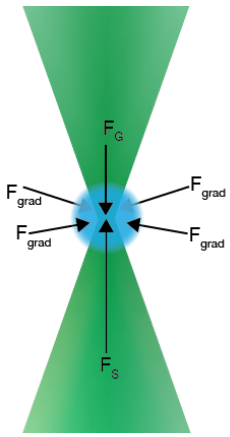

Figure 1.7: Gradient force optical tweezers. A particle becomes stably trapped where the scattering force, F_S, gradient force, F_{grad} and force of gravity, F_G are balanced.

the opposite direction.

There are a number of other external forces that may act on a particle trapped in air, arising from acoustic shocks, mechanical vibrations, thermal drifts, and airflow. These external forces may destabilize the particle or knock it out of the trap.[112,113] Aerosol trapping cells must be designed to reduce air currents around the particle in order to ensure stable trapping. Additionally, particles must be symmetric to remain stably trapped (e.g. spheres, ellipsoids, cylinders). Without an axis of symmetry, forces on the particle are not symmetric around the axis of laser propagation. In this case, radiation pressure will exert torque on the particle. This has been called the windmill effect, as the radiation pressure on asymmetric particles acts similarly to wind on a windmill.[114] Particles with an axis of rotational symmetry may remain trapped and rotating. In the context of aerosol, this usually leads to the particle being ejected from the trap when symmetry is lost upon efflorescence.[115]

Since the introduction of aerosol optical tweezers, more exotic trapping schemes have been developed, including the dual-beam optical trap used in this work.[91] The dual-beam

optical trap uses two equal power counter-propagating trapping beams aligned vertically or parallel to the optical table.[91,98,116,117] The two beams are tightly focused and their focal points aligned colinearly. In this trapping scheme, the scattering force from the two beams cancel as they are equal but act in opposite directions.[118]

When using optical tweezers to study aerosol, there are a number of possible issues one must consider that have not yet been discussed. First, a particle must not strongly absorb the wavelength of light used to create the trap. Absorption at this wavelength will cause the particle to heat up and quickly become unstable in the trap.[119] Aqueous particles are often trapped with a 532 nm laser, as water and many solutes of atmospheric relevance are weakly absorbing at this wavelength.[112] Additionally, one must consider the volatility of the particle. Solutes with high vapor pressures will quickly evaporate from a trapped particle which leads to water evaporation for the particle to remain in equilibrium with the surrounding air. This results in a continuously shrinking particle until it becomes too small to remain trapped.[120] Finally, the stability of the system under intense laser light must be considered, as some molecules may undergo a photochemical or heat-catalyzed reaction.[89,121,122]

1.3.2 Photophoretic trapping

Gradient force trapping is limited to weakly absorbing, dielectric particles. For particles that more strongly absorb light at the wavelength of the trapping beam, heating will be non-negligible and the particle may simply be vaporized or become unstable in the trap due to the phenomenon of photophoresis. The photophoretic force originates from an asymmetric heating of the particle.[102] An absorbing particle close to a laser beam will begin to heat on

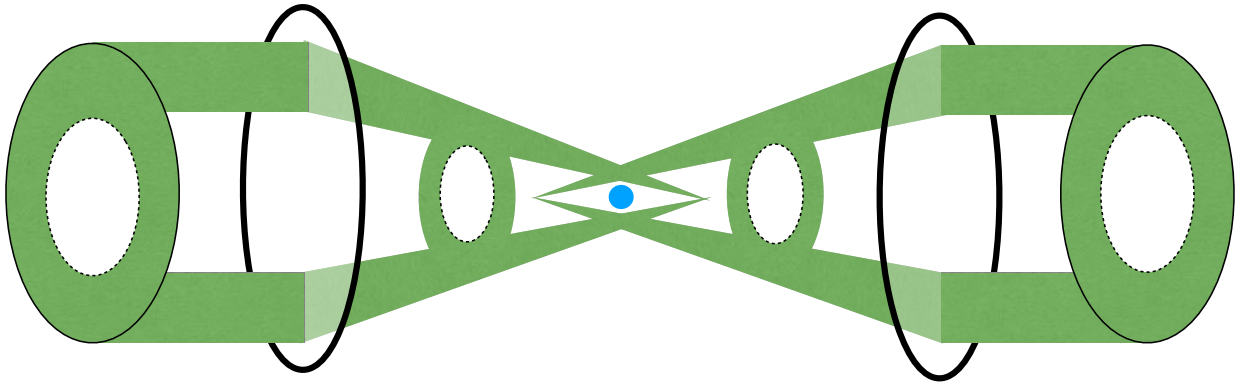

Figure 1.8: Schematic of a photophoretic trap created by focusing two hollow beams so that their focal points are slightly misaligned. An absorbing particle becomes trapped in the intensity void.

one side, and in turn, heat the gas molecules near its surface. These gas molecules will begin to travel faster, imparting a larger force on the particle as they collide with it, pushing the particle away from the source of heat.[112,123] A number of traps relying on the photophoretic force have been developed to confine absorbing particles.[102,113,119,124–126] These include hollow beams, speckle fields, tapper-ring fields, interference patterns from spherical aberrations, and 3D holograms with the use of spatial light modulators (SLMs).[113,124,127–130] Unlike optical tweezers, photophoretic traps are also capable of confining asymmetrically shaped particles such as pollen and dust spores.[102,113,124]

1.4 Light scattering

The confinement and optical imaging of particles alone does not offer much insight into their properties. To determine the chemical or physical properties of trapped aerosol, spectroscopic methods are often used to probe the particle. Fluorescence and Raman spectroscopy

of single particles have been used to determine chemical properties of aerosol,[96,125,131–133] but most commonly, scattering in the form of phase functions, cavity-enhanced Raman scattering (CERS) or broadband Mie scattering are used to determine aerosol physical properties.[34,44,95,101,134–137]

Light incident on a particle can be absorbed or scattered. The scattered light intensity will have an angular dependence that depends on the polarization of light and size parameter, x, defined in Eq. 1.2. When $x \ll 1$, Rayleigh scattering occurs and light is scattering is a dipolar pattern. At the other extreme, when $x \gg 1$, geometric optics describes the interaction of light with the particle and scattering primarily occurs in the forward direction. In between these two size regimes, when $x \approx 1$, Mie scattering occurs.[20]

Fig. 1.9 shows simulated angular scattering patterns for three size parameters with the incident beam arriving from the left. The forward scattering direction occurs at 0° and the back scattering occurs at 180°. These simulations show the scattering pattern for both a parallel and a perpendicular polarized incident plane wave. In all three panels, the parallel and perpendicular light are scattered with different relative intensities over the angular range.

1.4.1 Mie theory

The interaction of electromagnetic radiation with a particle induces oscillations in electrons. These oscillating charges radiate electromagnetic radiation in all directions. This is the scattered field. When the particle diameter is much smaller than the wavelength of light which is scattered, the scattered light is approximately in phase and there is little variation in intensity with scattering angle. If, however, the particle has a similar diameter to the incident

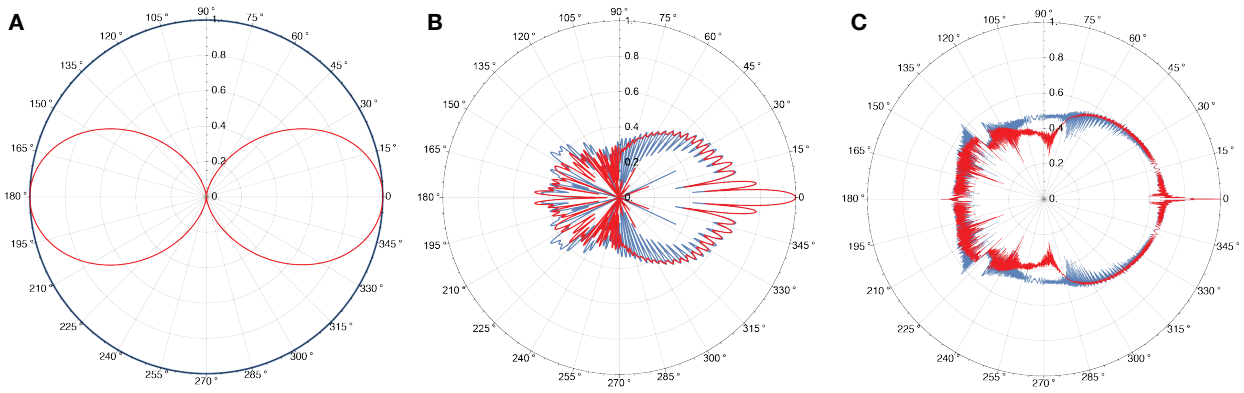

Figure 1.9: Scattering of parallel (blue) and perpendicular (red) polarizations for 650 nm radiation, by spheres having the refractive index of pure water at 25° C and radius of A) 5 nm ($x = 0.048$), B) 5 μm ($x = 48$) and C) 500 μm ($x = 4833$). Panels B and C are shown on a log scale.

light, scattered light may constructively and destructively interfere leading to variations of scattered light intensity with scattering angle. Mie theory describes the interaction between plane waves and dielectric spheres and can be used to calculate the scattered field.[20]

Although Mie theory describes the interaction of a sphere and a plane wave, in the case of optical trapping, the incident beam often has a Gaussian profile. Bessel beams have also been used to trap and characterize aerosol particles.[134,138,139] To describe the interactions of different beam shapes with dielectric particles, generalized Lorenz-Mie theory (GLMT) has been developed.[139,140] To handle the problem of non-spherical particles, more computationally demanding T-matrix calculations are required.[141]

Throughout the work in this thesis we will employ Mie theory as optically trapped aqueous aerosol particles are spherical in shape and have a uniform composition. The difference between Mie theory and GLMT lies in the predicted intensities as a function of collection angle for phase function fitting or as a function of wavelength in Mie scattering spectra. In

Chapter 2 we show a comparison of simulated 1D phase functions using a plane wave and a Gaussian beam, the difference in intensity is minimal for the beam waists, particle sizes and RIs used in typical optical trapping experiments.

1.4.2 Angular Mie scattering

As shown in Fig. 1.9B, Mie theory predicts strong angular-dependent light scattering from spherical particles. Interference of light in the particle results in a complex pattern of bright and dark fringes in the far field.[134] The scattering pattern is dependent on the size parameter defined in Eq. 1.2 and the RI of the particle. The angular range of the measured fringe pattern will be determined by the position and NA of the collection objective. The resulting image is often referred to as a 2D phase function in the literature. If the 2D phase function is collected at 90° from the incident beam, it is typically reduced into a one dimensional (1D) phase function by averaging each column of the image or by taking only the center row of the image.[134] Both methods generate a series of crests and troughs in intensity as a function of collection angle. Fig. 1.10 shows an example of both a 1D and a 2D phase function. In this example, the 1D phase function was determined by averaging columns of the phase function.

Determining the size and RI of a particle from a phase function

In order to determine the radius and RI of a sphere from its phase function, a library of phase functions for a range of plausible radii and RIs can be generated using Mie theory[20,142] and compared to experimental measurements (e.g. using a grid search). The radius and RI

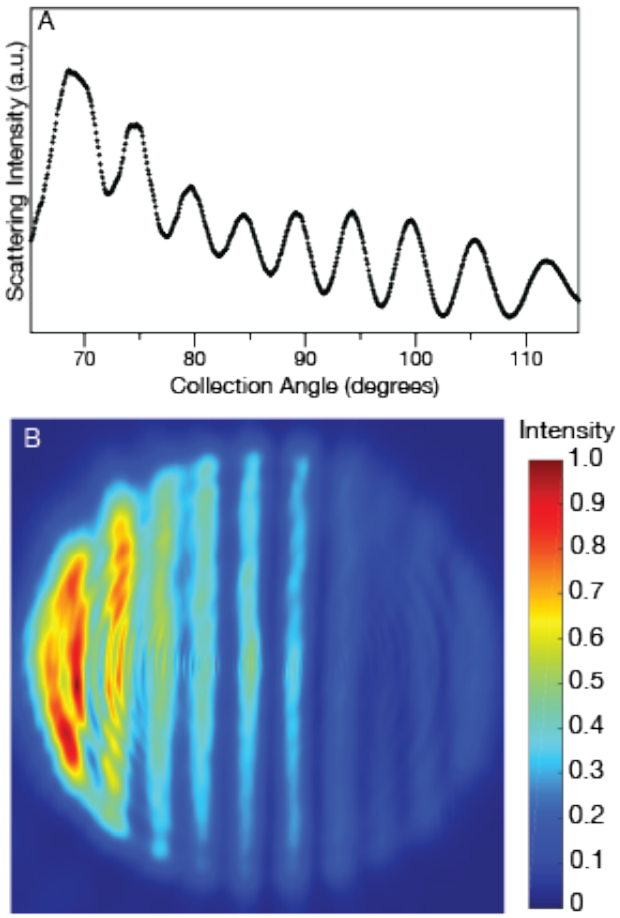

Figure 1.10: Example A) 1D and B) 2D phase functions.

of best-fit can be found by maximizing the correlation or minimizing the root-mean-square error between the phase functions in the library and the experimentally measured phase function.[134,142] A fitting algorithm for determining the size and RI of a particle using phase functions is presented in Chapter 2. The RI of best-fit will only be found at the wavelength of the elastically scattered light. To determine RI dispersion, a phase function must be taken with a series of probe beams of different wavelengths.[134] For nonspherical particles, the fringe pattern becomes highly complex and requires T-matrix calculations.[143] The work in this thesis is restricted to spherical particles.

1.4.3 Morphology-dependent resonances

A spherical particle can act as a high quality-factor optical cavity. When a particle interacts with a plane wave, total internal reflection of light around the particle–air interface can occur.[144,145] If the wavelength of light propagating around this interface is of the correct wavelength to constructively interfere with itself, light of this wavelength will build up in intensity. The wavelengths at which this build up occurs are called morphology-dependent resonances (MDRs), also commonly referred to as whispering gallery modes (WGMs) or Mie resonances.[144]

MDRs can be observed in CERS spectra, fluorescence spectra and broadband scattering spectra.[43,87,146] In the case of CERS, MDRs are only visible where there is spontaneous Raman scattering intensity. In the field of aerosol science, MDRs are typically collected over the broad, spontaneous Raman OH stretch of water for aqueous particles. For organic solutes, the nearby CH stretching band extends the range over which MDRs are visible.[58,86,91,147–149]

Although the OH stretch is broad compared to other Raman features, the range over which MDRs can be observed is limiting and requires particles are at least a few microns in radius for accurate Mie fitting.[136] If the particle fluoresces, the MDRs can likewise be observed over the fluorescence band, although this is not common for studies of aerosol and would require the addition of fluorescent dye to the particle.[109]

Broadband Mie scattering utilizes a white light source to illuminate the trapped particle.[43,87,136,150] MDRs are then visible over the entire spectrum of the broadband source. The implementation of broadband Mie scattering has allowed for the characterization of smaller particles as a much larger range of wavelengths can be collected, increasing the number of modes observed.[136,151] Fig. 1.11 shows a comparison from Moore *et al.* of the broadband scattering spectrum and the CERS spectrum of an aqueous ethylammonium nitrate droplet.[151] MDRs can be observed over both the Raman OH and CH stretching bands in the CERS spectrum but MDRs in the broadband spectrum can be observed over the full plotted spectral range.

MDRs are characterized by a set of quantum numbers describing the polarization, angular momentum and mode order.[152] The polarization, p, of a mode can be either transverse electric (TE) or transverse magnetic (TM), having the electric- or magnetic-field vectors tangential to the surface of the particle.[144] The angular momentum is described by a spherical harmonic, $Y_{l,m}$, where l is the mode number and m is the azimuthal mode number.[91,152] The mode number describes the size parameter of the resonant wavelength in the particle and the mode order, n, describes the number of lateral nodes in the MDR ($n-1$ nodes). The azimuthal modes are degenerate for a spherical particle. Features in Fig. 1.11 from Moore

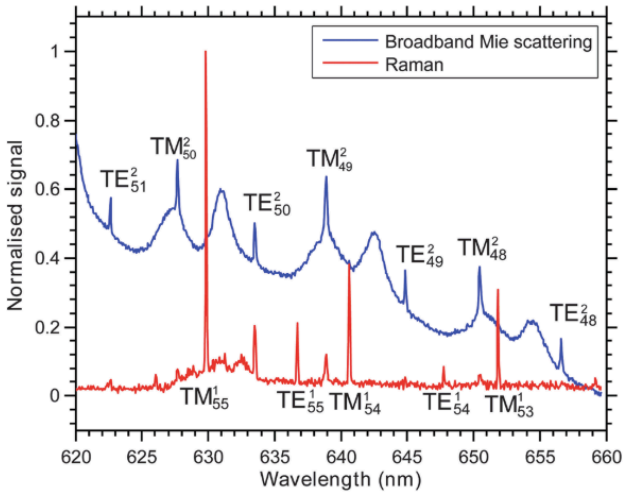

Figure 1.11: Comparison of the CERS spectrum (red line, bottom) and the broadband Mie scattering spectrum (blue line, top) from an aqueous droplet. Republished with permission of Royal Society of Chemistry, from Moore, L. J., Summers, M. D., & Ritchie, G. A. D. (2013). Optical trapping and spectroscopic characterisation of ionic liquid solutions. *Physical Chemistry Chemical Physics*, 15(32), 13489–13498.; permission conveyed through Copyright Clearance Center,Inc.

et al.[151] are labeled with their mode assignments in the form p_l^n.

In the scattering spectrum, modes alternate between TE and TM for a given mode order. The mode number decreases with longer wavelengths. Smaller mode orders appear in the scattering spectrum as narrow resonances and linewidths broaden with increasing mode order. Depending on the size parameter and resolution of the spectrograph used for collection, different mode orders will be visible in the scattering spectrum, with larger mode orders becoming visible for larger size parameters.[153] When multiple mode orders appear, the scattering spectrum quickly becomes complicated as modes of different orders may overlap.[97] The features in the scattering spectrum of a moderately absorbing particle will become broadened compared to those for a particle having the same radius and real RI but an absorption close to zero.[154] This will be discussed further in Chapter 3.

Determining the size and RI of a particle from MDRs

The Mie scattering spectrum can be fit in two ways: by fitting the full spectrum or using the positions of MDRs. Using only the positions of MDRs greatly reduces the computational demand and allows measurements to be fit in real-time. Algorithms for determining the size and RI of particles using the positions of the MDRs can be found in the literature.[85,155] The size and RI of an optically trapped particle can be determined with high accuracy using the positions of the MDRs.[85,156] Indeed, for a particle with a radius on the order of a few microns, its size can be determined with less than 1 nm uncertainty and the RI better than 0.11%.[156] Using the Mie scattering spectrum from CERS, fluorescence or broadband scattering, the RI dispersion can also be determined over the range of wavelengths MDRs are visible. As discussion in Section 1.2.1, the RI dispersion is most often described by a Cauchy expression.[85] However, it is not always feasible characterize a particle by simply fitting MDR positions as they may not be present in measurements. This will be the case when there are absorption bands that overlap with the wavelength range of the collected scattering spectrum. In Chapter 3, full spectrum fitting is discussed when analyzing the spectrum of a strongly absorbing particle.

References

[1] Kaufman, Y. J.; Tanré, D.; Boucher, O. A satellite view of aerosol in the climate system. *Nature* **2002**, *419*, 215–223.

[2] Hu, Z.; Huang, J.; Zhao, C.; Ma, Y.; Jin, Q.; Qian, Y.; Leung, L. R.; Bi, J.; Ma, J. Trans-Pacific transport and evolution of aerosols: Spatiotemporal characteristics and source contributions. *Atmos. Chem. Phys.* **2019**, *19*, 12709–12730.

[3] Tang, M.; Cziczo, D. J.; Grassian, V. H. Interactions of water with mineral dust Aerosol: Water Adsorption, Hygroscopicity, Cloud Condensation, and Ice Nucleation. *Chem. Rev.* **2016**, *116*, 4205–4259.

[4] Seinfeld, J. H.; Pandis, S. N. *Atmospheric chemistry and physics: From air pollution to climate change*, 3rd ed.; Wiley, 2006.

[5] Wu, L.; Li, X.; Kim, H.; Geng, H.; Godoi, R. H.; Barbosa, C. G.; Godoi, A. F.; Yamamoto, C. I.; De Souza, R. A.; Pöhlker, C.; Andreae, M. O.; Ro, C. U. Single-particle characterization of aerosols collected at a remote site in the Amazonian rainforest and an urban site in Manaus, Brazil. *Atmos. Chem. Phys.* **2019**, *19*, 1221–1240.

[6] Chou, C.; Formenti, P.; Maille, M.; Ausset, P.; Helas, G.; Harrison, M.; Osborne, S. Size distribution, shape, and composition of mineral dust aerosols collected during the African Monsoon Multidisciplinary Analysis Special Observation Period 0: Dust and biomass-burning experiment field campaign in Niger, January 2006. *J. Geophys. Res. Atmos.* **2008**, *113*, 1–17.

[7] Kuniyal, J. C.; Guleria, R. P. The current state of aerosol-radiation interactions: A mini review. *J. Aerosol Sci.* **2019**, *130*, 45–54.

[8] Rao, G.; Vejerano, E. P. Partitioning of volatile organic compounds to aerosols: A review. *Chemosphere* **2018**, *212*, 282–296.

[9] Knopf, D. A.; Alpert, P. A.; Wang, B. The role of organic aerosol in atmospheric ice nucleation: A review. *ACS Earth Space Chem.* **2018**, *2*, 168–202.

[10] Hill, S. C.; Williamson, C. C.; Doughty, D. C.; Pan, Y. L.; Santarpia, J. L.; Hill, H. H. Size-dependent

fluorescence of bioaerosols: Mathematical model using fluorescing and absorbing molecules in bacteria. *J. Quant. Spectrosc. Rad. Transf.* **2015**, *157*, 54–70.

[11] Nguyen, T. K. V.; Zhang, Q.; Jimenez, J. L.; Pike, M.; Carlton, A. G. Liquid water: Ubiquitous contributor to aerosol mass. *Environ. Sci. Technol. Lett.* **2016**, *3*, 257–263.

[12] Montoya-Aguilera, J.; Horne, J. R.; Hinks, M. L.; Fleming, L. T.; Perraud, V.; Lin, P.; Laskin, A.; Laskin, J.; Dabdub, D.; Nizkorodov, S. A. Secondary organic aerosol from atmospheric photooxidation of indole. *Atmos. Chem. Phys.* **2017**, *17*, 11605–11621.

[13] Harrison, R. M.; Yin, J. Particulate matter in the atmosphere: which particle properties are important for its effects on health? *Sci. Total Environ.* **2000**, *249*, 85 – 101.

[14] Davidson, C. I.; Phalen, R. F.; Solomon, P. A. Airborne Particulate Matter and Human Health: A Review. *Aerosol Sci. Technol.* **2005**, *39*, 737–749.

[15] Flores, J. M.; Washenfelder, R. A.; Adler, G.; Lee, H. J.; Segev, L.; Laskin, J.; Laskin, A.; Nizkorodov, S. A.; Brown, S. S.; Rudich, Y. Complex refractive indices in the near-ultraviolet spectral region of biogenic secondary organic aerosol aged with ammonia. *Phys. Chem. Chem. Phys.* **2014**, *16*, 10629–10642.

[16] Riziq, A. A.; Erlick, C.; Dinar, E.; Rudich, Y. Optical properties of absorbing and non-absorbing aerosols retrieved by cavity ring down (CRD) spectroscopy. *Atmos. Chem. Phys.* **2007**, *7*, 1523–1536.

[17] Feng, Y.; Ramanathan, V.; Kotamarthi, V. R. Brown carbon: A significant atmospheric absorber of solar radiation. *Atmos. Chem. Phys.* **2013**, *13*, 8607–8621.

[18] Valenzuela, A.; Reid, J. P.; Bzdek, B. R.; Orr-Ewing, A. J. Accuracy Required in Measurements of Refractive Index and Hygroscopic Response to Reduce Uncertainties in Estimates of Aerosol Radiative Forcing Efficiency. *J. Geophys. Res. Atmos.* **2018**, *123*, 6469–6486.

[19] Erlick, C.; Abbatt, J. P.; Rudich, Y. How different calculations of the refractive index affect estimates of the radiative forcing efficiency of ammonium sulfate aerosols. *J. Atmos. Sci.* **2011**, *68*, 1845–1852.

[20] Bohren, C. F.; Huffman, D. R. *Absorption and scattering of light by small particles*; WILEY-VCH: Weinheim, 1983.

[21] Moosmüller, H.; Chakrabarty, R. K.; Ehlers, K. M.; Arnott, W. P. Absorption Ångström coefficient, brown carbon, and aerosols: Basic concepts, bulk matter, and spherical particles. *Atmos. Chem. Phys.* **2011**, *11*, 1217–1225.

[22] Pilinis, C.; Pandis, S. N.; Seinfeld, J. H. Sensitivity of direct climate forcing by atmospheric aerosols to aerosol size and composition. *J. Geophys. Res.* **1995**, *100*.

[23] Zarzana, K. J.; Cappa, C. D.; Tolbert, M. A. Sensitivity of aerosol refractive index retrievals using optical spectroscopy. *Aerosol Sci. Tech.* **2014**, *48*, 1133–1144.

[24] Wang, W.; Rood, M. J. Real refractive index: Dependence on relative humidity and solute composition with relevancy to atmospheric aerosol particles. *J. Geophys. Res. Atmos.* **2008**, *113*, 1–9.

[25] Bouteloup, R.; Mathieu, D. Improved model for the refractive index: Application to potential components of ambient aerosol. *Phys. Chem. Chem. Phys.* **2018**, *20*, 22017–22026.

[26] Weast, R. C.; Astle, M. J.; Beyer, W. H. E. *CRC handbook of chemistry and physics*, 66th ed.; CRC Press, 1985.

[27] Tang, I. N.; Munkelwitz, H. R. Simultaneous determination of refractive index and density of an evaporating aqueous solution droplet. *Aerosol Sci. Technol.* **1991**, *15*, 201–207.

[28] Rowland, F. S. Stratospheric ozone. *Annu. Rev. Phys. Chem* **1991**, *42*, 731–768.

[29] Genthon, C.; Barnolat, J. M.; Raynaudt, D.; Lorius, C.; Jouzel, J.; Barkov, N. I.; Korotkevich, Y. S.; Kotlyakov, V. M. Vostok ice core: climate responce to CO_2 and orbital forcing changes over last climate cycle. *Nature* **1987**, *329*, 414–418.

[30] Lelieveld, J.; Crutzen, P. J.; Dentener, F. J. Changing concentration, lifetime and climate forcing of atmospheric methane. *Tellus B* **1998**, *50*, 128–150.

[31] Boucher, O.; Randall, D.; Artaxo, P.; Bretherton, C.; Feingold, G.; Forster, P.; Kerminen, V.-M. V.-M.; Kondo, Y.; Liao, H.; Lohmann, U.; Rasch, P.; Satheesh, S. K.; Sherwood, S.; Stevens, B.; Zhang, X. Y. *Climate Change 2013: The Physical Science Basis. Contribution of Working Group I to the Fifth Assessment Report of the Intergovernmental Panel on Climate Change*; 2013; Chapter Clouds and Aerosols, pp 571–657.

[32] Jung, C. H.; Lee, J. Y.; Kim, Y. P. Estimation of aerosol optical properties considering hygroscopicity and light absorption. *Atmos. Environ.* **2015**, *105*, 191–201.

[33] Lee, H. J.; Aiona, P. K.; Laskin, A.; Laskin, J.; Nizkorodov, S. A. Effect of solar radiation on the optical properties and molecular composition of laboratory proxies of atmospheric brown carbon. *Environ. Sci. Technol.* **2014**, *48*, 10217–10226.

[34] Dennis-Smither, B. J.; Hanford, K. L.; Kwamena, N. O. A.; Miles, R. E.; Reid, J. P. Phase, morphology, and hygroscopicity of mixed oleic acid/sodium chloride/water aerosol particles before and after ozonolysis. *J. Phys. Chem. A* **2012**, *116*, 6159–6168.

[35] Pratap, V.; Battaglia, M. A.; Carlton, A. G.; Hennigan, C. J. No evidence for brown carbon formation in ambient particles undergoing atmospherically relevant drying. *Environ. Sci. Process. Impacts* **2020**, *22*, 442–450.

[36] Ebben, C. J. et al. Contrasting organic aerosol particles from boreal and tropical forests during HUMPPA-COPEC-2010 and AMAZE-08 using coherent vibrational spectroscopy. *Atmos. Chem. Phys.* **2011**, *11*, 10317–10329.

[37] Romonosky, D. E.; Li, Y.; Shiraiwa, M.; Laskin, A.; Laskin, J.; Nizkorodov, S. A. Aqueous Photochemistry of Secondary Organic Aerosol of α-Pinene and α-Humulene Oxidized with Ozone, Hydroxyl Radical, and Nitrate Radical. *J. Phys. Chem. A* **2017**, *121*, 1298–1309.

[38] Lavi, A.; Lin, P.; Bhaduri, B.; Carmieli, R.; Laskin, A.; Rudich, Y. Characterization of light-absorbing oligomers from reactions of phenolic compounds and Fe(III). *ACS Earth Space Chem.* **2017**, *1*, 637–646.

[39] Moore, M. J.; Furutani, H.; Roberts, G. C.; Moffet, R. C.; Gilles, M. K.; Palenik, B.; Prather, K. A. Effect of organic compounds on cloud condensation nuclei (CCN) activity of sea spray aerosol produced by bubble bursting. *Atmos. Environ.* **2011**, *45*, 7462–7469.

[40] Weber, R. J.; Guo, H.; Russell, A. G.; Nenes, A. High aerosol acidity despite declining atmospheric sulfate concentrations over the past 15 years. *Nat. Geosci.* **2016**, *9*, 282–285.

[41] Bondy, A. L.; Bonanno, D.; Moffet, R. C.; Wang, B.; Laskin, A.; Ault, A. P. The diverse chemical mixing state of aerosol particles in the southeastern United States. *Atmos. Chem. Phys.* **2018**, *18*, 12595–12612.

[42] Ault, A. P.; Axson, J. L. Atmospheric aerosol chemistry: Spectroscopic and microscopic advances. *Anal. Chem.* **2017**, *89*, 430–452.

[43] Jones, S. H.; King, M. D.; Ward, A. D. Atmospherically relevant core–shell aerosol studied using optical trapping and Mie scattering. *Chem. Comm.* **2015**, *51*, 4914–4917.

[44] Gorkowski, K.; Donahue, N. M.; Sullivan, R. C. Determination of biphasic core–shell droplet properties using aerosol optical tweezers. *Environ. Sci.: Processes Impacts* **2018**, *20*, 1512–1523.

[45] Berkemeier, T.; Shiraiwa, M.; Pöschl, U.; Koop, T. Competition between water uptake and ice nucleation by glassy organic aerosol particles. *Atmos. Chem. Phys.* **2014**, *14*, 12513–12531.

[46] Bzdek, B. R.; Reid, J. P.; Malila, J.; Prisle, N. L. The surface tension of surfactant-containing, finite volume droplets. *Proc. Natl. Acad. Sci. U. S. A.* **2020**, *117*, 8335–8343.

[47] Estillore, A. D.; Hettiyadura, A. P. S.; Qin, Z.; Leckrone, E.; Wombacher, B.; Humphry, T.; Stone, E. A.; Grassian, V. H. Water Uptake and Hygroscopic Growth of Organosulfate Aerosol. *Environ. Sci. Technol.* **2016**, *50*, 4259–4268.

[48] Li, Y. J.; Liu, P. F.; Bergoend, C.; Bateman, A. P.; Martin, S. T. Rebounding hygroscopic inorganic aerosol particles: Liquids, gels, and hydrates. *Aerosol Sci. Technol.* **2017**, *51*, 388–396.

[49] Gupta, D.; Kim, H.; Park, G.; Li, X.; Eom, H. J.; Ro, C. U. Hygroscopic properties of NaCl and $NaNO_3$ mixture particles as reacted inorganic sea-salt aerosol surrogates. *Atmos. Chem. Phys.* **2015**, *15*, 3379–3393.

[50] Davies, J. F.; Wilson, K. R. Raman Spectroscopy of Isotopic Water Diffusion in Ultraviscous, Glassy, and Gel States in Aerosol by Use of Optical Tweezers. *Anal. Chem.* **2016**, *88*, 2361–2366.

[51] Krieger, U. K.; Marcolli, C.; Reid, J. P. Exploring the complexity of aerosol particle properties and processes using single particle techniques. *Chem. Soc. Rev.* **2012**, *41*, 6631–6662.

[52] Hallquist, M. et al. The formation, properties and impact of secondary organic aerosol: Current and emerging issues. *Atmos. Chem. Phys.* **2009**, *9*, 5155–5236.

[53] Rickards, A. M.; Miles, R. E.; Davies, J. F.; Marshall, F. H.; Reid, J. P. Measurements of the sensitivity

of aerosol hygroscopicity and the κ parameter to the O/C ratio. *J. Phys. Chem. A* **2013**, *117*, 14120–14131.

[54] DeRieux, W. S. W.; Li, Y.; Lin, P.; Laskin, J.; Laskin, A.; Bertram, A. K.; Nizkorodov, S. A.; Shiraiwa, M. Predicting the glass transition temperature and viscosity of secondary organic material using molecular composition. *Atmos. Chem. Phys.* **2018**, *18*, 6331–6351.

[55] Marsh, A.; Miles, R. E.; Rovelli, G.; Cowling, A. G.; Nandy, L.; Dutcher, C. S.; Reid, J. P. Influence of organic compound functionality on aerosol hygroscopicity: Dicarboxylic acids, alkyl-substituents, sugars and amino acids. *Atmos. Chem. Phys.* **2017**, *17*, 5583–5599.

[56] Cai, C.; Marsh, A.; Zhang, Y. H.; Reid, J. P. Group Contribution Approach to Predict the Refractive Index of Pure Organic Components in Ambient Organic Aerosol. *Environ. Sci. Technol.* **2017**, *51*, 9683–9690.

[57] Laskin, J.; Laskin, A.; Nizkorodov, S. A. Mass Spectrometry Analysis in Atmospheric Chemistry. *Anal. Chem.* **2018**, *90*, 166–189.

[58] Lienhard, D. M.; Bones, D. L.; Zuend, A.; Krieger, U. K.; Reid, J. P.; Peter, T. Measurements of Thermodynamic and Optical Properties of Selected Aqueous Organic and Organic - Inorganic Mixtures of Atmospheric Relevance. *J. Phys. Chem. A* **2012**, *116*, 9954–9968.

[59] Decesari, S. et al. Characterization of the organic composition of aerosols from Rondônia, Brazil, during the LBA-SMOCC 2002 experiment and its representation through model compounds. *Atmos. Chem. Phys.* **2006**, *6*, 375–402.

[60] Theodosi, C.; Panagiotopoulos, C.; Nouara, A.; Zarmpas, P.; Nicolaou, P.; Violaki, K.; Kanakidou, M.; Sempéré, R.; Mihalopoulos, N. Sugars in atmospheric aerosols over the Eastern Mediterranean. *Prog. Oceanogr.* **2018**, *163*, 70–81.

[61] Zobrist, B.; Marcolli, C.; Pedernera, D. A.; Koop, T. Do atmospheric aerosols form glasses? *Atmos. Chem. Phys.* **2008**, *8*, 5221–5244.

[62] Wang, C. C.; Tan, J.; Liu, L. Wavelength and concentration-dependent optical multi-component mixed-salt solutions. *Appl. Opt.* **2017**, *56*, 7662–7671.

[63] Freedman, M. A.; Hasenkopf, C. A.; Beaver, M. R.; Tolbert, M. A. Optical Properties of Internally Mixed Aerosol Particles Composed of Dicarboxylic Acids and Ammonium Sulfate. *J. Phys. Chem. A* **2009**, *13*, 13584–13592.

[64] Lightstone, J. M.; Onasch, T. B.; Imre, D. Deliquescence, Efflorescence, and Water Activity in Ammonium Nitrate and Mixed Ammonium Nitrate/Succinic Acid Microparticles. *J. Phys. Chem. A* **2000**, *104*, 9337–9346.

[65] Rovelli, G.; Song, Y.-C.; Maclean, A. M.; Topping, D. O.; Bertram, A. K.; Reid, J. P. Comparison of Approaches for Measuring and Predicting the Viscosity of Ternary Component Aerosol Particles. *Anal. Chem.* **2019**, *91*, 5074–5082.

[66] Marsh, A.; Petters, S. S.; Rothfuss, N. E.; Rovelli, G.; Song, Y. C.; Reid, J. P.; Petters, M. D. Amorphous phase state diagrams and viscosity of ternary aqueous organic/organic and inorganic/organic mixtures. *Phys. Chem. Chem. Phys.* **2018**, *20*, 15086–15097.

[67] Marshall, F. H.; Miles, R. E.; Song, Y. C.; Ohm, P. B.; Power, R. M.; Reid, J. P.; Dutcher, C. S. Diffusion and reactivity in ultraviscous aerosol and the correlation with particle viscosity. *Chem. Sci.* **2016**, *7*, 1298–1308.

[68] Lund Myhre, C. E.; Nielsen, C. J. Optical properties in the UV and visible spectral region of organic acids relevant to tropospheric aerosols. *Atmos. Chem. Phys.* **2004**, *4*, 1759 –1769.

[69] Rovelli, G.; Miles, R. E. H.; Reid, J. P.; Clegg, S. L. Accurate Measurements of Aerosol Hygroscopic Growth over a Wide Range in Relative Humidity. *J. Phys. Chem. A* **2016**, *120*, 4376–4388.

[70] Tong, H. J.; Reid, J. P.; Bones, D. L.; Luo, B. P.; Krieger, U. K. Measurements of the timescales for the mass transfer of water in glassy aerosol at low relative humidity and ambient temperature. *Atmos. Chem. Phys.* **2011**, *11*, 4739–4754.

[71] Wang, L.-N.; Cai, C.; Zhang, Y.-H. Kinetically Determined Hygroscopicity and Efflorescence of Sucrose-Ammonium Sulfate Aerosol Droplets under Lower Relative Humidity. *J. Phys. Chem. B* **2017**, *121*, 8551–8557.

[72] Marsh, A.; Rovelli, G.; Miles, R. E.; Reid, J. P. Complexity of measuring and representing the hygroscopicity of mixed component aerosol. *J. Phys. Chem. A* **2019**, *123*, 1648–1660.

[73] Clegg, S. L.; Wexler, A. S. Densities and apparent molar volumes of atmospherically important electrolyte solutions. 1. The solutes H_2SO_4, HNO_3, HCl, Na_2SO_4, $NaNO_3$, NaCl, $(NH_4)_2SO_4$, NH_4NO_3, and NH_4Cl from 0 to 50°C. *J. Phys. Chem. A* **2011**, *115*, 3393–3460.

[74] Cai, C.; Miles, R. E.; Cotterell, M. I.; Marsh, A.; Rovelli, G.; Rickards, A. M.; Zhang, Y. H.; Reid, J. P. Comparison of methods for predicting the compositional dependence of the density and refractive index of organic-aqueous aerosols. *J. Phys. Chem. A* **2016**, *120*, 6604–6617.

[75] Lide, D. R. *CRC handbook of chemistry and physics*, 82nd ed.; CRC Press, 2002.

[76] Zuend, A.; Marcolli, C.; Luo, B. P.; Peter, T. A thermodynamic model of mixed organic-inorganic aerosols to predict activity coefficients. *Atmos. Chem. Phys.* **2008**, *8*, 4559–4593.

[77] Zuend, A.; Marcolli, C.; Booth, A. M.; Lienhard, D. M.; Soonsin, V.; Krieger, U. K.; Topping, D. O.; McFiggans, G.; Peter, T.; Seinfeld, J. H. New and extended parameterization of the thermodynamic model AIOMFAC: calculation of activity coefficients for organic-inorganic mixtures containing carboxyl, hydroxyl, carbonyl, ether, ester, alkenyl, alkyl, and aromatic functional groups. *Atmos. Chem. Phys.* **2011**, *11*, 9155–9206.

[78] Zuend, A. Aerosol Inorganic-Organic Mixtures Functional groups Activity Coefficients (AIOMFAC) website and online model. https://aiomfac.lab.mcgill.ca, 2020; last accessed: 2020-04-02.

[79] Aiona, P. K.; Luek, J. L.; Timko, S. A.; Powers, L. C.; Gonsior, M.; Nizkorodov, S. A. Effect of photolysis on Absorption and Fluorescence Spectra of Light-Absorbing Secondary Organic Aerosols. *ACS Earth Space Chem.* 235–245.

[80] Feynman, R. P.; Leighton, R. B.; Sands, M. *The Feynman Lectures on Physics*; Addison-Wesley Publishing Company, 1964; Vol. 2; Chapter 32.

[81] Herráez, J. V.; Belda, R. Refractive indices, densities and excess molar volumes of monoalcohols + water. *J. Solution Chem.* **2006**, *35*, 1315–1328.

[82] Tang, I. N.; Munkelwitz, H. R. Water activities, densities and refractive indices of aqueous sulfates and sodium nitrate droplets of atmospheric importance. *J. Geophys. Res.* **1994**, *99*, 18801–18808.

[83] Tang, I. N.; Tridico, A. C.; Fung, K. H. Thermodynamic and optical properties of sea salt aerosols. *J. Geophys. Res.* **1997**, *102*, 23269–23275.

[84] Krieger, U. K.; Mössinger, J. C.; Luo, B.; Weers, U.; Peter, T. Measurement of the refractive indices of H_2SO_4–HNO_3–H_2O solutions to stratospheric temperatures. *Appl. Opt.* **2000**, *39*, 3691.

[85] Preston, T. C.; Reid, J. P. Determining the size and refractive index of microspheres using the mode assignments from Mie resonances. *J. Opt. Soc. Am. A* **2015**, *32*, 2210–2217.

[86] Cotterell, M. I.; Willoughby, R. E.; Bzdek, B. R.; Orr-Ewing, A. J.; Reid, J. P. A complete parameterisation of the relative humidity and wavelength dependence of the refractive index of hygroscopic inorganic aerosol particles. *Atmos. Chem. Phys.* **2017**, *17*, 9837–9851.

[87] Shepherd, R. H.; King, M. D.; Marks, A.; Brough, N.; Ward, A. D. Determination of the refractive index of insoluble organic extracts from atmospheric aerosol over the visible wavelength range using optical tweezers. *Atmos. Chem. Phys.* **2018**, *18*, 5235–5252.

[88] Liu, P.; Zhang, Y.; Martin, S. T. Complex refractive indices of thin films of secondary organic materials by spectroscopic ellipsometry from 220 to 1200 nm. *Environ. Sci. Technol.* **2013**, *47*, 13594–13601.

[89] David, G.; Esat, K.; Ritsch, I.; Signorell, R. Ultraviolet broadband light scattering for optically-trapped submicron-sized aerosol particles. *Phys. Chem. Chem. Phys.* **2016**, *18*, 5477–5485.

[90] Daimon, M.; Masumura, A. Measurement of the refractive index of distilled water from the near-infrared region to the ultraviolet region. *Appl. Opt.* **2007**, *46*, 3811–3820.

[91] Rafferty, A.; Preston, T. C. Measuring the size and complex refractive index of an aqueous aerosol particle using electromagnetic heating and cavity-enhanced Raman scattering. *Phys. Chem. Chem. Phys.* **2018**, *20*, 17038–17047.

[92] Willoughby, R. E.; Cotterell, M. I.; Lin, H.; Orr-Ewing, A. J.; Reid, J. P. Measurements of the Imaginary Component of the Refractive Index of Weakly Absorbing Single Aerosol Particles. *J. Phys. Chem. A* **2017**, *121*, 5700–5710.

[93] Lang-Yona, N.; Rudich, Y.; Segre, E.; Dinar, E.; Abo-Riziq, A. Complex refractive indices of aerosols retrieved by continuous wave-cavity ring down aerosol spectrometer. *Anal. Chem.* **2009**, *81*, 1762–1769.

[94] Andersson, A. A Model for the Spectral Dependence of Aerosol Sunlight Absorption. *ACS Earth Space Chem.* **2017**, *1*, 533–539.

[95] Lu, J. W.; Isenor, M.; Chasovskikh, E.; Stapfer, D.; Signorell, R. Low-temperature Bessel beam trap for single submicrometer aerosol particle studies. *Rev. Sci. Instrum.* **2016**, *85*, 095107.

[96] Suzuki, H.; Matsuzaki, Y.; Muraoka, A.; Tachikawa, M. Raman spectroscopy of optically levitated supercooled water droplet. *J. Chem. Phys.* **2012**, *136*, 234508.

[97] Price, C. L.; Bain, A.; Wallace, B. J.; Preston, T. C.; Davies, J. F. Simultaneous Retrieval of the Size and Refractive Index of Suspended Droplets in a Linear Quadrupole Electrodynamic Balance. *J. Phys. Chem. A* **2020**, *124*, 1811–1820.

[98] Zhao, C. Practical guide to the realization of a convertible optical trapping system. *Opt. Express* **2017**, *25*, 2496–2510.

[99] David, G.; Esat, K.; Thanopulos, I.; Signorell, R. Digital holography of optically-trapped aerosol particles. *Commun. Chem.* **2018**, *1*, 1–9.

[100] Curtis, J. E.; Koss, B. A.; Grier, D. G. Dynamic holographic optical tweezers. *Opt. Comm.* **2002**, *207*, 169–175.

[101] Rafferty, A.; Gorkowski, K.; Zuend, A.; Preston, T. C. Optical deformation of single aerosol particles. *P. Natl. Acad. Sci. USA* **2019**, *116*, 19880–19886.

[102] Gong, Z.; Pan, Y.-L.; Wang, C. Optical configurations for photophoretic trap of single particles in air. *Rev. Sci. Instrum.* **2016**, *87*, 103104.

[103] Ashkin, A. Acceleration and Trapping of Particles by Radiation Pressure. *Phys. Rev. Lett.* **1970**, *24*, 156–159.

[104] Ashkin, A.; Dziedzic, J. M. Optical levitation by radiation pressure. *Appl. Phys. Lett.* **1971**, *19*, 283–285.

[105] Ashkin, A.; Dziedzic, J. M.; Bjorkholm, J. E.; Chu, S. Observation of a single-beam gradient force optical trap for dielectric particles. *Opt. Lett.* **1986**, *11*, 288–290.

[106] Zhang, H.; Liu, K. K. Optical tweezers for single cells. *J. R. Soc. Interface* **2008**, *5*, 671–690.

[107] Ritchie, D. B.; Woodside, M. T. Probing the structural dynamics of proteins and nucleic acids with optical tweezers. *Curr. Opin. Struc. Biol.* **2015**, *34*, 43–51.

[108] Avellaneda, M. J.; Franke, K. B.; Sunderlikova, V.; Bukau, B.; Mogk, A.; Tans, S. J. Processive extrusion of polypeptide loops by a Hsp100 disaggregase. *Nature* **2020**, *578*, 317–320.

[109] Wills, J. B.; Knox, K. J.; Reid, J. P. Optical control and characterisation of aerosol. *Chem. Phys. Lett.* **2009**, *481*, 153–165.

[110] Jones, P. H.; Marago, O. M.; Volpe, G. *Optical tweezers: Principles and applications*; Cambridge University Press, 2015.

[111] Mitchem, L.; Reid, J. P. Optical manipulation and characterisation of aerosol particles using a single-beam gradient force optical trap. *Chem. Soc. Rev.* **2008**, *37*, 756–769.

[112] Gong, Z.; Pan, Y. L.; Videen, G.; Wang, C. Optical trapping and manipulation of single particles in air: Principles, technical details, and applications. *J. Quant. Spec. Rad. Trans.* **2018**, *214*, 94–119.

[113] Redding, B.; Pan, Y.-L. Optical trap for both transparent and absorbing particles in air using a single shaped laser beam. *Opt. Lett.* **2015**, *40*, 2798–2801.

[114] Normanno, D.; Capitanio, M.; Pavone, F. S. Spin absorption, windmill, and magneto-optic effects in optical angular momentum transfer. *Phys. Rev. A - At. Mol. Opt. Phys.* **2004**, *70*, 1–8.

[115] Mason, B. J.; Cotterell, M. I.; Preston, T. C.; Orr-Ewing, A. J.; Reid, J. P. Direct Measurements of the Optical Cross Sections and Refractive Indices of Individual Volatile and Hygroscopic Aerosol Particles. *J. Phys. Chem. A* **2015**, *119*, 5701–5713.

[116] Kraikivski, P.; Pouligny, B.; Dimova, R. Implementing both short- and long-working-distance optical trappings into a commercial microscope. *Rev. Sci. Instrum.* **2006**, *77*.

[117] Rkiouak, L.; Tang, M. J.; Camp, J. C.; McGregor, J.; Watson, I. M.; Cox, R. A.; Kalberer, M.;

Ward, A. D.; Pope, F. D. Optical trapping and Raman spectroscopy of solid particles. *Phys. Chem. Chem. Phys.* **2014**, *16*, 11426–11434.

[118] Horst, A. V. D.; Oostrum, P. D. J. V.; Moroz, A.; Blaaderen, A. V.; Dogterom, M. High trapping forces for high-refractive index particles trapped in dynamic arrays of counterpropagating optical tweezers. *Appl. Opt.* **2008**, *47*, 3196–3202.

[119] Liu, F.; Zhang, Z.; Wei, Y.; Zhang, Q.; Cheng, T.; Wu, X. Photophoretic trapping of multiple particles in tapered-ring optical field. *Opt. Express* **2014**, *22*, 23716–23723.

[120] Cai, C.; Stewart, D. J.; Reid, J. P.; Zhang, Y. H.; Ohm, P.; Dutcher, C. S.; Clegg, S. L. Organic component vapor pressures and hygroscopicities of aqueous aerosol measured by optical tweezers. *J. Phys. Chem. A* **2015**, *119*, 704–718.

[121] Lienhard, D. M. et al. Viscous organic aerosol particles in the upper troposphere: Diffusivity-controlled water uptake and ice nucleation? *Atmos. Chem. Phys.* **2015**, *15*, 13599–13613.

[122] Parmentier, E. A.; David, G.; Arroyo, P. C.; Bibawi, S.; Esat, K.; Signorell, R. Photochemistry of single optically trapped oleic acid droplets. *J. Aerosol Sci.* **2021**, *151*, 0–10.

[123] Bluvshtein, N.; Krieger, U. K.; Peter, T. Photophoretic spectroscopy in atmospheric chemistry – high sensitivity measurements of light absorption by a single particle. *Atmos. Meas. Tech.* **2020**, *13*, 3191–3203.

[124] Wang, C.; Pan, Y.-L.; Coleman, M. Experimental observation of particle cones formed by optical trapping. *Opt. Lett.* **2014**, *39*, 2767–2770.

[125] Wang, C.; Pan, Y.-L.; Hill, S. C.; Redding, B. Photophoretic trapping-Raman spectroscopy for single pollens and fungal spores trapped in air. *J. Quant. Spectrosc. Rad. Transf.* **2015**, *153*, 4–12.

[126] Pan, Y.-L.; Wang, C.; Hill, S. C.; Coleman, M.; Beresnev, L. A.; Santarpia, J. L. Trapping of individual airborne absorbing particles using a counterflow nozzle and photophoretic trap for continuous sampling and analysis. *Appl. Phys. Lett.* **2014**, *104*, 113507.

[127] Alpmann, C.; Esseling, M.; Rose, P.; Denz, C.; Alpmann, C.; Esseling, M.; Rose, P.; Denz, C. Holographic optical bottle beams. *Appl. Phys. Lett.* **2012**, *100*, 111101.

[128] Shvedov, V. G.; Rode, A. V.; Izdebskaya, Y. V.; Desyatnikov, A. S.; Krolikowski, W.; Kivshar, Y. S. Speckle field as a multiple particle trap. *AIP Conf. Proc.* **2010**, *1278*, 26–37.

[129] Liu, F.; Zhang, Z.; Wei, Y.; Zhang, Q.; Cheng, T.; Wu, X. Photophoretic trapping of multiple particles in tapered-ring optical field. *Opt. Express* **2014**, *22*, 23716.

[130] Shvedov, V. G.; Hnatovsky, C.; Rode, A. V.; Krolikowski, W. Robust trapping and manipulation of airborne particles with a bottle beam. *Opt. InfoBase Conf. Pap.* **2011**, *19*, 273–275.

[131] Gong, Z.; Pan, Y.-L.; Videen, G.; Wang, C. The temporal evolution process from fluorescence bleaching to clean Raman spectra of single solid particles optically trapped in air. *Chem. Phys. Lett.* **2017**, *689*, 100–104.

[132] Gong, Z.; Pan, Y.-L.; Videen, G.; Wang, C. Optical trapping-Raman spectroscopy (OT-RS) with embedded microscopy imaging for concurrent characterization and monitoring of physical and chemical properties of single particles. *Anal. Chim. Acta* **2018**, *1020*, 86–94.

[133] Kalume, A.; Zhu, E.; Wang, C.; Santarpia, J.; Pan, Y.-L. Position-resolved Raman spectra from a laser-trapped single airborne chemical droplet. *Opt. Lett.* **2017**, *42*, 5113.

[134] Carruthers, A. E.; Walker, J. S.; Casey, A.; Orr-Ewing, A. J.; Reid, J. P. Selection and characterization of aerosol particle size using a Bessel beam optical trap for single particle analysis. *Phys. Chem. Chem. Phys.* **2012**, *14*, 6741–6748.

[135] Cotterell, M. I.; Mason, B. J.; Carruthers, A. E.; Walker, J. S.; Orr-Ewing, A. J.; Reid, J. P. Measurements of the evaporation and hygroscopic response of single fine-mode aerosol particles using a Bessel beam optical trap. *Phys. Chem. Chem. Phys.* **2014**, *16*, 2118–2128.

[136] Lew, L. J. N.; Ting, M. V.; Preston, T. C. Determining the size and refractive index of homogeneous spherical aerosol particles using Mie resonance spectroscopy. *Appl. Opt.* **2018**, *57*, 4601–4609.

[137] Cai, C.; Zhao, C. Optical levitation measurement on hygroscopic behaviour and SVOC vapour pressure of single organic/inorganic aqueous aerosol. *Atmos. Environ.* **2018**, *189*, 50–60.

[138] Thanopulos, I.; Luckhaus, D.; Preston, T. C.; Signorell, R. Dynamics of submicron aerosol droplets in a robust optical trap formed by multiple Bessel beams. *J. Appl. Phys.* **2014**, *115*, 154304.

[139] Preston, T. C.; Reid, J. P. Angular scattering of light by a homogeneous spherical particle in a zeroth-order Bessel beam and its relationship to plane wave scattering. *J. Opt. Soc. Am. A* **2015**, *32*, 1053–1062.

[140] Lock, J. A.; Gouesbet, G. Generalized Lorenz-Mie theory and applications. *J. Quant. Spec. Rad. Transf.* **2009**, *110*, 800–807.

[141] Mishchenko, M. I.; Travis, L. D. Capabilities and limitations of a current FORTRAN implementation of the T-matrix method for randomly oriented, rotationally symmetric scatterers. *J. Quant. Spec. Rad. Transf.* **1998**, *60*, 309–324.

[142] Schmitz, M.; Rothe, T.; Kienle, A. Evaluation of a spectrally resolved scattering microscope. *Biomed. Opt. Express* **2011**, *2*, 2665.

[143] Walters, S.; Zallie, J.; Seymour, G.; Pan, Y. L.; Videen, G.; Aptowicz, K. B. Characterizing the size and absorption of single nonspherical aerosol particles from angularly-resolved elastic light scattering. *J. Quant. Spectrosc. Radiat. Transf.* **2019**, *224*, 439–444.

[144] Foreman, M. R.; Swaim, J. D.; Vollmer, F. Whispering gallery mode sensors. *Adv. Opt. Photonics* **2015**, *7*, 168–240.

[145] Lam, C. C.; Leung, P. T.; Young, K. Explicit asymptotic formulas for the positions, widths, and strengths of resonances in Mie scattering. *J. Opt. Soc. Am. B* **1992**, *9*, 1585.

[146] Owen, J. F.; Chang, R. K.; Barber, P. W. Morphology–dependent resonances in Raman scattering, fluorescence emission, and elastic scattering from microparticles. *Aerosol Sci. Tech.* **1982**, *1*, 293–302.

[147] Knox, K. J.; Reid, J. P. Ultrasensitive absorption spectroscopy of optically-trapped aerosol droplets. *J. Phys. Chem. A* **2008**, *112*, 10439–10441.

[148] Gorkowski, K.; Beydoun, H.; Aboff, M.; Walker, J. S.; Reid, J. P.; Sullivan, R. C. Advanced aerosol optical tweezers chamber design to facilitate phase-separation and equilibration timescale experiments on complex droplets. *Aerosol Sci. Technol.* **2016**, *50*, 1327–1341.

[149] Day, C. P. F.; Miloserdov, A.; Widish-Jones, K.; Pearson, E.; Carruthers, A. E. Quantifying the hygroscopic properties of cyclodextrin containing aerosol for drug delivery to the lungs. *Phys. Chem. Chem. Phys.* **2020**, *22*, 11327–11336.

[150] Ward, A. D.; Zang, M.; Hunt, O. Broadband Mie scattering from optically levitated aerosol droplets using a white LED. *Opt. Express* **2008**, *16*, 16390–16403.

[151] Moore, L. J.; Summers, M. D.; Ritchie, G. A. Optical trapping and spectroscopic characterisation of ionic liquid solutions. *Phys. Chem. Chem. Phys.* **2013**, *15*, 13489–13498.

[152] Eversole, J. D.; Lin, H. B.; Huston, A. L.; Campillo, A. J.; Leung, P. T.; Liu, S. Y.; Young, K. High-precision identification of morphology-dependent resonances in optical processes in microdroplets. *J. Opt. Soc. Am. B* **1993**, *10*, 1955–1968.

[153] Chylek, P.; Kiehl, J. T.; Ko, M. Narrow resonance structure in the Mie scattering characteristics. *Appl. Opt.* **1978**, *17*, 3019–3021.

[154] Chylek, P.; Ngo, D.; Pinnick, R. G. Resonance Structure of Composite and Slightly Absorbing Spheres. *J. Opt. Soc. Am. A* **1992**, *9*, 775–780.

[155] Preston, T. C.; Reid, J. P. Accurate and efficient determination of the radius, refractive index, and dispersion of weakly absorbing spherical particle using whispering gallery modes. *J. Opt. Soc. Am. B* **2013**, *30*, 2113–2122.

[156] Miles, R. E. H.; Walker, J. S.; Burnham, D. R.; Reid, J. P. Retrieval of the complex refractive index of aerosol droplets from optical tweezers measurements. *Phys. Chem. Chem. Phys.* **2012**, *14*, 3037–3047.

Chapter 2

Determining the size and refractive index of single aerosol particles using angular light scattering and Mie resonances

Chapter Preface

In the previous chapter, the importance of accurate aerosol refractive indices for radiative forcing predictions was highlighted. Here, two methods of retrieving the radius and refractive index of single aerosol particles using Mie theory are compared. The aim of this chapter is to determine the most accurate method of refractive index determination.

2.1 Abstract

Optical trapping allows for high precision studies of many microphysical and chemical processes as it enables measurements on the single-particle level. This has been a tremendous benefit to fundamental aerosol research. In the vast majority of these experiments, trapped particles are characterized using light scattering – most often angular light scattering (phase functions) or Mie resonance spectroscopy. In this report, we compare the radii and refractive indices of best-fit found with these two light scattering methods by trapping single aerosol particles in a relative humidity-controlled cell where we can simultaneously measure both phase functions and Mie resonances, the latter of which are found using cavity-enhanced Raman scattering. Additionally, we compare best-fits found using both one- and two-dimensional phase functions. The application of Mie theory to these light scattering problems is thoroughly reviewed. Both the accuracy and uncertainty of the best-fits that these light scattering techniques produce are investigated using a model aqueous inorganic aerosol particle.

2.2 Introduction

Utilizing light scattering to characterize small airborne particles is an important analytical tool in aerosol science. There is also an intrinsic interest in the scattering and absorption cross-sections of aerosol particles due to the large uncertainty in how atmospheric particles interact with solar radiation in Earth's atmosphere.[1] Scattering by particles can be divided into the (i) Rayleigh, (ii) Mie, and (iii) geometric domains, where the wavelength of light relative to the size of the particle will be either (i) much larger, (ii) on the same order, or (iii) much smaller. While Rayleigh and geometric scattering are approximate solutions to the scattering problem, Mie theory provides an analytical solution to the problem of the scattering and absorption of an electromagnetic plane wave by a homogeneous spherical particle.[2,3] The rigorous treatment of Mie theory can be applied to all three of the listed domains but that is often avoided due to computational time requirements and the stronger intuitive appeal of the approximate models that are valid in either the Rayleigh or geometric domains.

At the core of a Mie calculation is the evaluation of scattering coefficients. Once these are known, then scattering and absorption cross-sections can be found along with the elements of the amplitude scattering matrix, the latter of which enables the calculation of angular light scattering. Furthermore, the denominators of the Mie scattering coefficients themselves can be set to zero to yield expressions for the electric and magnetic modes in a homogeneous spherical particle. These resonances are referred to as Mie resonances (for a homogeneous spherical particle) but are also often called morphology-dependent resonances,

optical resonances, or whispering gallery mode resonances.[4–11] Weakly absorbing spherical particles can behave like high quality factor optical cavities and support modes with very sharp resonances.

Measurements of Mie resonances in scattering spectra can both be used to determine the size and refractive index of spherical particles. However, due to their sensitivity to size and composition, the use of Mie resonance positions for characterization is often only practical in single, spherical particle experiments.[12] Mie resonances have been observed in Raman, fluorescence and broadband spectra for single particles and can be extremely narrow.[7,9,13–18] Resonance fitting can have remarkable precision and accuracy when determining size and wavelength-dependent refractive index.[7,9,10,14,19–22] Best-fits are found by generating a library of calculated peak positions for a range of refractive indices and radii and minimizing the sum of squared residuals (or maximizing correlation) between calculated and measured resonance positions.[7,10] Throughout the years, there have been many fitting procedures presented in the literature.[7,9,10,22–25] A micrometer-sized particle can be sized with around ± 1 nm precision and its refractive index can be determined to 10^{-4}.[19,26,27] For instance, Preston and Reid determined particle radii with errors as low as 0.032% for particles with radii of about 5 μm.[9]

Angular light scattering can also be measured and fitted using Mie theory. When scattered light is collected from a single particle with an objective whose focal plane is near, but does not overlap with, the location of the particle, bright and dark fringes can be imaged on a camera.[28–30] This two-dimensional (2D) image is often referred to as a phase function.[31,32] and the angular range over which it is collected is determined by the position and numerical aperture (NA) of the collection objective. Collected phase function images are often

transformed into one-dimensional (1D) spectra by averaging each column of the image[32–36] or taking slices through the image.[37,38] The resulting 1D spectrum is then compared to a library of spectra calculated with Mie theory for a physically plausible range of radii and refractive indices. Correlation analysis,[28,39] or sum of squared residuals[32] can be used to compare the calculated and experimental spectra in order to determine the best-fit. It has been reported that radii can be determined to within 3% when one phase function image is used[28] and below 2% when phase functions collected with different incident wavelengths are used.[32]

Alternatively, the measured 2D phase function can be directly fitted using Mie theory. In fact, such fits have been recently explored in a field outside aerosol science using single particle scattering microscopy (where scattered light that was collected from single particles on a cover slip was fitted).[31,35,40] In that work, the correlation between measured and calculated 2D phase functions was used to determine best-fits. The uncertainty in the radii of the best-fits was below 0.3% when considering scattering patterns across many different wavelengths.

Measurements of angular light scattering on the single particle level are of great importance in the aerosol community as it eliminates averaging effects. Single aerosol particles can be spatially confined by electrostatic forces,[30,41–43] photophoretic forces,[44–46] and by using optical forces to levitate[47,48] or trap.[7,21,49–51] Traps based on the photophoretic force are limited to particles which absorb radiation[44–46] and those based on electrostatic forces are limited to particles with charges, while optical force based traps are limited to weakly absorbing particles. Optical levitation does not confine particles as well in space as a gradient based optical trap. Using optically based traps for light scattering experiments has the

advantage of not requiring a probe beam, as the trapping beam can also be used for this purpose.[7,46,48,50,52,53] Other trapping methods such as acoustic trap[54,55] have not been widely adopted by the aerosol community as typical trapping frequencies are only appropriate for droplets much larger than a few microns.

In this report, we compare the radius and refractive index of best-fit found by fitting 1D phase functions, 2D phase functions, and Mie resonances. The Mie resonance positions are extracted from sharp peaks observed in cavity-enhanced Raman scattering (CERS) spectra. Simultaneous measurements of both phase functions and Mie resonances are performed in a relative humidity (RH) controlled cell where a single aerosol particle is held with a dual-beam optical trap. For the first time, we are able to assess the accuracy of phase function best-fits relative to Mie resonance best-fits. These best-fits are also compared to predictions from a thermodynamic model and refractometer measurements. Additionally, we compare the 1D and 2D phase functions best-fits in order to determine if transforming 2D measurements into 1D spectra reduces the accuracy of the subsequent best-fit. For our model aqueous inorganic system, we consider particles composed of water and lithium chloride (LiCl). This type of particle is well suited for our study as we can readily control particle size and refractive index by changing the RH inside our trapping cell: when the RH surrounding a particle is adjusted the particle will grow or shrink as it equilibrates with the surrounding water vapor. As the LiCl is non-volatile, this also leads to a change in solute concentration in the particle which will alter its refractive index.[56]

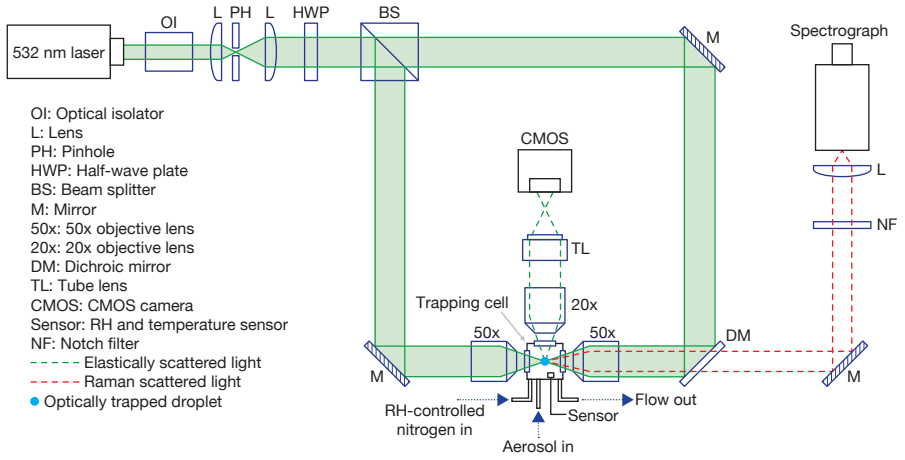

Figure 2.1: Schematic of setup used to perform experiments. Phase functions were collected with the CMOS camera and CERS spectra were collected with the spectrograph.

2.3 Experimental

Fig. 2.1 shows the optical trapping setup that was used in all experiments performed here. Light from a $\lambda = 532$ nm laser (Opus 532, Laser Quantum) was expanded as it passed through a 1.2× telescope. A half-wave plate was then used to orient the polarization angle of the beam such that when it subsequently passed through a polarizing beamsplitting cube, it was split into two beams of equal intensity that were orthogonally polarized. Two 50× objectives (SLMPLN50X, Olympus) with a NA of 0.35 were used to focus the two counter-propagating beams into the trapping cell. Inside the cell, the focal points of both beams were located at the same position. The RH in the cell was controlled by two mass flow controllers (MF-1, MKS Instruments) that bring RH-controlled air into the cell. The RH and temperature inside the cell were monitored in five second intervals with a probe (SHT75x, Sensirion).

To collect angular light scattering images (phase functions), a 20× long working distance

objective (PSM-PLAPO20X, Motic) with a NA of 0.42 collected scattered light orientated 90° to the two trapping beams. The phase function was then imaged with a CMOS camera (DCC1545M, Thorlabs). Forward and backscattered Raman light was collected with one of the 50× objectives, transmitted through a dichroic mirror (LPD02-532RU-25, Semrock) and coupled into a spectrograph (Isoplane SCT-320, Princeton Instruments) where it was then imaged on a CCD (PIXIS:100B_eXcelon, Princeton Instruments).

A medical nebulizer (MicroAir, Omron) was used to generate aqueous LiCl aerosol particles. Aerosol plumes would be drawn into the trapping cell where a single particle would be trapped at the shared focal point of the two counter-propagating Gaussian beams. Once a particle was trapped, it was allowed to equilibrate with its surroundings. After equilibration, data collection began and Raman spectra and phase function images were recorded at one second intervals. After the data was collected, the RH was changed by introducing a different ratio of moist to dry air into the cell. The particle was again allowed to come to equilibrium with its new surroundings before a new set of data was recorded.

2.4 Theory

2.4.1 Angular light scattering

Light scattering by a homogeneous spherical particle can be accurately calculated using Mie theory when the incident beam is well described as an electromagnetic plane wave.[3] Fig. 2.2 shows the geometry that will be used here to describe the scattering problem. For an

incident plane wave that is characterized by a wavevector $\vec{k}_i$ and a scattered wave that is characterized by a wavevector $\vec{k}_s$ we can define the scattering angle Θ as

$$\Theta = \arccos\left(\frac{\vec{k}_i \cdot \vec{k}_s}{|\vec{k}_i||\vec{k}_s|}\right). \tag{2.1}$$

In the geometry of Fig. 2.2, the wavevectors are

$$\vec{k}_i = k\begin{pmatrix} \sin\vartheta_i\cos\varphi_i \\ \sin\vartheta_i\sin\varphi_i \\ \cos\varphi_i \end{pmatrix} \quad \text{and} \quad \vec{k}_s = k\begin{pmatrix} \sin\vartheta_s\cos\varphi_s \\ \sin\vartheta_s\sin\varphi_s \\ \cos\varphi_s \end{pmatrix}, \tag{2.2}$$

where the angular wavenumber is $k = 2\pi/\lambda$ and λ is the wavelength of light in the medium surrounding the spherical particle. The incident angles, ϑ_i and φ_i, and the scattering angles, ϑ_s and φ_s, are defined in Fig. 2.2.

If the incident wave is described by the Stokes parameters $\vec{S}_i = (I_i, Q_i, U_i, V_i)^{\mathrm{T}}$, the Stokes-Mueller formalism for the scattering process yields[31]

$$\vec{S}_s = \vec{M}\vec{R}\vec{S}_i, \tag{2.3}$$

where $\vec{M}$ is the scattering matrix, $\vec{R}$ is the rotation matrix, and $\vec{S}_s = (I_s, Q_s, U_s, V_s)^{\mathrm{T}}$ is the Stokes parameters associated with the scattered wave. Other authors[31,40] have included transmission matrices in Eq. 2.3 but they are not used here as we will assume that reflections

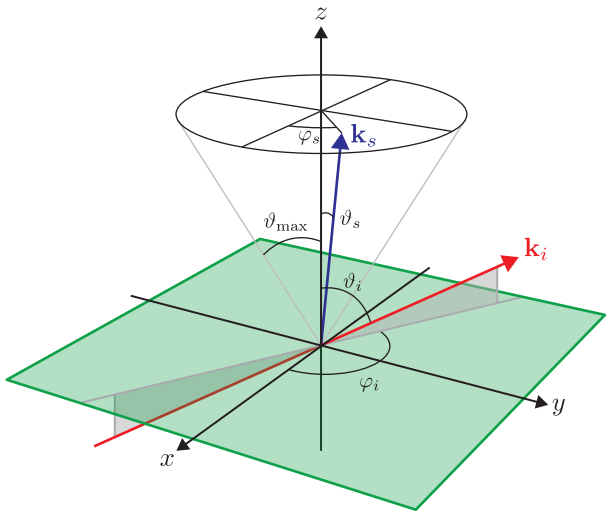

Figure 2.2: Geometry of the scattering problem. The center of the spherical particle is located at the origin.

from the cell windows are negligible.

In Eq. 2.3, the rotation matrix is defined as

$$\vec{R} = \begin{pmatrix} 1 & 0 & 0 & 0 \\ 0 & \cos 2\xi & \sin 2\xi & 0 \\ 0 & -\sin 2\xi & \cos 2\xi & 0 \\ 0 & 0 & 0 & 1 \end{pmatrix}, \tag{2.4}$$

where ξ is the angle between the normal of the plane defined by $\vec{k}_i$ and axis of the objective collecting the scattered light and the normal of the plane defined by $\vec{k}_i$ and $\vec{k}_s$.

In Eq. 2.3, the scattering matrix is defined as

$$\vec{M} = \frac{1}{k^2 r^2} \begin{pmatrix} S_{11} & S_{12} & 0 & 0 \\ S_{12} & S_{11} & 0 & 0 \\ 0 & 0 & S_{33} & S_{34} \\ 0 & 0 & -S_{34} & S_{33} \end{pmatrix}, \tag{2.5}$$

where r is the distance to the detector.

The elements of $\vec{M}$ are

$$\begin{aligned} S_{11} = \tfrac{1}{2}(|S_2|^2 + |S_1|^2), \quad S_{12} = \tfrac{1}{2}(|S_2|^2 - |S_1|^2), \\ S_{33} = \tfrac{1}{2}(S_2^* S_1 + S_2 S_1^*), \quad \text{and} \quad S_{34} = \tfrac{i}{2}(S_2^* S_1 + S_2 S_1^*), \end{aligned} \tag{2.6}$$

where S_1 and S_2, are defined as[3]

$$S_1 = \sum_{n=1}^{\infty} \frac{2n+1}{n(n+1)} (a_n \pi_n + b_n \tau_n), \tag{2.7}$$

$$S_2 = \sum_{n=1}^{\infty} \frac{2n+1}{n(n+1)} (a_n \tau_n + b_n \pi_n), \tag{2.8}$$

π_n and τ_n are the angular functions

$$\pi_n = \frac{P_n^1(\cos\Theta)}{\sin\Theta} \quad \text{and} \quad \tau_n = \frac{dP_n^1(\cos\Theta)}{d\Theta}, \tag{2.9}$$

(P_n^1 is the first order associated Legendre function) and a_n and b_n are the Mie scattering coefficients

$$a_n = \frac{m^2 j_n(mx)[x j_n(x)]' - j_n(x)[mx j_n(mx)]'}{m^2 j_n(mx)[x h_n^{(1)}(x)]' - h_n^{(1)}(x)[mx j_n(mx)]'} \tag{2.10}$$

and

$$b_n = \frac{j_n(mx)[x j_n(x)]' - j_n(x)[mx j_n(mx)]'}{j_n(mx)[x h_n^{(1)}(x)]' - h_n^{(1)}(x)[mx j_n(mx)]'}, \tag{2.11}$$

where m is the relative refractive index of the homogeneous sphere ($m = m_a/m_s$, where m_a is the refractive index of the sphere and m_s is the refractive index of the surrounding medium), x is the dimensionless size parameter ($x = ka$, where a is the radius of the spherical particle), j_n are spherical Bessel functions of the first kind and $h_n^{(1)}$ are Hankel functions of the first kind. Although Eqs. 2.7 and 2.8 are sums to infinity, during computations the series is truncated at the integer closest to $x + 4x^{1/3} + 2$.[3]

Evaluating Eq. 2.3 allows $\vec{S}_s$ to be found for any ϑ_s and φ_s. Based on the geometry in Fig. 2.2, in order to generate a phase function at the detector, $\vec{S}_s$ should be evaluated from $\varphi_s = 0$ to 360° and $\vartheta_s = 0$ to $\vartheta_{\max}$, where $\vartheta_{\max} = \arcsin(\mathrm{NA})$ and NA is the numerical aperture of the collection objective. Once $\vec{S}_s$ has been found for this range of ϑ_s and φ_s, the intensity at the detector can be readily calculated for unpolarized light, $I_{s,\mathrm{unpol}}$, parallel polarized light, $I_{s,\mathrm{par}}$, or perpendicularly polarized light, $I_{s,\mathrm{perp}}$ using the relationships

$$I_{s,\mathrm{unpol}} = I_s, \quad I_{s,\mathrm{par}} = (I_s + Q_s)/2, \quad \text{and} \quad I_{s,\mathrm{perp}} = (I_s - Q_s)/2. \tag{2.12}$$

The angular intensity distribution at the detector is the phase function.

In our experimental setup (Section 2.3), we measure light scattering from two counter-propagating beams. As shown in Fig. 2.1, the two counter-propagating beams are orthogonally polarized to each other due to the polarizing beamsplitter. When calculating phase functions, we treat light scattering from each beam independently and add the two resulting profiles together. One profile is reversed before the addition to account for the counter-propagation. However, because of the orthogonal polarizations of the two beams and the placement of our objective, it will be the case that the beam whose polarization is perpendicular to the plane defined by the detector axis and $\vec{k}_i$ will dominate the measured scattered intensity. Nevertheless, both beams are included in all calculations.

2.4.2 Mie resonances

Eqs. 2.10 and 2.11 can be used to calculate the positions of electric and magnetic modes for a homogeneous sphere (Mie resonances). Size parameters where the denominator of either equation goes to zero correspond to a Mie resonance.[11,57] The size parameters that satisfy the resonance condition have both a real and imaginary part, so we introduce the complex size parameter, z. The characteristic equation for Mie resonances can be compactly written as[10]

$$m\gamma\frac{j_n'(mz)}{j_n(mz)} = \frac{h_n^{(1)\prime}(z)}{h_n^{(1)}(z)} + \frac{1-\gamma}{z}, \tag{2.13}$$

where $\gamma = 1$ for transverse electric (TE) modes and $\gamma = 1/m^2$ for transverse magnetic (TM) modes. For a given value of m, the real part of z that satisfies Eq. 2.13 corresponds to a resonant size parameter, $x_{n,l,p}$, where n is the mode number, l is the mode order, and p is the

polarization of the mode (TE or TM). Modes are labeled with the notation p_n^l. For instance, the label for a TM mode with $n = 60$ and $l = 3$ would be TM_{60}^3. Methods for solving Eq. 2.13 for a given set of n, l, and p have been discussed in Ref. 10.

2.5 Phase function measurements

2D phase function images that were collected with a CMOS camera were first cropped to a square around the phase function removing much of the padding that contains no light scattering information. A representative cropped phase function is shown in Fig. 2.3a. Fig. 2.3b shows a simulated 2D phase function calculated using the method discussed in Section 2.4. The most distinct difference between the measured and calculated phase functions are the presence of the large number of concentric circles found in the intensity pattern of the measured phase function. These have been previously observed by several other authors.[32,52,58] They are the result of Fresnel diffraction by a circular aperture, although they have occasionally been misattributed to other optical phenomena (e.g. spherical aberration).

The Fresnel number is defined as $F = r_0^2/L\lambda$, where r_0 is the radius of the back aperture and L is the distance from the back aperture to the detector. The large size of the back aperture of the 20× collection objective, about 8 mm in diameter, and the distance from the aperture to the detector, about 40 cm, gives a high Fresnel number of $F = 75$ and places our imaging setup in the near-field diffraction range. Fig. 2.3c shows the calculated Fresnel diffraction for $F = 75$. The intensity pattern closely matches that which is superimposed on the observed 2D phase function in Fig. 2.3a. In principle, Fresnel diffraction could be

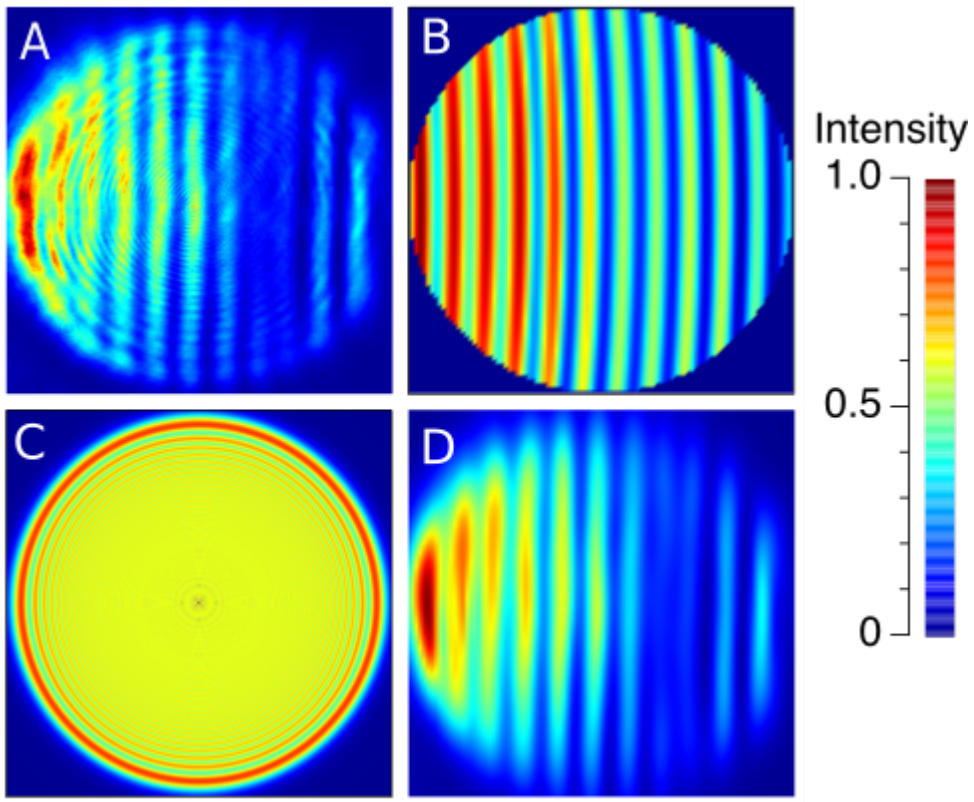

Figure 2.3: (a) Measured 2D phase function for an aqueous LiCl droplet held at 49% RH in the cell of the setup shown in Fig. 2.2, (b) Calculated 2D phase function for a particle with a radius of 3294 nm and a refractive index 1.40 (at $\lambda = 532$ nm), (c) Calculated Fresnel diffraction for $F = 75$, and (d) The 2D phase function from panel (a) after being treated with a low-pass filter to remove Fresnel diffraction.

incorporated into our phase function calculations (see pp. 727-728 of Ref. 59 for an outline of the appropriate methodology). However, such an inclusion would be very numerically intensive and it is much more straightforward to remove the unwanted effect of Fresnel diffraction by applying a low-pass filter to the columns of the measured phase function. This was done by processing measured phase functions with a built-in function in off-the-shelf software (Mathematica was used here). The cut-off frequency of the applied low-pass filter was chosen such that it removes the high frequency oscillations that appear in the measured phase function (the concentric circles) but does not have an effect on the lower frequency intensity oscillations that are characteristic of angular Mie scattering. Fig. 2.3d shows the result of applying a low-pass filter to the phase function shown in Fig. 2.3a.

1D phase functions were also constructed using the measured 2D phase functions (e.g. Fig. 2.3a). By taking pixels inside a circle that is centered on the cropped 2D phase function and whose diameter is equal to the size of the cropped image, the intensity of pixels in each column of this circle could then be averaged to generate a 1D phase function. This averaging also largely eliminates the Fresnel diffraction that is present in the 2D phase function. The edges of the 1D phase function tended to contain large amounts of noise due to the small number of pixels that would be used during the averaging. 2D phase functions were then compressed to 100 by 100 pixels to save computational time while the 1D phase functions were left at the original resolution of $\sim$ 500 pixels (this number is not constant because cropping changes the number of pixels from measurement to measurement).

2.6 Fitting measurements

2.6.1 Overview of fitting methodologies

Fitting 2D phase functions

Fig. 2.4a shows the measured phase function for a micrometer-sized aqueous LiCl droplet. As discussed in Section 2.5, the 2D phase function was processed with a low-pass filter to remove Fresnel diffraction from the image. In order to determine the radius of best-fit, $a_{\text{best-fit}}$, and refractive index of best-fit, $m_{\text{best-fit}}$, a simulated library of phase functions is generated across a physically reasonably range of a and m. Then, the correlation, c, between the measured 2D phase function and each of the simulated 2D phase functions is calculated. The correlation is defined as

$$c = \frac{N\sum x_i y_i - \sum x_i \sum y_i}{\sqrt{N\sum x_i^2 - (\sum x_i)^2}\sqrt{N\sum y_i^2 - (\sum y_i)^2}}. \tag{2.14}$$

where each pair of points, (x_i, y_i), consists of the measured and simulated scattered intensity located at one pixel i in the phase function and N is the total number of points in the set (the total number of pixels).

The values of a and m associated with the simulated phase function that yields the maximum value of c will be $a_{\text{best-fit}}$ and $m_{\text{best-fit}}$, respectively. Maximizing correlation in order to determine best-fits has been used by other authors when fitting phase functions.[31,39] Fig. 2.4b shows c as a function of a and m in the region near $a_{\text{best-fit}}$ and $m_{\text{best-fit}}$. The values

of a and m that yield the highest c (the best-fit) are $a_{\text{best-fit}} = 3103$ nm and $m_{\text{best-fit}} = 1.4229$. However, there are nearby bands that also have local maxima in c. Furthermore, the maximum value of c is 0.897 and is closer to the maximum value of c in one of the other bands than it is to the ideal correlation of one for a perfect fit. Specifically, there is a nearby local maximum that is located at $a = 3061$ nm and $m = 1.3765$ where $c = 0.863$. The implications of local maxima with correlations that are very similar to the global maximum are that small changes to how the measured phase function is processed or the parameters used to generate the simulated phase function can lead to one of these local maxima turning into the global maximum. This will affect the accuracy of the parameters of best-fit retrieved by fitting phase functions and will be discussed in detail in Sections 2.6.2 and 2.6.3.

Fitting 1D Phase Functions

As was discussed in Section 2.5, 1D phase functions can be constructed from 2D phase functions. Using that methodology, 1D phase functions were constructed from measured 2D phase functions and their correlation with simulated 1D phase functions was calculated with Eq. 2.14. Fig. 2.4c shows a 1D phase function and Fig. 2.4d contains the corresponding correlation map. Here, $a_{\text{best-fit}} = 3116$ nm and $m_{\text{best-fit}} = 1.4178$ but, similar to what was found when fitting 2D phase functions, there are nearby bands that have local maxima in c that are close. This potential for inaccuracy when fitting 1D phase functions has been noted previously.[60] For the 2D and 1D phase functions fits (Fig. 2.4b and d), the best-fits are similar but not identical.

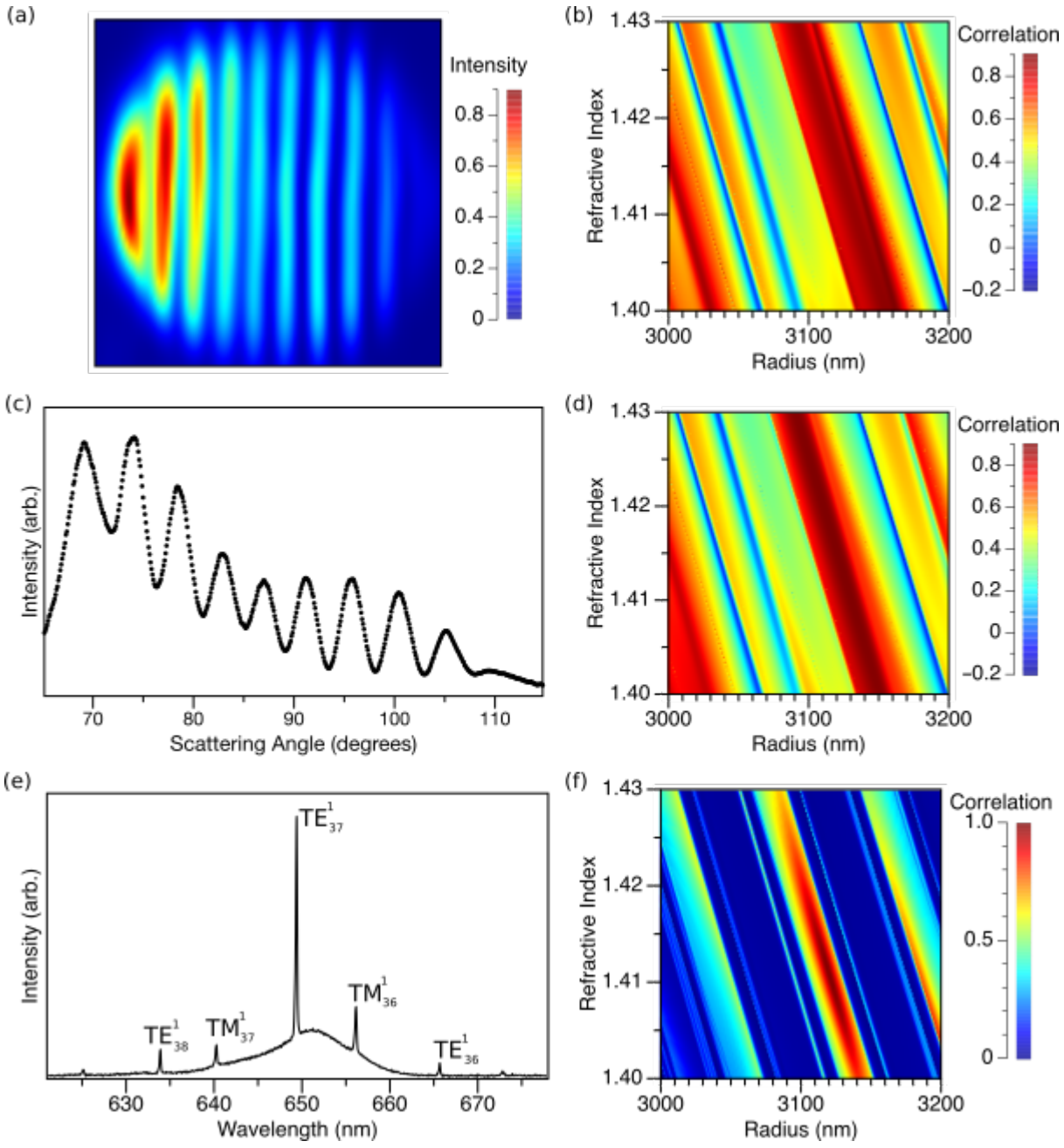

Figure 2.4: Examples of measurements and best-fit searches for an aqueous LiCl droplet held at 37% relative humidity. (a) Filtered 2D phase function (b) correlation for radius and refractive index combinations for the 2D phase function (c) 1D phase function (d) correlation for radius and refractive index combinations for the 1D phase function (e) Raman spectrum with Mie resonances (f) correlation for combinations of radius and refractive index for the positions of the Mie resonances.

Fitting Mie resonances in CERS spectra

Fig. 2.4e shows the CERS spectrum for the same micrometer-sized aqueous droplet whose phase functions were discussed above. Sharp peaks on top of the spontaneous Raman band are associated with the excitation of Mie resonances. Using only these peak positions ($\lambda =$ 633.90, 640.27, 649.39, 656.15, and 665.67 nm), $a_{\text{best-fit}}$ and the now wavelength-dependent $m_{\text{best-fit}}$ can quickly be found using MRFIT.[10,61] They are $a_{\text{best-fit}} = 3120.8$ nm and $m_{\text{best-fit}} =$ 1.4107 (at $\lambda = 532$ nm). The mode assignments corresponding to the best-fit are indicated in Fig. 2.4e.

With MRFIT, best-fits are found by minimizing the sum of squared residuals rather than maximizing correlation. For the purpose of comparing the correlation maps shown for the phase function fits, in Fig. 2.4f we have calculated c for the Mie resonance dataset as a function of a and m near $a_{\text{best-fit}}$ and $m_{\text{best-fit}}$. The definition of c that was used to generate Fig. 2.4f was the one given by Eversole *et al.*.[7] As expected, the best-fit obtained by maximizing c was identical to that obtained by minimizing the sum of squared residuals. Unlike the phase function best-fits, c at the global maximum is nearly one when fitting the Mie resonances ($c = 0.999$). Fig. 2.4f shows the correlation near the region of the best-fit. The high correlation bands are much sharper than those associated with the phase function fits. The peak correlation of the next band with a local maximum in c is less than 0.9. Therefore, even if a fairly coarse grid search across a and m is employed, accurate values of $a_{\text{best-fit}}$ and $m_{\text{best-fit}}$ are still achievable when fitting Mie resonances.

2.6.2 The effect of collection geometry and image processing on phase function best-fits

Obtaining best-fits for homogeneous spherical particles from either phase functions or Mie resonances relies on fitting light scattering measurements with Mie theory. In principle, one would expect little to no discrepancy between the best-fits obtained with either method. In practice, this is not the case (as is demonstrated in Section 2.6.3). One key difference is that, unlike best-fits found using Mie resonance peak positions in CERS spectra, obtaining accurate best-fits from phase functions requires knowledge of additional parameters in order to generate simulated phase functions. Furthermore, measured phase functions require more elaborate processing prior to fitting, whereas with CERS measurements the only analysis that is required is finding the location of the Mie resonance peak positions.

Concerning the requirement of additional parameters, accurate knowledge of the positioning of the collection objective and its NA are needed to properly simulate phase functions. We recently discussed this issue in the context of fitting broadband light scattering measurements.[17] In that work, it was found that small angular offsets in a right-angle collection geometry could lead to poor parameters of best-fit if not properly accounted for in simulated spectra. Here, we explore the effect of geometry on phase function fitting in Fig. 2.5 and 2.6. In Fig. 2.5, the effect of changing the NA of the collection objective on $a_{\text{best-fit}}$, $m_{\text{best-fit}}$, and the maximum value of c are shown. The NA was varied between 0.30 and 0.50 which corresponds to 15° to 110° cone angles. What is surprising in Fig. 2.5 is that c is not maximized for the true NA of the collection objective (NA = 0.42). Instead, local maxima

in c are located at NA 0.340, 0.380, 0.395, 0.415 and 0.440, but NAs of 0.340, 0.415 and 0.440 are physically unreasonable for our collection geometry. For the case of NA = 0.38, the best-fit yields $a_{\text{best-fit}} = 2720$ nm and $m_{\text{best-fit}} = 1.429$. This lower 'effective' NA is physically plausible as Fresnel diffraction causes the intensity of the phase function to drop off significantly as it approaches ϑ_{max} (i.e. the edge of the phase function that is predicted by the NA of the collection objective using geometric optics). Consequently, when cropping measured phase functions it is likely that too many pixels will be removed near the outer edge of the measured phase function. This results in an effective NA that is lower than the actual NA of the collection objective. Additionally, imaging the particle out of plane results in a change of the effective NA. In our experiments, the images were taken with the focal point of the collection objective in a plane between the particle and the objective which would also decrease the effective NA.

In Fig. 2.6, we examine the effect of the collection geometry on the best-fit when the NA of the collection objective is held constant at 0.42. This is most easily explored by varying the angle ϑ_i (see Fig. 2.2). Ideally, with the right-angle geometry that we have used to collect the angular light scattering, ϑ_i should be 90°. In practice, this angle may be offset from 90° if the collection objective is not oriented exactly at 90° to the path of the incident beam. However, the offset cannot be too large as the measured image will begin to visibly distort and the resulting phase function will no longer appear circular. This makes identifying and correcting for any large offset straightforward as high quality, circular images can only be collected when the lens of the collection objective are parallel to the trapping cell window. In Fig. 2.6, the effect of varying ϑ_i between 80° and 100° on the maximum

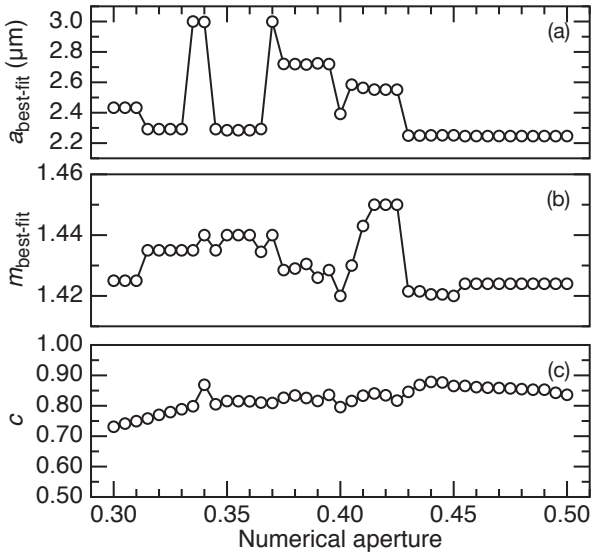

Figure 2.5: An example of the effect of changing numerical aperture on (a) the radius of best-fit, $a_{\text{best-fit}}$, (b) the refractive index of best-fit, $m_{\text{best-fit}}$, and (c) the correlation, c, associated with the best-fit, for a 2D phase function at 22% RH. The lines are added to guide the eye.

value of c and the best-fits at each ϑ_i are shown. For the ϑ_i that has the highest overall value of c, $a_{\text{best-fit}} = 2186.8$ nm and $m_{\text{best-fit}} = 1.420$. The value of ϑ_i that yields the maximum c is 88°. This best-fit is considerably different from that retrieved by varying the NA (Fig. 2.5). We also investigated the effect of varying the angle φ_i but small offsets in this angle had no effect on the retrieved best-fits. Finally, when taking measurements, the effective NA and ϑ_i that gave the highest correlations were found to vary slightly after the collection objective was moved to center the particle on the CMOS camera.

We also considered the possibility that the incident beam is not well described as a plane wave. In order to examine this, phase functions were generated using generalized Lorenz-Mie theory (GLMT)[62–64] for a Gaussian beam.[65] Fig. 2.7 shows the 1D phase function for a particle located at the focal point of Gaussian beam with a beam waist of 4.3 μm. The beam

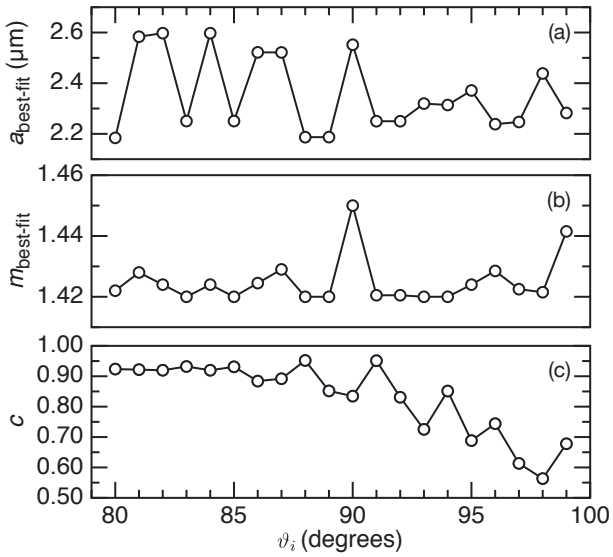

Figure 2.6: An example of the effect of changing ϑ_i on (a) the radius of best-fit, $a_{\text{best-fit}}$, (b) the refractive index of best-fit, $m_{\text{best-fit}}$, and (c) the correlation, c, associated with the best-fit. For all fits, the NA is held constant at 0.42 for a 2D phase function at 22% RH. The lines are added to guide the eye.

waist chosen for this calculation was the waist at the focal point of trap and was measured experimentally using the knife-edge method.[50,66] The size and refractive index of the particle used in the calculation were $a = 3$ μm and $m = 1.4$. While the intensities across the angular range differ between the plane wave and Gaussian beam calculations, the overall shape of the two plots is similar. The correlation between the plane-wave and Gaussian scattering is 0.981 in Fig. 2.7a and 0.997 in Fig. 2.7b. Therefore, there will be little difference in the value of c obtained if the incident beam is treated as a Gaussian beam rather than a plane wave and the plane wave approximation that we use throughout this work appears to be satisfactory.

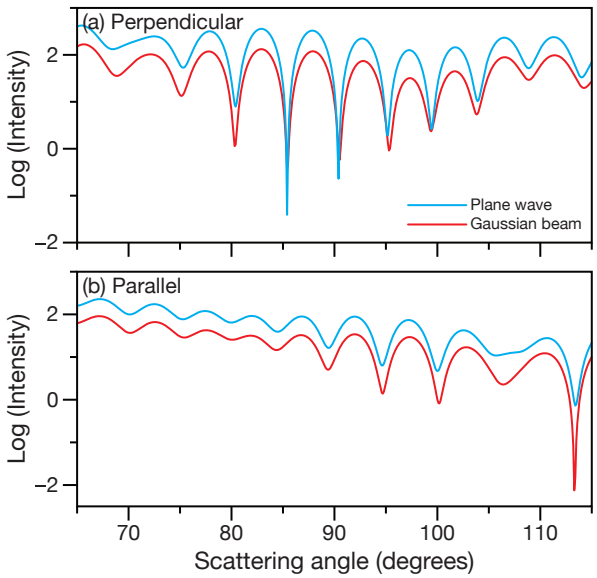

Figure 2.7: 1D phase functions calculated using either Mie theory or generalized Lorenz-Mie theory (GLMT). GLMT calculations were performed using a Gaussian beam with the spherical particle located at the focal point of the beam. The radius and refractive index of the particle were 3 μm and 1.4, respectively. The wavelength of light was 532 nm and the beam waist for the GLMT calculation was 4.3 μm (the same as our optical trap). The log of the scattered light intensity for light polarized (a) perpendicular and (b) parallel to the scattering plane is plotted across the angular range that would be collected by a lens with NA = 0.42 located at 90° to the incident beam.

2.6.3 Accuracy of fitting methodologies

In atmospheric science, optical tweezers are commonly used to study the hygroscopicity of aerosol particles due to the excellent accuracy and high sensitivity of measurements.[67,68] Hygroscopic growth can be investigated by trapping a single particle in an RH controlled cell and monitoring changes to a and m in response to stepwise changes in RH.[69] As we have already discussed, both a and m can simultaneously be found by fitting either 1D phase functions, 2D phase functions, or Mie resonance peaks in CERS spectra. Fig. 2.8 shows measurements from a hygroscopic growth experiment for an aqueous LiCl droplet. Fig. 2.8a shows the RH in the cell as a function of time over the course of the experiment. During this time, both elastic angular light scattering and Raman scattering are simultaneously collected. Fig. 2.8b shows the peak positions extracted from CERS spectra and Fig. 2.8c and d show representative 1D and 2D phase functions at four experimental RHs that the trapped particle was in equilibrium with.

Measurements from the hygroscopic growth experiment were fitted using the methodology discussed in Section 2.6.1 and the resulting $a_{\text{best-fit}}$ and $m_{\text{best-fit}}$ are shown Figs. 2.9 and 2.10, respectively. As discussed in Section 2.6.2, the effective NA and true value of ϑ_i will be slightly different than their ideal values and this can impact the retrieved best-fits. Therefore, when fitting phase functions, both the NA and ϑ_i were allowed to vary within physically plausible bounds in order to maximize correlation. Note that if the NA and ϑ_i were simply fixed at their ideal values (NA $= 0.42$ and $\vartheta_i = 90°$), the accuracy of the best-fits for the phase functions was much worse than that which is shown in Figs. 2.9 and 2.10.

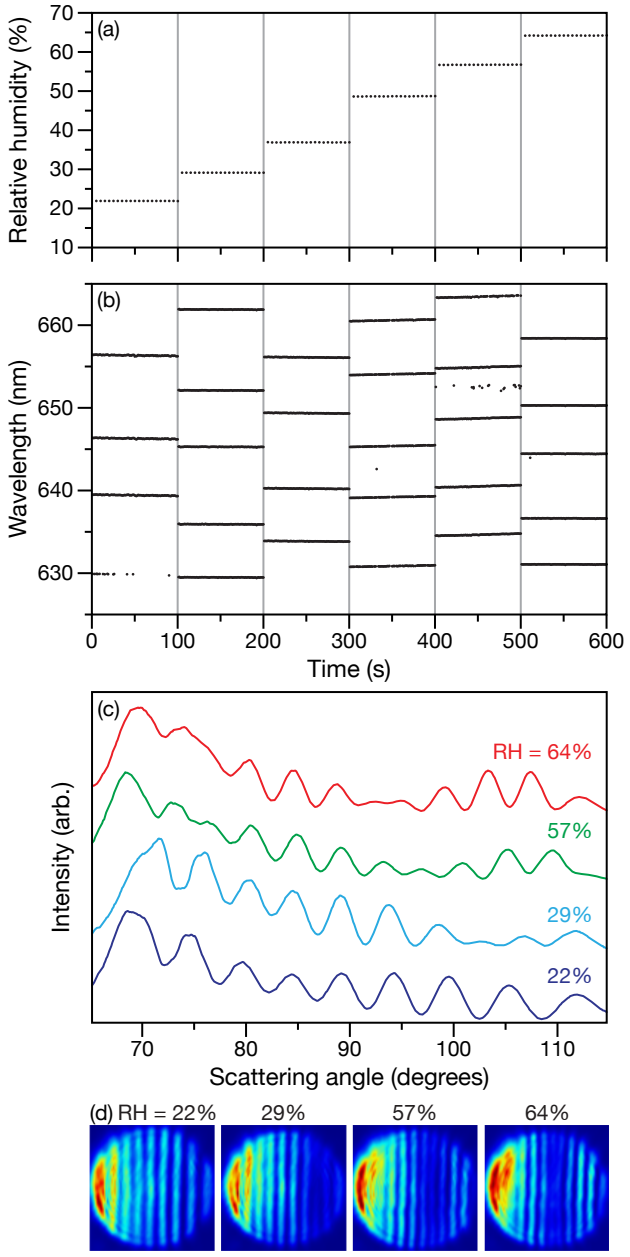

Figure 2.8: (a) Relative humidity (RH) in the trapping cell over time. The RH is measured every 5 s. (b) Positions of Mie resonances in collected Raman spectra of an optically trapped aqueous LiCl droplet that is equilibrated with the surrounding RH listed in panel (a). Raman spectra are recorded every 1 s. Note that there is a break between datasets, at the vertical lines, to allow the cell to come back to equilibrium after changing the RH. Examples of (c) 1D and (d) 2D phase functions for 22, 29, 57 and 64% RH. In (c), the 1D phase functions are offset for clarity.

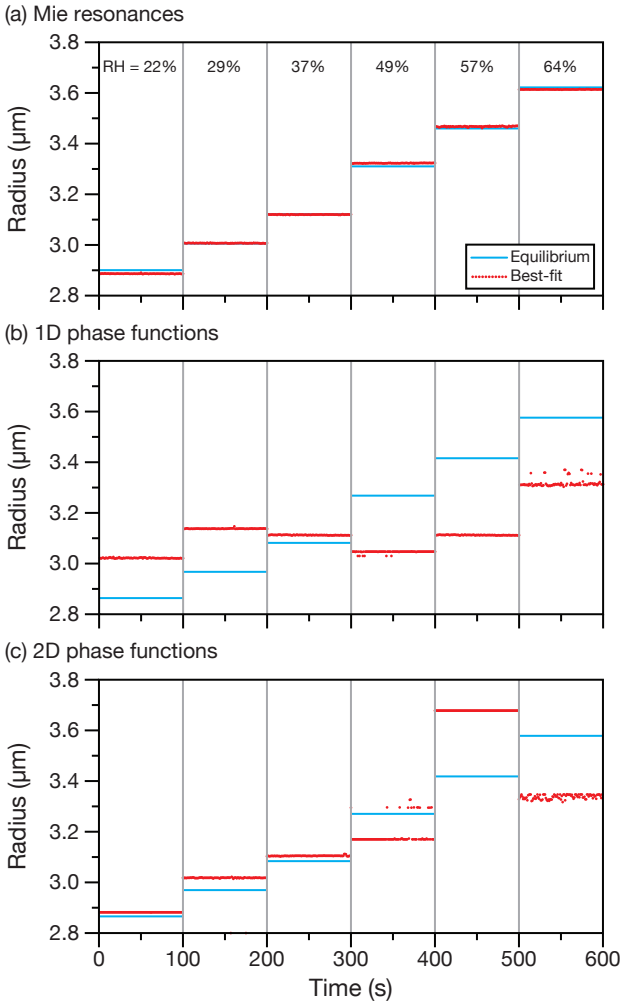

Figure 2.9: The radius of best-fit, $a_{\text{best-fit}}$, for aqueous LiCl droplets at several different relative humidities. Best-fits were found using either (a) Mie resonances, (b) 1D phase functions, or (c) 2D phase functions. Best-fits are compared to equilibrium radii calculated using AIOMFAC[70] and the tabulated density of aqueous LiCl.[71]

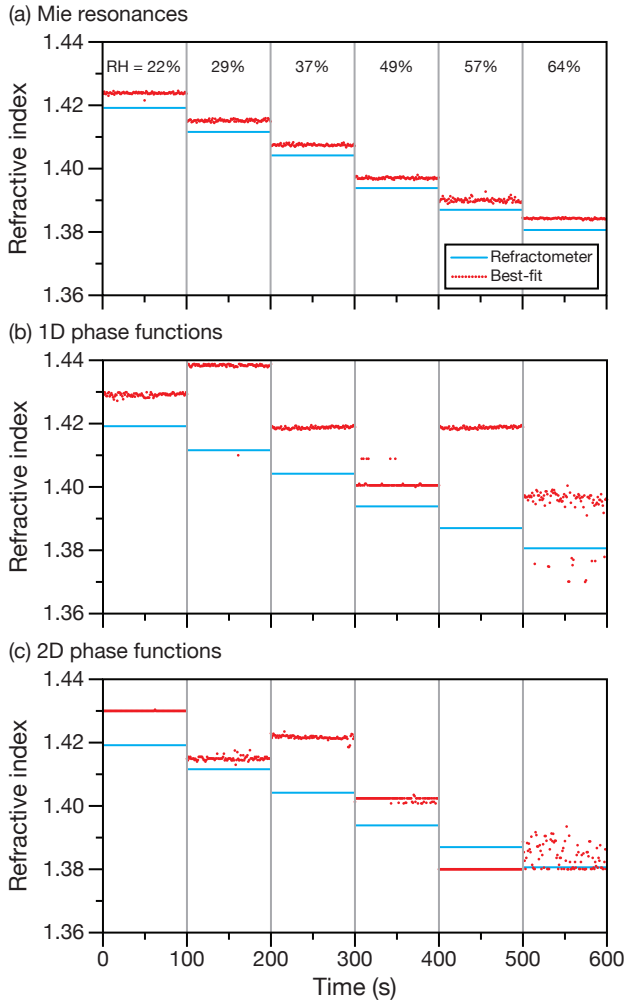

Figure 2.10: The refractive index of best-fit, $m_{\text{best-fit}}$, for aqueous LiCl droplets at several different relative humidities. Best-fits were found using either (a) Mie resonances (at $\lambda = 589$ nm), (b) 1D phase functions (at $\lambda = 532$ nm), or (c) 2D phase functions (at $\lambda = 532$ nm). Best-fits are compared to the refractive index for a solution of aqueous LiCl measured with an Abbe refractometer (at $\lambda = 589$ nm).[72] Droplet composition is calculated using AIOMFAC.[70]

The composition of an aqueous droplet containing an inorganic solute that is in equilibrium with its surrounding water vapor can be accurately calculated as a function of water activity using a thermodynamic model (AIOMFAC was used here).[70] Therefore, for any RH, we can determine the amount of water and LiCl in the particle. Then, the density and refractive index of the aqueous LiCl droplet can be compared to previously reported measurements.[71,72] The predicted refractive index taken from refractometer measurements for aqueous solutions can be directly compared to $m_{\text{best-fit}}$ for the droplet (Fig. 2.10). In Fig. 2.9 we compare our $a_{\text{best-fit}}$ to radii that were calculated using AIOMFAC and the tabulated density of aqueous LiCl. In order to use the density to calculate the equilibrium droplet radius as a function of RH at least one value of the radius must be known. As the true radius of the droplet is never known during this experiment, in Fig. 2.9a-c we have chosen an initial droplet radius that minimizes the error between the calculated and measured radii across all RHs. In Fig. 2.9a, the match between the equilibrium radii and $a_{\text{best-fit}}$ found using the Mie resonances is excellent. In contrast, both the phase function best-fits (Fig. 2.9b and c) are quite poor when compared to the calculated equilibrium radii. The phase function best-fits are also not self-consistent. Based on thermodynamics, one expects that the size of the droplet will only increase with increasing RH. However, in both Fig. 2.9b and c this behavior is not always observed.

In Fig. 2.10, $m_{\text{best-fit}}$ is compared to the refractive index calculated using refractometer measurements of an aqueous solution for the equilibrium droplet compositions at each RH. In Fig. 2.10a, the correspondence between the refractometer refractive index and the best-fits are good, although $m_{\text{best-fit}}$ is on average 0.004 dimensionless units greater than

the refractometer refractive index. Due to dispersion, $m_{\text{best-fit}}$ for the phase functions was expected to be slightly higher than the refractometer refractive index as the phase functions were measured at a shorter wavelength ($\lambda = 532$ nm for the phase function measurements and $\lambda = 589$ nm for the refractometer measurements). This can account for some of the inaccuracy seen in $m_{\text{best-fit}}$ in Fig. 2.10b and c as the best-fits are larger than the refractometer refractive index (with the exception of $m_{\text{best-fit}}$ at RH = 57% in Fig. 2.10c). However, this consideration does not explain the lack of self-consistency in $m_{\text{best-fit}}$ across the various RHs. Just as was seen with the radii of best-fit that were calculated using the phase functions, the refractive index of best-fit does not show the physically expected behavior with changing RH. In summary, from Figs. 2.9 and 2.10 it can be seen that the phase function best-fits have comparable precision to the Mie resonance best-fits (with the exception of the RH = 64% best-fits which have greater uncertainty) but the overall accuracy of the phase function best-fits compares poorly to the accuracy of the Mie resonance best-fits.

2.7 Conclusion

Our focus here has been on retrieving radii and refractive indices of best-fit using two different light scattering methodologies. While it is clear that Mie resonances can provide more accurate best-fits than phase functions, there are other considerations that were not discussed in our assessment of the techniques that are worth summarizing here. First, the spectrograph and CCD that were used to measure CERS spectra are much more expensive than the CMOS camera that was used to record phase function measurements. Therefore, cost may prohibit

the use of CERS measurements in single particle experiments. Second, depending on the composition of the particle, the spontaneous Raman band may be too narrow to allow for a sufficient number of Mie resonance peaks to be observed (at least three peaks are required).[17] Third, as particle size decreases, the spacing between Mie resonances increases and, again, this can lead to a situation where an insufficient number of Mie resonance peaks are observed. When using CERS with aqueous particles, this typically occurs as the radius falls below 3 μm.[17,32,58] In contrast, with phase function analysis it is possible to characterize much smaller particles, even below 500 nm in radius.[32,58] Of course, there are other methods to obtain Mie resonance positions, such as broadband light scattering,[17,26] that do not suffer from the same limitations as CERS. Fourth, fitting Mie resonances will yield a wavelength-dependent refractive index and there are many situations where this is useful (e.g. other refractive index data in the literature may have been measured at different wavelengths and knowledge of dispersion will facilitate a direct comparison). Fifth, in certain collection geometries it will be necessary to use 2D phase functions rather than 1D phase functions. See Ref. 31 for one such example. For the geometry used here, fitting 2D phase functions only gave a small accuracy improvement over fitting 1D phase functions.

In summary, whenever possible, Mie resonances should be used when determining the size and refractive index of optically trapped particles. While both Mie resonance and phase function best-fits have comparably high precisions, the accuracy of the phase function best-fits calculated using either 1D or 2D phase functions is much worse than the accuracy of the Mie resonance best-fits. The origin of these inaccuracies may be largely to do with the additional parameters needed when generating simulated phase functions during the

fitting process. Specifically, the effective NA and ϑ_i. As was discussed in Section 2.6.1, the accurate calculation of Mie resonance positions observed in CERS spectra does not require these additional parameters and the best-fits do not suffer from the same difficulties that affect the phase function fitting process.

References

[1] Boucher, O. et al. Clouds and Aerosols. *Climate Change 2013: The Physical Science Basis. Contribution of Working Group I to the Fifth Assessment Report of the Intergovernmental Panel on Climate Change* **2013**, 571–657.

[2] Mie, G. Beiträge zur optik trüber medien, speziell kolloidaler metallösungen. *Annalen der Physik* **1908**, *330*, 377–445.

[3] Bohren, C. F.; Huffman, D. R. *Absorption and Scattering of Light by Small Particles*; Wiley-VCH, 1983.

[4] Ashkin, A.; Dziedzic, J. M. Observation of optical resonances of dielectric spheres by light scattering. *Appl. Opt.* **1981**, *20*, 1803–1814.

[5] Lam, C. C.; Leung, P. T.; Young, K. Explicit asymptotic formulas for the positions, widths, and strengths of resonances in Mie scattering. *J. Opt. Soc. Am. B* **1992**, *9*, 1585–1592.

[6] Symes, R.; Sayer, R. M.; Reid, J. P. Cavity enhanced droplet spectroscopy: Principles, perspectives and prospects. *Phys. Chem. Chem. Phys.* **2004**, *6*, 474–487.

[7] Eversole, J. D.; Lin, H. B.; Huston, A. L.; Campillo, A. J.; Leung, P. T.; Liu, S. Y.; Young, K. High-precision identification of morphology-dependent resonances in optical processes in microdroplets. *J. Opt. Soc. Am. B* **1993**, *10*, 1955–1968.

[8] Roll, G.; Schweiger, G. Geometrical optics model of Mie resonances. *J. Opt. Soc. Am. A* **2000**, *17*, 1301–1311.

[9] Preston, T. C.; Reid, J. P. Accurate and efficient determination of the radius, refractive index, and dispersion of weakly absorbing spherical particle using whispering gallery modes. *J. Opt. Soc. Am. B* **2013**, *30*, 2113–2122.

[10] Preston, T. C.; Reid, J. P. Determining the size and refractive index of microspheres using the mode assignments from Mie resonances. *J. Opt. Soc. Am. A* **2015**, *32*, 2210–2217.

[11] Chýlek, P.; Kiehl, J. T.; Ko, M. Narrow resonance structure in the Mie scattering characteristics. *Appl. Opt.* **1978**, *17*, 3019–3021.

[12] Dlugach, J. M.; Mishchenko, M. I. Effects of nonsphericity on the behavior of Lorenz-Mie resonances in scattering characteristics of liquid-cloud droplets. *J. Quant. Spectrosc. Radiat. Transfer* **2014**, *146*, 227 – 234.

[13] Dennis-Smither, B. J.; Marshall, F. H.; Miles, R. E. H.; Preston, T. C.; Reid, J. P. Volatility and oxidative aging of aqueous maleic acid aerosol droplets and the dependence on relative humidity. *J. Phys. Chem. A* **2014**, *118*, 5680–5691.

[14] Lin, H.-B.; Campillo, A. J. Radial profiling of microdroplets using cavity-enhanced Raman spectroscopy. *Opt. Lett.* **1995**, *20*, 1589–1591.

[15] Moore, L. J.; Summers, M. D.; Ritchie, G. A. D. Optical trapping and spectroscopic characterisation of ionic liquid solutions. *Phys. Chem. Chem. Phys.* **2013**, *15*, 13489–13498.

[16] Vaughn, B. S.; Tracey, P. J.; Trevitt, A. J. Drop-on-demand microdroplet generation: a very stable platform for single-droplet experimentation. *RSC Adv.* **2016**, *65*, 60215–60222.

[17] Lew, L. J. N.; Ting, M. V.; Preston, T. C. Determining the size and refractive index of homogeneous spherical aerosol particles using Mie resonance spectroscopy. *Appl. Opt.* **2018**, *57*, 4601–4609.

[18] Ward, A. D.; Berry, M. G.; Mellor, C. D.; Bain, C. D. Optical sculpture: controlled deformation of emulsion droplets with ultralow interfacial tensions using optical tweezers. *Chem. Comm.* **2006**, *16*, 16390–16403.

[19] Guillon, M.; Miles, R. E.; Reid, J. P.; McGloin, D. Thermo-optical resonance locking of an optically trapped salt-water microdroplet. *New J. Phys.* **2009**, *11*, 1–10.

[20] Wills, J. B.; Knox, K. J.; Reid, J. P. Optical control and characterisation of aerosol. *Chem. Phys. Lett.* **2009**, *481*, 153–165.

[21] Knox, K. J.; Reid, J. P. Ultrasensitive absorption spectroscopy of optically-trapped aerosol droplets. *J. Phys. Chem. A* **2008**, *112*, 10439–10441.

[22] Miles, R. E. H.; Walker, J. S.; Burnham, D. R.; Reid, J. P. Retrieval of the complex refractive index of aerosol droplets from optical tweezers measurements. *Phys. Chem. Chem. Phys.* **2012**, *14*, 3037–3047.

[23] Li, J.; Chýlek, P. Resonances of a dielectric sphere illuminated by two counterpropagating plane waves. *J. Opt. Soc. Am. A* **1993**, *10*, 687–692.

[24] Conwell, P. R.; Rushforth, C. K.; Benner, R. E.; Hill, S. C. Efficient automated algorithm for the sizing of dielectric microspheres using the resonance spectrum. *J. Opt. Soc. Am. A* **1984**, *1*, 1181–1187.

[25] Hill, S. C.; Rushforth, C. K.; Benner, R. E.; Conwell, P. R. Sizing dielectric spheres and cylinders by aligning measured and computed resonance locations: algorithm for multiple orders. *Appl. Opt.* **1985**, *24*, 2380–2390.

[26] Jones, S. H.; King, M. D.; Ward, A. D. Determining the unique refractive index properties of solid polystyrene aerosol using broadband Mie scattering from optically trapped beads. *Phys. Chem. Chem. Phys.* **2013**, *15*, 20735–20741.

[27] Jones, S. H.; King, M. D.; Ward, A. D. Atmospherically relevant core–shell aerosol studied using optical trapping and Mie scattering. *Chem. Comm.* **2015**, *51*, 4914–4917.

[28] Graßmann, A.; Peters, F. Size measurement of very small spherical particles by Mie scattering imaging (MSI). *Part. Part. Syst. Charact.* **2004**, *21*, 379–389.

[29] Glover, A. R.; Skippon, S. M.; Boyle, R. D. Interferometric laser imaging for droplet sizing: a method for droplet-size measurement in sparse spray systems. *Appl. Opt.* **1995**, *34*, 8409–8421.

[30] Derkachov, G.; Jakubczyk, D.; Woźniak, M.; Archer, J.; Kolwas, M. High-precision temperature determination of evaporating light-absorbing and non-light-absorbing droplets. *J. Phys. Chem. B* **2014**, *118*, 12566–12574.

[31] Rothe, T.; Schmitz, M.; Kienle, A. Angular and spectrally resolved investigation of single particles by darkfield scattering microscopy. *J. Biomed. Opt.* **2012**, *17*, 117006.

[32] Carruthers, A. E.; Walker, J. S.; Casey, A.; Orr-Ewing, A. J.; Reid, J. P. Selection and characterization of aerosol particle size using a Bessel beam optical trap for single particle analysis. *Phys. Chem. Chem. Phys.* **2012**, *14*, 6741–6748.

[33] Meresman, H.; Wills, J. B.; Summers, M.; McGloin, D.; Reid, J. P. Manipulation and characterization

of accumulation and coarse mode aerosol particles using a Bessel beam trap. *Phys. Chem. Chem. Phys.* **2009**, *11*, 11333–11339.

[34] Barnes, M. D.; Lermer, N.; Whitten, W. B.; Ramsey, J. M. A CCD based approach to high-precision size and refractive index determination of levitated microdroplets using Fraunhofer diffraction. *Rev. Sci. Instrum.* **1997**, *68*, 2287–2291.

[35] Rothe, T.; Schmitz, M.; Kienle, A. Angular Resolved Scattering Microscopy. *Advanced Microscopy Techniques II* **2011**, *8086*, 1–6.

[36] Berg, M. J.; Hill, S. C.; Videen, G.; Gurton, K. P. Spatial filtering technique to image and measure two-dimensional near-forward scattering from single particles. *Opt. Express* **2010**, *18*, 9486–9495.

[37] Smith, Z. J.; Berger, A. J. Validation of an integrated Raman- and angular-scattering microscopy system on heterogeneous bead mixtures and single human immune cells. *Appl. Opt.* **2009**, *48*, D109–D120.

[38] König, G.; Anders, K.; Frohn, A. A new light-scattering technique to measure the diameter of periodically generated moving droplets. *J. Aerosol Sci.* **1986**, *17*, 157–167.

[39] Preston, T. C.; Reid, J. P. Angular scattering of light by a homogeneous spherical particle in a zeroth-order Bessel beam and its relationship to plane wave scattering. *J. Opt. Soc. Am. A Opt. Image Sci. Vis.* **2015**, *32*, 1053–1062.

[40] Schmitz, M.; Rothe, T.; Kienle, A. Evaluation of a spectrally resolved scattering microscope. *Biomed. Opt. Express* **2011**, *2*, 2665–2678.

[41] Braun, C.; Krieger, U. K. Two–dimensional angular light–scattering in aqueous NaCl single aerosol particles during deliquescence and efflorescence. *J. Geophys. Res* **1999**, *104285*, 275–21.

[42] Davis, E. J.; Ravindran, P. Single particle light scattering measurements using the electrodynamic balance. *Aerosol Science and Technology* **1982**, *1*, 337–350.

[43] Tang, I. N.; Munkelwitz, H. R. Simultaneous determination of refractive index and density of an evaporating aqueous solution droplet. *Aerosol Science and Technology* **1991**, *15*, 201–207.

[44] Liu, F.; Zhang, Z.; Wei, Y.; Zhang, Q.; Cheng, T.; Wu, X. Photophoretic trapping of multiple particles in tapered-ring optical field. *Optics Express* **2014**, *22*, 23716.

[45] Redding, B.; Hill, S. C.; Alexson, D.; Wang, C.; Pan, Y.-L. Photophoretic trapping of airborne particles using ultraviolet illumination. *Optics Express* **2015**, *23*, 3630–3639.

[46] Wang, C.; Pan, Y. L.; Hill, S. C.; Redding, B. Photophoretic trapping-Raman spectroscopy for single pollens and fungal spores trapped in air. *Journal of Quantitative Spectroscopy and Radiative Transfer* **2015**, *153*, 4–12.

[47] Ashkin, A.; Dziedzic, J. M. Optical levitation by radiation pressure. *Applied Physics Letters* **1971**, *19*, 283–285.

[48] Suzuki, H.; Matsuzaki, Y.; Muraoka, A.; Tachikawa, M. Raman spectroscopy of optically levitated supercooled water droplet. *Journal of Chemical Physics* **2012**, *136*.

[49] Jones, P. H.; Maragò, O. M.; Volpe, G. *Optical Tweezers: Principles and Applications*; Cambridge University Press, 2015.

[50] Rafferty, A.; Preston, T. C. Measuring the size and complex refractive index of an aqueous aerosol particle using electromagnetic heating and cavity-enhanced Raman scattering. *Phys. Chem. Chem. Phys.* **2018**, *20*, 17038–17047.

[51] Ashkin, A.; Dziedzic, J. M.; Bjorkholm, J. E.; Chu, S. Observation of a single-beam gradient force optical trap for dielectric particles. *Optics Letters* **1986**, *11*, 288.

[52] Lu, J. W.; Isenor, M.; Chasovskikh, E.; Stapfer, D.; Signorell, R. Low-temperature Bessel beam trap for single submicrometer aerosol particle studies. *Rev. Sci. Instrum.* **2014**, *85*, 095107 1–9.

[53] Li, P.; Shi, K.; Liu, Z. Manipulation and spectroscopy of a single particle by use of white-light optical tweezers. *Optics Letters* **2005**, *30*, 156–158.

[54] Zang, D.; Yu, Y.; Chen, Z.; Li, X.; Wu, H.; Geng, X. Acoustic levitation of liquid drops: Dynamics, manipulation and phase transitions. *Advances in Colloid and Interface Science* **2017**, *243*, 77–85.

[55] Onofri, F. R. A.; Ren, K. F.; Sentis, M.; Gaubert, Q.; Pelcé, C. Experimental validation of the vectorial complex ray model on the inter-caustics scattering of oblate droplets. *Opt. Express* **2015**, *23*, 15768–15773.

[56] Mason, B. J.; Cotterell, M. I.; Preston, T. C.; Orr-Ewing, A. J.; Reid, J. P. Direct measurements of

the optical cross sections and refractive indices of individual volatile and hygroscopic aerosol particles. *J. Phys. Chem. A* **2015**, *119*, 5701–5713.

[57] Chýlek, P. Resonance structure of Mie scattering: distance between resonances. *Journal of the Optical Society of America A* **1990**, *7*, 1609–1613.

[58] Carruthers, A. E.; Reid, J. P. Longitudinal optical trapping and sizing of aerosol droplets. *Opt. Express* **2010**, *18*, 14238–14244.

[59] Siegman, A. E. *Lasers*; University Science Books: Mill Valley, California, 1986.

[60] Lu, J. W.; Rickards, A. M. J.; Walker, J. S.; Knox, K. J.; Miles, R. E. H.; Reid, J. P.; Signorell, R. Timescales of water transport in viscous aerosol: measurements on sub-micron particles and dependence on conditioning history. *Phys. Chem. Chem. Phys.* **2014**, *16*, 9819–9830.

[61] Mie Resonance Fitting (MRFIT). http://www.meteo.mcgill.ca/~tpreston/code.html.

[62] Gouesbet, G.; Grehan, G.; Maheu, B. Localized interpretation to compute all the coefficients g m n in the generalized Lorenz-Mie theory. *J. Opt. Soc. Am. A* **1990**, *7*, 998–1007.

[63] Lock, J. A.; Gouesbet, G. Generalized Lorenz–Mie theory and applications. *J. Quant. Spectrosc. Radiat. Transfer* **2009**, *110*, 800–807.

[64] Gouesbet, G.; Lock, J. A.; Gréhan, G. Generalized Lorenz–Mie theories and description of electromagnetic arbitrary shaped beams: Localized approximations and localized beam models, a review. *J. Quant. Spectrosc. Radiat. Transfer* **2011**, *112*, 1–27.

[65] Lock, J. A. Improved Gaussian beam-scattering algorithm. *Appl. Opt.* **1995**, *34*, 559–570.

[66] González-Cardel, M.; Arguijo, P.; Díaz-Uribe, R. Gaussian beam radius measurement with a knife-edge: a polynomial approximation to the inverse error function. *Appl. Opt.* **2013**, *52*, 3849–3855.

[67] Walker, J.; Wills, J.; Reid, J. Direct comparison of the thermodynamic properties of sodium chloride and ammonium sulphate aerosol at relative humidities approaching saturation. *J. Phys. Chem. A* **2010**, *114*, 12691–12691.

[68] Dennis-Smither, B. J.; Hanford, K. L.; Kwamena, N. O. A.; Miles, R. E.; Reid, J. P. Phase, morphology,

and hygroscopicity of mixed oleic acid/sodium chloride/water aerosol particles before and after ozonolysis. *J. Phys. Chem. A* **2012**, *116*, 6159–6168.

[69] Cai, C.; Stewart, D. J.; Preston, T. C.; Walker, J. S.; Zhang, Y. H.; Reid, J. P. A new approach to determine vapour pressures and hygroscopicities of aqueous aerosols containing semi-volatile organic compounds. *Phys. Chem. Chem. Phys.* **2014**, *16*, 3162–3172.

[70] Zuend, A.; Marcolli, C.; Luo, B. P.; Peter, T. A thermodynamic model of mixed organic-inorganic aerosols to predict activity coefficients. *Atmos. Chem. Phys.* **2008**, *8*, 4559–4593.

[71] Lide, D. R. *CRC Handbook of Chemistry and Physics*, 82nd ed.; CRC Press, 2002.

[72] Gao, D.; Guo, Y.; Yu, X.; Wang, S.; Deng, T. Solubilities, densities, and refractive indices in the salt-water ternary system (LiCl + $LiBO_2$+ H_2O) at T= 288.15 K and 298.15 K and $p = 0.1$ MPa. *J. Chem. Eng. Data* **2015**, *60*, 2594–2599.

Chapter 3

Mie scattering from strongly absorbing airborne particles in a photophoretic trap

Chapter Preface

In the previous chapter it was shown that fitting the morphology dependant resonances in the cavity-enhanced Raman spectrum resulted in the most accurate retrieval of the radius and refractive index for optically trapped particles. Here, the broadband Mie scattering spectrum is used to collect morphology dependant resonances over a broader wavelength range than accessible with cavity-enhanced Raman spectroscopy. The aim of this chapter is to build a model for the refractive index of aerosol having discrete absorption bands in the scattering spectrum.

3.1 Abstract

High-precision light scattering measurements of single, absorbing aerosol particles pose a challenge as the strong attenuation of light results in featureless spectra. Using the Kramers-Kronig relations and broadband light scattering, we develop and implement a method for the retrieval of both the size and complex refractive index of particles that are strongly absorbing across large spectral regions. This method is validated using both synthetic spectra and scattered light intensity measurements from single dye-doped polystyrene beads of known radii that are held using a photophoretic trap.

3.2 Introduction

Optical trapping has found use in the characterization of aerosol particles since measurements are free from substrate interactions and the effects of ensemble averaging.[1–4] Single particle measurements have found enormous success in high-precision studies of weakly absorbing aerosols.[1,3,5–11] However, many airborne particles of atmospheric interest cannot be considered weakly absorbing across optical wavelengths. Two well-known examples are black carbon, for which the imaginary part of the refractive index, k, is approximately 0.79 and is wavelength independent over the visible spectrum, and brown carbon, for which k is known to increase towards shorter visible and ultraviolet wavelengths.[12] Translating the success seen in studies of weakly absorbing particles to systems where absorption is non-negligible is a challenge in terms of both trapping and spectroscopic characterization. The trapping of

a single, weakly absorbing, airborne particle can be achieved with standard optical tweezers.[3,5,11,13–16] There are two main forces that are important to the trapping of an airborne particle; the scattering force and the gradient force.[13,17,18] The scattering force acts in the direction of propagation of the trapping beam and pushes the particle in the same direction. With only one beam, this is a destabilizing force that must be counteracted. The gradient force pulls a particle of higher refractive index than its surrounding medium towards the most intense part of the beam.[13,18] Gradient forces strong enough to overcome the scattering force can be achieved with high numerical aperture lenses.[13,17–19]

Conventional optical tweezers based on gradient forces are poorly suited for studies of strongly absorbing particles due to photophoretic forces caused by electromagnetic heating.[20–22] Photophoretic forces can be orders of magnitude greater than gradient forces for strongly absorbing particles and will push the particle away from the most intense region of the trapping beam.[19,22,23] However, this force can be exploited in order to trap absorbing particles. Early work utilized the photophoretic force to levitate micron-sized particles in a local intensity minimum.[24] More recently, the trapping of strongly absorbing particles in air has been achieved utilizing the photophoretic force by creating a so-called optical bottle, where the particle is held in a dark void that is completely surrounded by a region of high light intensity.[17,19,25–29]

Holding a weakly or strongly absorbing particle in an optical trap is not by itself useful for studying fundamental aerosol processes. It is the utilization of elastic and inelastic light scattering from the trapped particle that enables the high-precision work that was referenced earlier. In particular, the presence of sharp peaks in the scattering spectra of

individual spherical particles, which are sensitive to size and composition, have been utilized extensively.[1,3–7,9–11,14,15,30–36] These peaks are associated with optical modes that are often referred to as whispering gallery modes, morphology-dependent resonances or Mie resonances. The latter term strictly refers only to resonances in homogeneous, spherical particles. Most methods for determining particle size and composition are based on the assumption that k is close to zero. Indeed, this is an excellent assumption as measurements of k for weakly absorbing particles have yielded values on the order of 10^{-8} or 10^{-9} .[1,5] However, for particles that are strong absorbers the imaginary part of the refractive index cannot be neglected and it can be anticipated that sharp peaks associated with resonant scattering will be attenuated for these large values of k.[33,37] Quantifying absorption for strongly absorbing particles has been demonstrated for samples in solution[33,38,39] and for particle suspensions in air[40] by fitting the Ångström equation and by a Mie inversion procedure of IR spectra for particle streams[41,42] but to our knowledge has not been achieved at the single particle level.

Single particle broadband light scattering has become a heavily utilized tool in the aerosol optical trapping community in recent years. The scattering efficiency of white light from polymer spheres has been reported,[2] and more recently, Mie resonances in broadband scattering have been utilized to determine the size and real part of the refractive index of optically trapped particles.[3,4,9,10,34] Both Mie resonance positions[3,5–7,9,30–32,35] and full spectrum[4,33,43] fitting approaches have been employed to fit wavelength dependent Mie resonances. Linewidths in spectra of low size parameter systems tend to be quite broad (e.g. the optical spectrum of a particle whose size is only a few microns). Fitting spectra using only the peak positions of broad features can lead to inaccurate best-fits since the wavelengths of

maximum intensity are no longer approximately equal to Mie resonances.[3,33]

The absence of distinct features in light scattering spectra of strongly absorbing particles means that the spectroscopic determination of particle size and refractive index is a great challenge. In this report we develop a fitting scheme based on light scattering measurements across regions of strong and weak absorption. Utilizing the Kramers-Kronig relationships and an appropriate model for the complex refractive index (a set of Lorentzian oscillators), we are able to retrieve a particle's size and its wavelength-dependent complex refractive index from broadband scattering measurements. The accuracy of this retrieval scheme is first assessed using a synthetic data set. It is then applied to light scattering measurements from single, micron-sized, dye-doped polystyrene beads that strongly absorb light across a broad region of the visible spectrum. Single particle spectra for these beads are collected as they are held in a photophoretic trap. The accuracy of the resulting parameters of best-fits for these beads are assessed through a comparison to size measurements taken with a Coulter counter and measurements of ensemble spectra.

3.3 Experimental

Fig. 3.1 shows a schematic of the hollow beam optical trap used in the experiments here. Light from a $\lambda = 532$ nm laser (Opus 532, Laser Quantum) was passed through a half-wave plate to orient the polarization angle of the beam such that when it subsequently passed through a polarizing beamsplitting cube, it was split into two beams of equal intensity that were orthogonally polarized. The beam was expanded and 'cleaned up' as it passed through

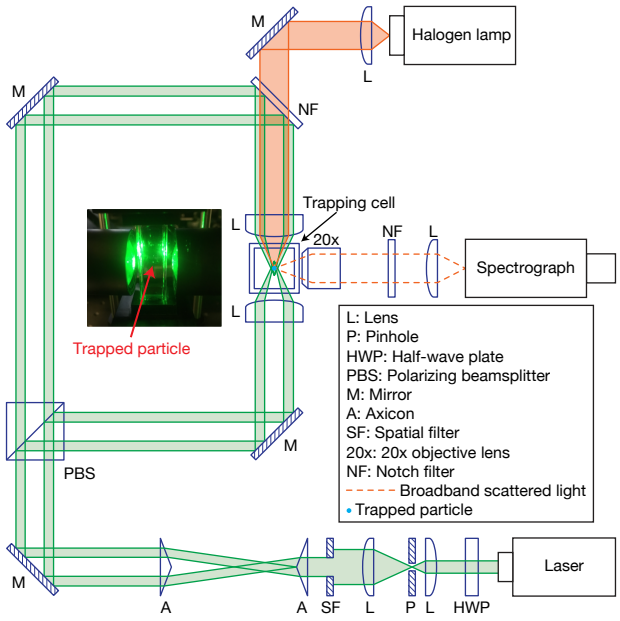

Figure 3.1: Schematic of the hollow beam optical trap and white light scattering setup. Inset: Photograph of the cell containing a trapped particle. The lenses surrounding the cell can also be seen in the photograph.

a 4× telescope with a pinhole at the focal point of the first lens. A spatial filter allowed for control of the diameter of the expanded, collimated beam. The beam was then passed through two 2° axicons (Thorlabs) spaced about 50 cm apart yielding a hollow beam with an outer diameter slightly smaller than 2.5 cm and an inner diameter that could be changed by opening or closing the previously mentioned spatial filter. The hollow beam was passed through the polarizing beamsplitter and directed with mirrors towards the trapping cell. Two 50 mm focal length achromatic aspheric lenses (Edmond Optics) focused the hollow beams into the trapping cell. The lenses were positioned so that their focal points did not overlapping in space, i.e. the lenses were slightly less than 100 mm apart. This resulted in a so-called optical bottle: a dark void, where the particle is trapped, that is surrounded by a volume of high intensity.

White light from a halogen lamp (OSL2 Thorlabs) was collimated and directed to the optical trap. A $\lambda = 532$ nm notch laser dichroic beamspiltter (NFD01-532 Semrock) reflected the laser light but transmitted the white light except in a narrow region centered at $\lambda = 532$ nm. The white light was then focused into the trapping cell, through one of the lenses used to create the optical trap, where it could interact with the particle. The variable power of the lamp was always turned up to full for these experiments.

Scattered light was collected with a 20× long working distance objective (PSM-PLAPO20X, Motic) with a numerical aperture (NA) of 0.42 oriented at 90° to the two trapping beams. The collimated light leaving the objective was passed through a notch filter (NF533-17 Thorlabs) to remove the elastic scattering from the laser beam and was then coupled into a spectrograph (Isoplane SCT-320, Princeton Instruments) with a 300 groove/mm diffraction grating where it was imaged on a CCD (PIXIS:100B_eXcelon, Princeton Instruments).

The particles used here were solid blue-dyed polystyrene beads (Polysciences, Inc) suspended in water. Two different aqueous suspensions were used: one containing beads with diameters of 3.15 ± 0.06 μm and one containing beads with diameters of 5.88 ± 0.25 μm. For brevity we will refer to these beads as 'small' particles and 'large' particles, respectively. The particles were introduced into the cell with a nebulizer (PARI TurboBOY SX). Typical trapping powers were between 50-300 mW depending on the size of the particle. Once trapped, any residual water on the surface of the particle would evaporate quickly due to the dry conditions in the trapping cell.

For each particle, four different spectra were acquired. Each spectrum was the result of 10 averaged one second frames. The acquisition proceeded as follows: First, a spectrum,

$I_F(\lambda)$, with the particle trapped but without the white light turned on was taken. This spectrum is a measurement of the laser induced fluorescence. Second, a spectrum, $I_{WL}(\lambda)$, of the white light scattering while the particle was trapped was collected. Third, the particle was knocked out of the trap and a spectrum, $I_B(\lambda)$, of the white light scattering was again taken. Finally, with no particle in the cell, the white light was turned off and a spectrum, $I_D(\lambda)$, of the dark background was collected.

With these four spectra and the intensity profile of the light source, $I_P(\lambda)$, the experimental spectrum of a single particle, $I_E(\lambda)$, was calculated using the following relationship:

$$I_E(\lambda) = \frac{I_{WL}(\lambda) - I_B(\lambda) - I_F(\lambda) + I_D(\lambda)}{I_P(\lambda)}. \tag{3.1}$$

At first glance it may seem odd that $I_D(\lambda)$ is added rather than subtracted from $I_{WL}(\lambda)$ in Eq. 3.1. However, both $I_F(\lambda)$ and $I_B(\lambda)$ will contain the dark spectrum in their signal so the addition of $I_D(\lambda)$ ensures that $I_D(\lambda)$ is only subtracted once from $I_{WL}(\lambda)$.

3.4 Theory

3.4.1 Model of the complex refractive index

The wavenumber-dependent complex refractive index is $m(\nu) = n(\nu) + ik(\nu)$, where $\nu = 1/\lambda$ and λ is the wavelength of light. The real part, n, and the imaginary part, k, of m are linked

through the Kramers-Kronig relationships (Ref. 44, p. 28):

$$n(\nu) = 1 + \frac{2}{\pi}\mathcal{P}\int_0^\infty \frac{\nu' k(\nu')}{\nu'^2 - \nu^2} d\nu', \tag{3.2}$$

$$k(\nu) = -\frac{2\nu}{\pi}\mathcal{P}\int_0^\infty \frac{n(\nu') + 1}{\nu'^2 - \nu^2} d\nu', \tag{3.3}$$

where $\mathcal{P}$ means that the Cauchy principal value of the integral is used.

One way to take advantage of Eqs. 3.2 and 3.3 is to use an expression for either n and k whose Kramers-Kronig transform has a known closed-form solution. To implement this methodology here, we will represent k using the sum of a set of Lorentzian functions.[45,46] In this model, the optical response of the medium can be thought of as originating from J oscillators. Each jth oscillator has a resonant wavenumber, $\nu_{0,j}$, a full-width at half-maximum (FWHM), Γ_j, and its contribution to k is

$$k_{L,j}(\nu) = \frac{B_j}{\pi}\left(\frac{\Gamma_j/2}{(\nu - \nu_{0,j})^2 + (\Gamma_j/2)^2} - \frac{\Gamma_j/2}{(\nu + \nu_{0,j})^2 + (\Gamma_j/2)^2}\right), \tag{3.4}$$

where B_j is a constant. Eq. 3.4 is an antisymmetric Lorentzian function. The expression for k that will be constructed using this type of function and the resulting expression for n will satisfy the symmetry conditions required by the Kramers-Kronig relations. Specifically, $k(-\nu) = -k(\nu)$ and $n(-\nu) = n(\nu)$.[46]

We will be performing optical measurements in the visible and near-infrared region of the spectrum. Optical transitions that occur at shorter wavelengths (in the ultraviolet and higher energies) will influence the refractive index in this region but their lineshapes and

resonant wavenumbers will not be known and cannot be found with our visible and near-infrared measurements. However, their contribution to the visible and near-infrared region can be expressed as[46]

$$k_\delta(\nu) = \lim_{\nu_\delta \to \infty} \frac{\pi}{2} B_\delta \nu_\delta \delta(\nu - \nu_\delta), \tag{3.5}$$

where B_δ is a constant that will offset the real part of the refractive index.

The imaginary part of the refractive index in this multiple-oscillator model will be

$$k(\nu) = \sum_{j=1}^{J} \frac{B_j}{\pi} \left(\frac{\Gamma_j/2}{(\nu - \nu_{0,j})^2 + (\Gamma_j/2)^2} - \frac{\Gamma_j/2}{(\nu + \nu_{0,j})^2 + (\Gamma_j/2)^2} \right) + k_\delta(\nu). \tag{3.6}$$

An expression for the real part of the refractive index can be found by inserting Eq. 3.6 into Eq. 3.2 and integrating to yield

$$n(\nu) = n_\infty + \frac{2}{\pi} \sum_{j=1}^{J} \frac{B_j \nu_{0,j} (\nu_{0,j}^2 - \nu^2 + (\Gamma_j/2)^2)}{(\nu_{0,j}^2 - \nu^2 + (\Gamma_j/2)^2)^2 + (\nu\Gamma_j)^2}, \tag{3.7}$$

where $n_\infty = 1 + B_\delta$.

3.4.2 Scattering spectrum and Mie resonances

The broadband white light source used in all experiments is unpolarized (the halogen lamp shown in Fig. 3.1). Therefore, the Stokes vector associated with the beam incident on a trapped particle is simply $\vec{S}_i = (I_i, 0, 0, 0)^{\mathrm{T}}$. The Stokes vector for the scattered wave is $\vec{S}_s = (I_s, Q_s, U_s, V_s)^{\mathrm{T}}$. However, as the spectrometer and CCD are not sensitive to the polarization of light, only the I_s component of $\vec{S}_s$ is needed when calculating the theoretical

scattered light spectrum. The spectrum is calculated by evaluating[47]

$$I_T(\lambda, a) = \int_0^{2\pi} \int_0^{\vartheta_{\max}} I_s(\vartheta_s, \varphi_s, \lambda, a)\, r^2 \sin\vartheta_s \, d\vartheta_s d\varphi_s \tag{3.8}$$

across the wavelength range of interest. In Eq. 3.8, a is the radius of the particle, r is the distance to the detector (simply set to one for all calculations presented here), and $\vartheta_{\max} = \arcsin(\mathrm{NA})$. The angles ϑ_s and φ_s are the polar and azimuthal scattering angles. The method for calculating $I_s(\vartheta_s, \varphi_s, \lambda, a)$ is discussed in Refs. 32,43,47. To calculate $I_T(\lambda, a)$, Eq. 3.8 is integrated numerically.

Electric and magnetic modes for a homogeneous spherical particle can be calculated using the Mie scattering coefficients. The characteristic equation for these Mie resonances is[7]

$$m\gamma \frac{j_n'(mz)}{j_n(mz)} = \frac{h_n^{(1)\prime}(z)}{h_n^{(1)}(z)} + \frac{1-\gamma}{z}, \tag{3.9}$$

where j_n and $h_n^{(1)}$ are spherical Bessel functions and Hankel functions of the first kind, respectively. The parameter γ is defined as $\gamma = 1$ for transverse electric (TE) modes and $\gamma = 1/m^2$ for transverse magnetic (TM) modes. A set of complex resonant size parameters, $z_{n,l,p} = x_{n,l,p} + iy_{n,l,p}$, where n is the mode number (not to be confused with the real part of the refractive index), l is the mode order, and p is a label that indicates the polarization of the resonance (TE or TM), satisfy Eq. 3.9. Modes will be labeled in the form p_n^l. The real part of $z_{n,l,p}$ is the resonant size parameter, $x_{n,l,p}$. The linewidth of a resonance is equal to $-2y_{n,l,p}$ and can therefore be calculated using the imaginary part of $z_{n,l,p}$.

Solutions to Eq. 3.9 can be found using a root-finding algorithm (e.g. the Newton-Raphson method is used here) with an initial guess that is close to the true value of $z_{n,l,p}$. The explicit approximate formula presented by Lam *et al.*[36] provides suitable values for the initial guesses of the resonant size parameter when the imaginary part of the refractive index is zero. For cases when $k > 0$, we found suitable initial guesses by first setting $k = 0$, then (i) solving Eq. 3.9, (ii) increasing the value of k by a small amount, (iii) solving Eq. 3.9 using the result from Step (i) as an initial guess, (iv) Repeating Steps (i–iii) until the desired value of k was reached. With this iterative approach, complex resonant size parameters for a range of k starting from $k = 0$ could be tabulated. The behavior of the complex resonant size parameter as the imaginary part of the refractive index changes is discussed in Section 3.5.1.

3.5 Discussion

3.5.1 The effect of the imaginary part of the refractive index on Mie spectra

Fig. 3.2 shows a set of simulated (a) extinction efficiency, (b) scattering efficiency, and (c) scattered intensity spectra for a spherical particle with a radius of 3000 nm where the real part, n, of the refractive index is held constant while the imaginary part, k, is varied. As k increases, the intensity of sharp, first-order peaks quickly falls off. The intensity of the second order peaks also decreases, but the onset of significant change occurs at higher k.

For instance, the intensity of the second order peaks in the $k = 10^{-4}$ plots is very similar to the plots with smaller values of k but the first order peaks are completely absent from all of the $k = 10^{-4}$ plots. For the largest values of k shown in Fig. 3.2, all of the spectra are fairly featureless (with the one exception being the four broad peaks in Fig. 3.2c that correspond to second order TM modes).

The relationship between the imaginary part of the refractive index, Mie resonance positions, and linewidths is explored more thoroughly in Fig. 3.3 by plotting resonance (a) positions and (b) linewidths as a function of k. In Fig. 3.3a, it is clear that until $k > 0.01$, the effect of the imaginary part of the refractive on Mie resonance positions is small. For $k < 0.01$, the resonance positions of all three mode orders are approximately independent of k. In contrast, in Fig. 3.3b it can be seen that, even for the smallest values of k that are plotted, the linewidths of first order modes are already sensitive to changes in k and increase significantly with increasing k. The linewidths of the second and third order modes remain unchanged for the smallest values of k shown in Fig. 3.3b. However, if compared to when k begins to affect the Mie resonances in Fig. 3.3a, the onset of a dependence on k for the linewidths occurs at much lower values in Fig. 3.3b. It is also interesting to note that the onset of shifts in resonance positions with increasing k occur at lower k for higher mode orders while the opposite trend is seen with changes in linewidths (the onset of shifts occur at lower k for lower mode orders). Overall, from Fig. 3.3 it is apparent that linewidths are much more sensitive to k than resonance positions. The implication for sizing particles is that if peaks are sharp enough to be observed in a broadband scattering spectrum, it should be a satisfactory approximation to set k equal to zero when using the set of observed peak

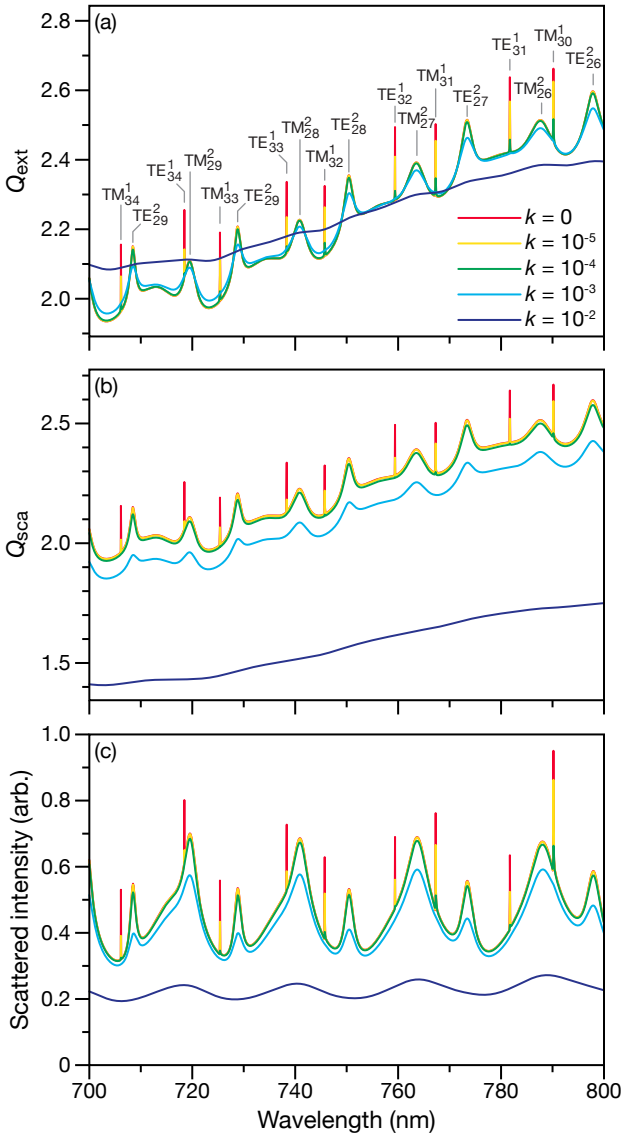

Figure 3.2: Calculated (a) extinction efficiency, Q_{ext}, (b) scattering efficiency, Q_{sca}, and (c) scattered intensity spectra for a spherical particle with a radius of 3000 nm and a complex refractive index of $m = n + ik$, where $n = 1.5$ and the values of k are listed in (a). For the scattered intensity calculation, the numerical aperture of the collection objective was 0.42 and the axis of the objective was orthogonal to the unpolarized incident beam. Peaks in (a) are labeled with their mode assignments that were found using Eq. 3.9.

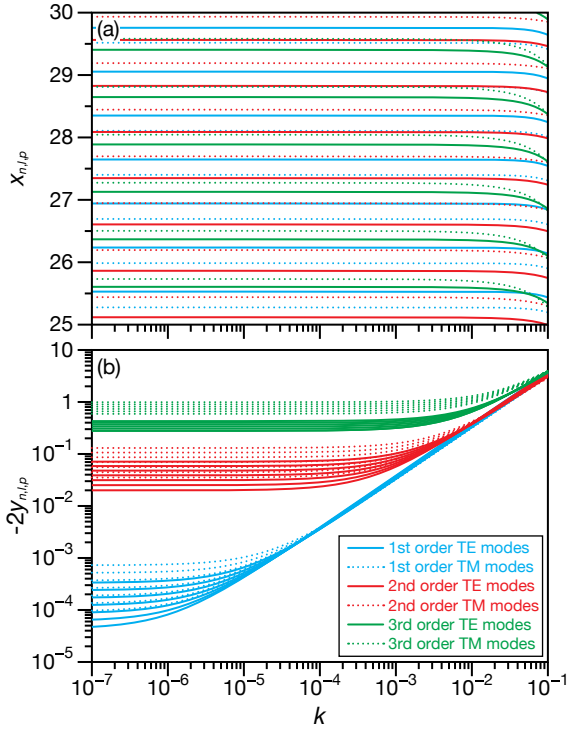

Figure 3.3: Mie resonance (a) positions, $x_{n,l,p}$, and (b) linewidths, $-2y_{n,l,p}$, as a function of the imaginary part of the refractive index, k, for a sphere with a real part of the refractive index set to 1.5. The complex resonant size parameters, $z_{n,l,p} = x_{n,l,p} + iy_{n,l,p}$, were calculated using Eq. 3.9. Calculations for mode orders, l, between 1 and 3 and mode numbers, n, whose value of $x_{n,l,p}$ is between 25 and 30 are shown. Both polarizations, p, are shown (TE and TM).

positions to retrieve particle size. Additionally, it should also be possible to fit the peaks and determine the real part of the refractive index across the region of the spectrum where sharp peaks are observed. This type of resonance fitting will be discussed below.

To accurately model the optical constants of an actual material it is necessary to include the variation of both n and k with wavelength due to dispersion. Consequently, classifying materials as either weakly or strongly absorbing is not useful unless a specific wavelength range is specified. Fig. 3.4a shows a synthetic refractive index function for a material whose

refractive index is modeled using Eqs. 3.6 and 3.7. This material is strongly absorbing in the region near $\lambda = 600$ nm (e.g. k at $\lambda = 600$ nm is 4.57×10^{-2}) but outside of this region, at either shorter or longer wavelengths, absorption decreases significantly (e.g. k at $\lambda = 450$ nm is 6.92×10^{-4} and k at $\lambda = 750$ nm is 1.89×10^{-3}). Fig. 3.4b shows the corresponding broadband scattering spectrum calculated using this refractive index function for a sphere with a radius of 3000 nm. Near $\lambda = 600$ nm, the scattered light intensity shows only a broad minimum and is otherwise featureless. As one moves away from this region, either towards shorter or longer wavelengths, peaks associated with Mie resonances become visible.

One problem we wish to address in this work is the retrieval of the size and complex refractive index of aerosol particles that strongly absorb light across regions of the visible spectrum. A brute-force solution would be to minimize the error (or maximize the correlation) between simulated and measured broadband scattering spectra by varying the particle size and the parameters that describe the refractive index function in the simulation. In principle this approach is feasible, but it has the potential to be very computationally intensive. Even in the simplest case, where the complex refractive index of the particle can be accurately modeled with a single oscillator, it would still be necessary to search a space with five parameters during the fitting process: particle size, the three parameters that characterize the oscillator, and n_∞. Each additional oscillator that is needed to accurately model the complex refractive index will mean that three more dimensions are added to the search space.

To implement a search through the parameter space in a computationally efficient manner

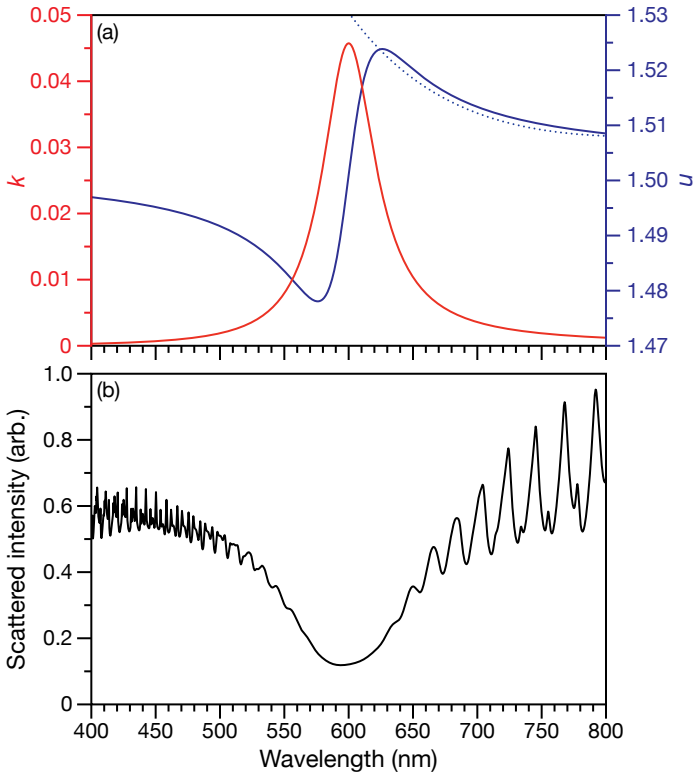

Figure 3.4: (a) The real part, n, and imaginary part, k, of a synthetic complex refractive function and (b) the corresponding broadband scattering spectrum. The synthetic complex refractive index was calculated using Eqs. 3.6 and 3.7 with $J = 1$ (a single oscillator), a resonant wavelength of 600 nm ($\nu_{0,1} = 1/600$ nm^{-1}), FWHM of 50 nm ($\Gamma_1 = 1.19 \times 10^{-4}$ nm^{-1}), $B_1 = 10^{-5}$ nm^{-1}, and $n_\infty = 1.5$. For the scattered intensity calculation, the radius of the sphere was 3000 nm, the numerical aperture of the collection objective was 0.42 and the axis of the objective was orthogonal to the unpolarized incident beam. The dotted line in panel (a) is the n of best-fit found using MRFIT by fitting peaks between $\lambda = 745$ and 800 nm in panel (b).

we take the following approach: First, we fit the Mie resonances in a weakly absorbing region of the spectrum using the freely available program, MRFIT.[7,48] This enables us to accurately size the particle. For the synthetic spectrum in Fig. 3.4b we take the peaks at $\lambda = 745.286$, 755.108, 767.848, 777.748, and 792.025 nm and fit them using MRFIT. This results in a radius of best-fit of 3001.7 nm. Additionally, the real part of the refractive index retrieved using the resonance fitting is accurate within the region of the spectrum where the Mie resonance peaks are found ($n_{\text{best-fit}} = 1.5369 - 39174/\lambda^2 + 1.3265 \times 10^{10}/\lambda^4$, where λ is in nm). For comparison, this refractive index of best-fit is plotted as a dotted line in Fig. 3.4a. The refractive index from MRFIT can also be used to provide an initial guess for n_∞. Next, we note that while the minimum in scattered intensity at $\lambda = 594$ nm does not exactly match the actual resonant wavelength of 600 nm, it is close and should be an excellent first guess. Finally, the width of the minimum in scattered intensity can be used as a first guess for the FWHM of the oscillator.

With these pieces of information, the search space will be greatly constrained and accurate parameters of best-fits can be found much more quickly than would be possible without suitable initial guesses or bounds. Of course, the above analysis relied on the knowledge that the refractive index function could be suitably described using only one oscillator. In the following section we will consider the fitting of measurements where such an assumption will not be valid. However, as will be shown, the methodology discussed here can readily be extended to cases where multiple oscillators are required to fit observed spectra.

3.5.2 Measured scattering spectra of absorbing particles

Fig. 3.5a shows the single particle spectra of two different dye-doped polystyrene beads held in a photophoretic trap. Each bead was trapped from an aerosol plume containing particles with a supplier determined size distribution measured by a Coulter counter of either 1575 ± 30 nm (for brevity, referred to as 'small') or 2940 ± 125 nm (for brevity, referred to as 'large'). The scattered intensity in Fig. 3.5 was found using Eq. 3.1 and the appropriate spectral measurements discussed in Section 3.3. The low intensity scattering region of the spectrum ($580 - 670$ nm) corresponds to absorption in the orange region of the spectrum, which is reasonable since the beads appear blue to the naked eye. There is a region in the middle of both spectra ($670 - 720$ nm) where the scattered light intensity increases but sharp resonances are not visible. The absorbance here is not as strong as it is at shorter wavelengths but it is still substantial enough to remove any sharp resonances. Features observed at longer wavelengths ($720 - 800$ nm) look like the Mie resonances seen in the scattering spectra of weakly absorbing spheres.[3,4,9,10,34] Sharp resonances can be observed in the spectrum of the large particle while the peaks in the spectrum of small particle are broader. Above 800 nm there was significant noise in measured spectra due to the low intensity of the light source at those wavelengths. Therefore, we have excluded that region of the spectrum from our results.

Fig. 3.5b shows ensemble measurements of the small and large particles. The particles were dispersed in water and the measurements were taken by replacing the trapping cell with a cuvette of this dispersion. The sharp resonances that appeared in the scattering

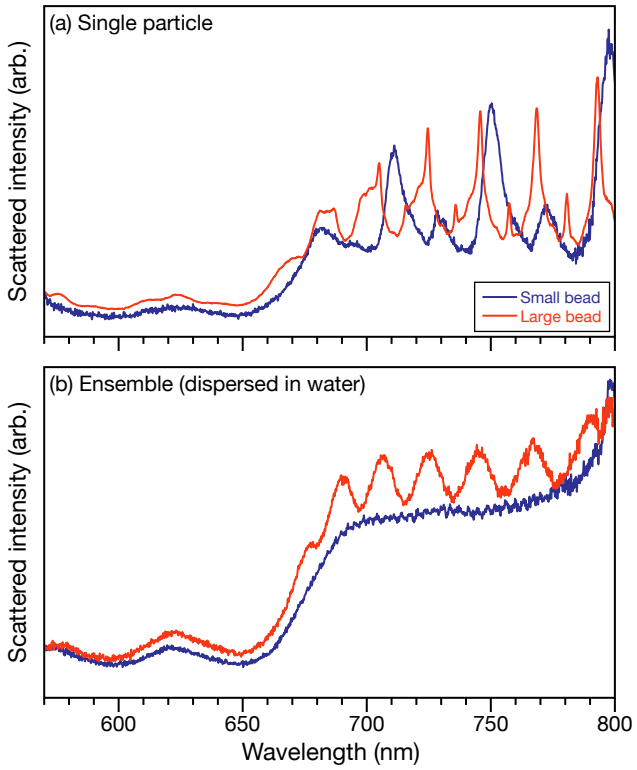

Figure 3.5: Broadband scattering spectra of small and large dye-doped polystyrene beads. In (a) the scattering of a single particle held in the hollow beam optical trap is measured. In (b) the scattering of an ensemble measurement of particles dispersed in water is measured.

spectra of individual particles (Fig. 3.5a) are absent in both cases but similar scattering minima below 700 nm are still observed. The scattering intensity from the small spheres is featureless and nearly flat across the weakly absorbing region of the spectrum. The sharp increase in scattering intensity at the longest wavelengths is an artifact of background removal. The absence of Mie resonance peaks when moving from the single particle spectrum to the ensemble spectrum of the small particles is due to a combination of the distribution of particle sizes present in the ensemble scattering measurement and the fact that those particles are in a higher index medium (water rather than air). These same effects eliminate the very sharp peaks that are seen in the single particle spectrum of the large particles. In the ensemble measurement of the large particles, only very broad peaks are observed.

3.5.3 Retrieval of size and complex refractive index from single particle spectra

Using the fitting methodology outlined in Section 3.5.1, we first use MRFIT to determine the initial guesses for the radius using the peak positions located in the region between $700 - 800$ nm. This also gives values for n in that region of the spectrum. Again we emphasize that MRFIT is strictly only valid for materials where $k = 0$, however, the results shown in Fig. 3.2 and 3.3 show that the assumption of $k = 0$ should still yield accurate results provided that $k < 0.01$. We sized 25 large particles and determined using MRFIT the mean radius of best-fit was 2892 ± 41 nm and n at $\lambda = 800$ nm was 1.575 ± 0.005. For the small particles, the mean radius of best-fit for 26 particles was found to be 1448 ± 86 nm

and n at $\lambda = 800$ nm was 1.538 ± 0.057.

In Fig. 3.5a, two broad minima in the scattered light intensity are observed in both the spectra of the large and small particle near $\lambda = 593$ and 650 nm. These minima are more distinct in the small particle spectrum since the large particle spectrum has some weak features between the minima that result in other local minima. Based on these two observed minima in the scattered intensity, we modeled the refractive index with two oscillators ($J = 2$ in Eqs. 3.6 and 3.7). The resonant wavelengths of the two oscillators were simply set very close to the observed locations of the intensity minima.

The complex refractive indices of best-fit for the small and large particles were found by maximizing the correlation between measured and calculated broadband scattering spectra. As stated earlier, 26 spectra of different, single small particles were collected and 25 spectra of different, single large particles were collected. When fitting one particle size, correlation was simultaneous maximized across either set of spectra. The parameters of best-fit for the refractive index were found by varying the parameters B_1, B_2, Γ_1, Γ_2, and n_∞. It was assumed that these parameters would be identical for particles within either the small or large set. However, the radius would not be constant for particles within a set, so this was allowed to vary as the sum of the correlations across all spectra in a set was maximized. The refractive indices of best-fit are plotted in Fig. 3.6 and the parameters of best-fit are listed in the caption.

The differences between the n and k for the two particle sizes seen in Fig. 3.6 can be attributed to the amount of dye in the beads. Based on the specifications of the supplier, beads can contain $10 - 40\%$ dye by mass. The parameters for the small beads (larger values

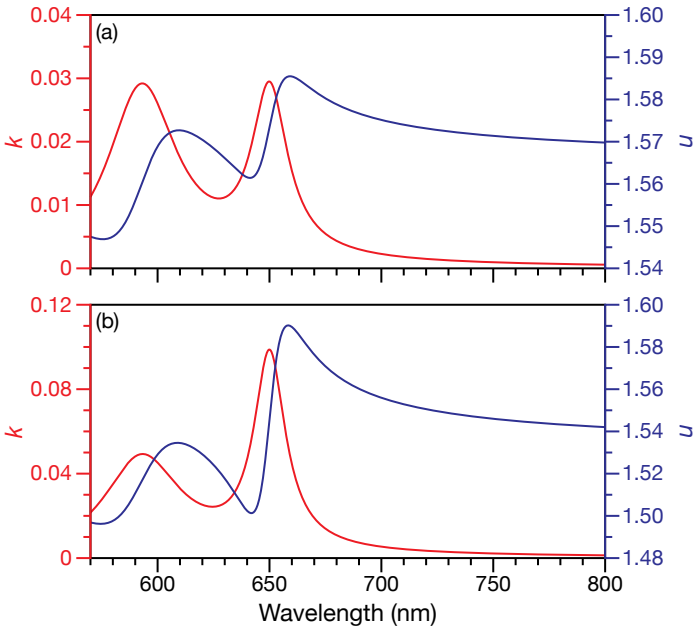

Figure 3.6: The real part, n, and imaginary part, k, of the complex refractive index of best-fit for the (a) large and (b) small dye-doped polystyrene beads. The complex refractive index was modeled using Eqs. 3.6 and 3.7 with two oscillators ($J = 2$). The parameters of best-fit for the large beads were $\nu_{0,1} = 1/650$ nm^{-1}, $\Gamma_1 = 4.57 \times 10^{-5}$ nm^{-1}, $B_1 = 1.88 \times 10^{-6}$ nm^{-1}, $\nu_{0,2} = 1/593$ nm^{-1}, $\Gamma_2 = 1.08 \times 10^{-4}$ nm^{-1}, $B_2 = 4.83 \times 10^{-6}$ nm^{-1}, and $n_\infty = 1.564$. The parameters of best-fit for the small beads were $\nu_{0,1} = 1/650$ nm^{-1}, $\Gamma_1 = 4.02 \times 10^{-5}$ nm^{-1}, $B_1 = 5.82 \times 10^{-6}$ nm^{-1}, $\nu_{0,2} = 1/593$ nm^{-1}, $\Gamma_2 = 1.20 \times 10^{-4}$ nm^{-1}, $B_2 = 8.95 \times 10^{-6}$ nm^{-1}, and $n_\infty = 1.528$.

of B_1 and B_2) would indicate that they contain a higher percentage of dye by mass than the large beads. Additionally, the value of n at $\lambda = 800$ nm was 1.542 for the small beads and 1.570 for the large beads. For pure polystyrene, the value of n at $\lambda = 800$ nm is 1.578.[49] Therefore, in a region of the spectrum far away from the absorption band of the dye, the real part of the refractive index of the large beads is closer to that of pure polystyrene. The result of this comparison suggests that the mass fraction of polystyrene is higher in the large beads (and, consequently, that its mass fraction of the dye is lower). This is consistent with the composition implied by the values of B_1 and B_2 that were obtained during the fitting process.

Examples of scattering spectra of best-fit are shown in Figs. 3.7 and 3.8. It can be seen that the spectra calculated with the two fitted refractive index functions yield good agreement with the measured spectra. In the short wavelength region of the spectra, the scattering minima are located in the same position for all measurements. In all cases, there is also a rise in scattered light intensity between these minima. There are also small bumps around these minima in both the experimental and simulated spectra that arise due to the decrease in k between the two minima. In the mid-wavelength range we see a sharp increase in scattered light intensity for both calculated and measured spectra. Finally, in the long wavelength range where the particles are weakly absorbing, we see good agreement between calculated and measured peak positions.

The retrieved radii by Mie resonance fitting were much smaller than the expected values given by the manufacturer. We measured the particle radii by optical microscopy to confirm the radii. Table 3.1 lists the radii determined by (i) the supplier using a Coulter counter,

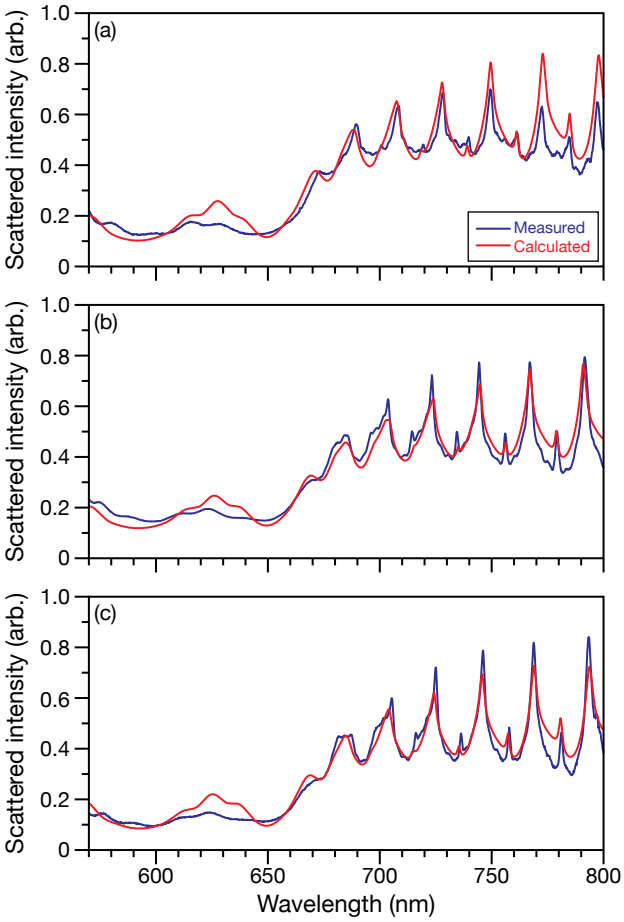

Figure 3.7: Three examples of measured and calculated broadband scattering spectra for single, large dye-doped polystyrene beads. The radii of best-fit were (a) 2829 nm, (b) 2896 nm, and (c) 2814 nm. The complex refractive index used in all three calculations is shown in Fig. 3.6a.

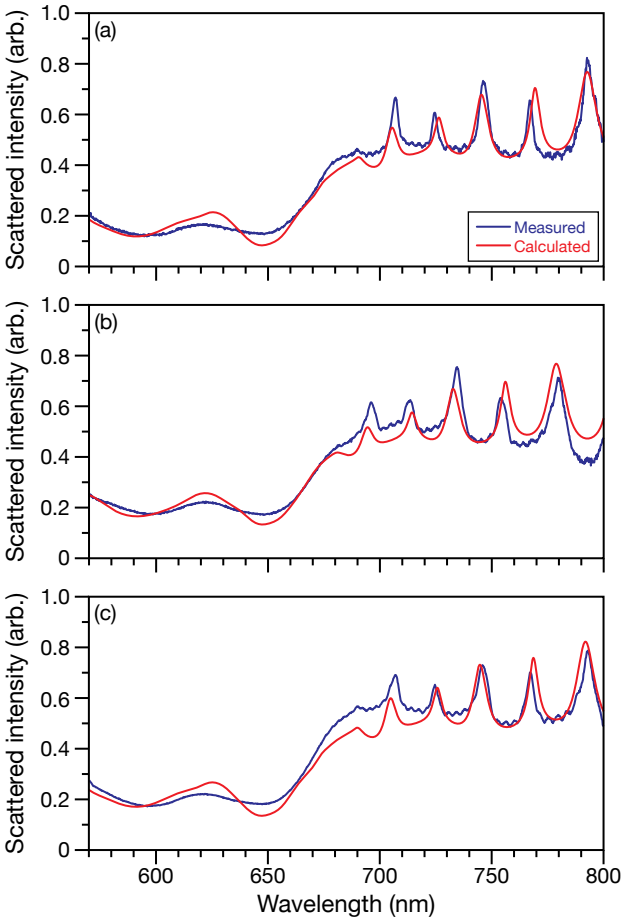

Figure 3.8: Three examples of measured and calculated broadband scattering spectra for single, small dye-doped polystyrene beads. The radii of best-fit were (a) 1412 nm, (b) 1387 nm, and (c) 1411 nm. The complex refractive index used in all three calculations is shown in Fig. 3.6b.

Table 3.1: Radii and standard deviations for large and small beads measured using a Coulter counter, optical microscopy, and fitting broadband scattering spectra.

Sizing method	Radius (nm)	
	Large beads	Small beads
Coulter counter	2949 ± 125	1575 ± 30
Optical microscopy	2737 ± 206	1443 ± 111
Fitting broadband spectra	2830 ± 38	1415 ± 6

(ii) optical microscopy and (iii) applying the Mie fitting algorithm to measured broadband spectra. The mean radii determined from fitting the scattering spectra were 1415 ± 6 nm for the small particles (5.34 standard deviations lower than the mean radius measured with a Coulter counter and 0.25 standard deviations lower than the mean radius measured with optical microscopy) and 2830 ± 38 nm for the large particles (0.88 standard deviations lower than the mean radius measured with a Coulter counter and 0.45 standard deviations greater than the mean radius measured with optical microscopy). Therefore, radii determined by fitting the Mie scattering spectra are within one standard deviation of radii measured using optical microscopy for both the large and small particles. For particles in this size regime, optical microscopy is a very accurate sizing methodology and, based on the results in Table 3.1, we can conclude that fitting broadband spectra has a similar accuracy. However, by fitting an entire Mie scattering spectrum, we are also able to retrieve both n and k across both strongly and weakly absorbing regions of the spectrum. This also differentiates the fitting procedure from simply fitting Mie resonance positions as that only allows for n to be found in the weakly absorbing region.

3.6 Summary

For the first time, we have presented broadband scattering measurements from single, strongly absorbing aerosol particles. Measurements of single particle spectra were fitted in order to retrieve the particle size and wavelength-dependent complex refractive index. The fitting process used a refractive index model that satisfied the Kramers-Kronig relations and treated the optical response of the particle material as a sum of Lorentzian oscillators. Once the parameters of best-fit were retrieved, calculated spectra gave good agreement with single particle measurements. We also investigated the effect of a non-zero imaginary refractive index on Mie resonances and linewidths in detail. Linewidths were found to be much more sensitive to changes in the imaginary part of the refractive index than resonance positions. This result allows for the retrieval of accurate sizes and the real part of the refractive index (across spectral regions where Mie resonance peaks are observed) using common resonance fitting algorithms where the imaginary part of the refractive index is assumed to be zero (e.g. MRFIT was used here). Utilizing the information from resonance fitting, along with observed minima in the broadband scattered intensity, the search space defined by the Lorentzian oscillator parameters becomes greatly constrained and the retrieval of the size and complex refractive index of best-fit is much less computationally demanding. This methodology enables the characterization of the optical properties of single particles across an entire measured spectrum regardless if the material is weakly or strongly absorbing.

References

[1] Rafferty, A.; Preston, T. C. Measuring the size and complex refractive index of an aqueous aerosol particle using electromagnetic heating and cavity-enhanced Raman scattering. *Phys. Chem. Chem. Phys.* **2018**, *20*, 17038–17047.

[2] Li, P.; Shi, K.; Liu, Z. Manipulation and spectroscopy of a single particle by use of white-light optical tweezers. *Opt. Lett.* **2005**, *30*, 156–158.

[3] Lew, L. J. N.; Ting, M. V.; Preston, T. C. Determining the size and refractive index of homogeneous spherical aerosol particles using Mie resonance spectroscopy. *Appl. Opt.* **2018**, *57*, 4601–4609.

[4] David, G.; Esat, K.; Ritsch, I.; Signorell, R. Ultraviolet broadband light scattering for optically-trapped submicron-sized aerosol particles. *Phys. Chem. Chem. Phys.* **2016**, *18*, 5477–5485.

[5] Miles, R. E. H.; Walker, J. S.; Burnham, D. R.; Reid, J. P. Retrieval of the complex refractive index of aerosol droplets from optical tweezers measurements. *Phys. Chem. Chem. Phys.* **2012**, *14*, 3037–3047.

[6] Preston, T. C.; Reid, J. P. Accurate and efficient determination of the radius, refractive index, and dispersion of weakly absorbing spherical particle using whispering gallery modes. *J. Opt. Soc. Am. B* **2013**, *30*, 2113–2122.

[7] Preston, T. C.; Reid, J. P. Determining the size and refractive index of microspheres using the mode assignments from Mie resonances. *J. Opt. Soc. Am. A* **2015**, *32*, 2210–2217.

[8] Carruthers, A. E.; Reid, J. P. Longitudinal optical trapping and sizing of aerosol droplets. *Opt. Express* **2010**, *18*, 14238–14244.

[9] Jones, S. H.; King, M. D.; Ward, A. D. Determining the unique refractive index properties of solid polystyrene aerosol using broadband Mie scattering from optically trapped beads. *Phys. Chem. Chem. Phys.* **2013**, *15*, 20735–20741.

[10] Jones, S. H.; King, M. D.; Ward, A. D. Atmospherically relevant core-shell aerosol studied using optical trapping and Mie scattering. *Chem. Comm.* **2015**, *51*, 4914–4917.

[11] Guillon, M.; Miles, R. E.; Reid, J. P.; McGloin, D. Thermo-optical resonance locking of an optically trapped salt-water microdroplet. *New J. Phys.* **2009**, *11*, 103041.

[12] Moosmüller, H.; Chakrabarty, R. K.; Arnott, W. P. Aerosol light absorption and its measurement: A review. *J. Quant. Spectrosc. Radiat. Transf.* **2009**, *110*, 844–878.

[13] Omori, R.; Kobayashi, T.; Suzuki, A. Observation of a single-beam gradient-force optical trap for dielectric particles in air. *Opt. Lett.* **1997**, *22*, 816–818.

[14] Knox, K. J.; Reid, J. P. Ultrasensitive absorption spectroscopy of optically-trapped aerosol droplets. *J. Phys. Chem. A* **2008**, *112*, 10439–10441.

[15] Gorkowski, K.; Donahue, N. M.; Sullivan, R. C. Emerging investigator series: determination of biphasic core-shell droplet properties using aerosol optical tweezers. *Environ. Science: Process. Impacts* **2018**, *Advance Article*.

[16] Davies, J. F.; Wilson, K. R. Raman spectroscopy of isotopic water diffusion in ultraviscous, glassy, and gel states in aerosol by use of optical tweezers. *Anal. Chem.* **2016**, *88*, 2361–2366.

[17] Redding, B.; Pan, Y.-L. Optical trap for both transparent and absorbing particles in air using a single shaped laser beam. *Opt. Lett.* **2015**, *40*, 2798–2801.

[18] Zhao, C. Practical guide to the realization of a convertible optical trapping system. *Opt. Express* **2017**, *25*, 2496–2510.

[19] Pan, Y. L.; Wang, C.; Hill, S. C.; Coleman, M.; Beresnev, L. A.; Santarpia, J. L. Trapping of individual airborne absorbing particles using a counterflow nozzle and photophoretic trap for continuous sampling and analysis. *Appl. Phys. Lett.* **2014**, *104*, 113507.

[20] Shvedov, V. G.; Desyatnikov, A. S.; Rode, A. V.; Krolikowski, W. Z.; Kivshar, Y. S. Optical guiding of absorbing nanoclusters in air. *Opt. Express* **2009**, *17*, 5743–5757.

[21] Desyatnikov, A. S.; Shvedov, V. G.; Rode, A. V.; Krolikowski, W.; Kivshar, Y. S. Photophoretic manipulation of absorbing aerosol particles with vortex beams: theory versus experiment. *Opt. Express* **2009**, *17*, 8201–8211.

[22] Ashkin, A. Acceleration and trapping of particles by radiation pressure. *Phys. Rev. Lett.* **1970**, *24*, 156–159.

[23] Campos, W. H.; Fonseca, J. M.; Mendes, J. B. S.; Rocha, M. S.; Moura-Melo, W. A. How light absorption modifies the radiative force on a microparticle in optical tweezers. *Appl. Opt.* **2018**, *57*, 7216–7224.

[24] Lewittes, M.; Arnold, S.; Oster, G. Radiometric levitation of micron sized spheres. *Appl. Phys. Lett.* **1982**, *40*, 455–457.

[25] Redding, B.; Hill, S. C.; Alexson, D.; Wang, C.; Pan, Y.-L. Photophoretic trapping of airborne particles using ultraviolet illumination. *Opt. Express* **2015**, *23*, 3630–3639.

[26] Wang, C.; Pan, Y. L.; Hill, S. C.; Redding, B. Photophoretic trapping-Raman spectroscopy for single pollens and fungal spores trapped in air. *J. Quant. Spectrosc. Radiat. Transf.* **2015**, *153*, 4–12.

[27] Gong, Z.; Pan, Y.-L.; Wang, C. Optical configurations for photophoretic trap of single particles in air. *Rev. Sci. Instrum.* **2016**, *87*, 103014.

[28] Alpmann, C.; Esseling, M.; Rose, P.; Denz, C.; Alpmann, C.; Esseling, M.; Rose, P.; Denz, C. Holographic optical bottle beams. *Appl. Opt. Lett.* **2012**, *100*, 111101.

[29] Curtis, J. E.; Koss, B. A.; Grier, D. G. Dynamic holographic optical tweezers. *Opt. Commun.* **2002**, *207*, 169–175.

[30] Hill, S. C.; Rushforth, C. K.; Benner, R. E.; Conwell, P. R. Sizing dielectric spheres and cylinders by aligning measured and computed resonance locations: algorithm for multiple orders. *Appl. Opt.* **1985**, *24*, 2380–2390.

[31] Conwell, P. R.; Rushforth, C. K.; Benner, R. E.; Hill, S. C. Efficient automated algorithm for the sizing of dielectric microspheres using the resonance spectrum. *J. Opt. Soc. Am. A* **1984**, *1*, 1181–1187.

[32] Bain, A.; Rafferty, A.; Preston, T. C. Determining the size and refractive index of single aerosol particles using angular light scattering and Mie resonances. *J. Quant. Spectrosc. Radiat. Transf.* **2018**, *221*, 61–70.

[33] Shepherd, R. H.; King, M. D.; Marks, A.; Brough, N.; Ward, A. D. Determination of the refractive index of insoluble organic extracts from atmospheric aerosol over the visible wavelength range using optical tweezers. *Atmos. Chem. Phys.* **2018**, *18*, 5235–5252.

[34] Ward, A. D.; Zang, M.; Hunt, O. Broadband Mie scattering from optically levitated aerosol droplets using a white LED. *Chem. Comm.* **2006**, *16*, 4515–4517.

[35] Eversole, J. D.; Lin, H. B.; Huston, A. L.; Campillo, A. J.; Leung, P. T.; Liu, S. Y.; Young, K. High-precision identification of morphology-dependent resonances in optical processes in microdroplets. *J. Opt. Soc. Am. B* **1993**, *10*, 1955–1968.

[36] Lam, C. C.; Leung, P. T.; Young, K. Explicit asymptotic formulas for the positions, widths, and strengths of resonances in Mie scattering. *J. Opt. Soc. Am. B* **1992**, *9*, 1585–1592.

[37] Chylek, P.; Ngo, D.; Pinnick, R. G. Resonance Structure of Composite and Slightly Absorbing Spheres. *J. Opt. Soc. Am. A* **1992**, *9*, 775–780.

[38] Zhou, Y.; Wang, X.; Wu, Q.; Cong, Z.; Wu, G.; Ji, M. Quantifying light absorption of iron oxides and carbonaceous aerosol in seasonal snow across northern China. *Atmosphere* **2017**, *8*, 15–22.

[39] Moosmüller, H.; Chakrabarty, R. K.; Ehlers, K. M.; Arnott, W. P. Absorption Ångström coefficient, brown carbon, and aerosols: Basic concepts, bulk matter, and spherical particles. *Atmos. Chem. Phys.* **2011**, *11*, 1217–1225.

[40] Hoffer, A.; Gelencsér, A.; Guyon, P.; Kiss, G.; Schmid, O.; Frank, G. P.; Artaxo, P.; Andreae, M. O. Optical properties of humic-like substances (HULIS) in biomass-burning aerosols. *Atmos. Chem.Phys.* **2006**, *6*, 3563–3570.

[41] Dohm, M. T.; Potscavage, A. M.; Niedziela, R. F. Infrared optical constants for carvone from the Mie inversion of aerosol extinction spectra. *J. Phys. Chem. A* **2004**, *108*, 5365–5376.

[42] Tang, M.; Alexander, J. M.; Kwon, D.; Estillore, A. D.; Laskina, O.; Young, M. A.; Kleiber, P. D.; Grassian, V. H. Optical and physicochemical properties of brown carbon aerosol: Light scattering, FTIR extinction spectroscopy, and hygroscopic growth. *J. Phys. Chem. A* **2016**, *120*, 4155–4166.

[43] Schmitz, M.; Rothe, T.; Kienle, A. Evaluation of a spectrally resolved scattering microscope. *Biomed. Opt. Express* **2011**, *2*, 2665–2678.

[44] Bohren, C. F.; Huffman, D. R. *Absorption and Scattering of Light by Small Particles*; Wiley-VCH, 1983; p 28.

[45] Hawranek, J. P.; Neelakantan, P.; Young, R. P.; Jones, R. N. The control of errors in I.R. spectrophotometry—IV. Corrections for dispersion distortion and the evaluation of both optical constants. *Spectrochim. Acta Part A Mol. Spectrosc.* **1976**, *32*, 85–98.

[46] Gienger, J.; Groß, H.; Neukammer, J.; Bär, M. Determining the refractive index of human hemoglobin solutions by Kramers–Kronig relations with an improved absorption model. *Appl. Opt.* **2016**, *55*, 8951–8961.

[47] Rothe, T.; Schmitz, M.; Kienle, A. Angular and spectrally resolved investigation of single particles by darkfield scattering microscopy. *J. Biomed. Opt.* **2012**, *17*, 117006.

[48] Preston, T. C. Mie Resonance Fitting (MRFIT). http://www.meteo.mcgill.ca/~tpreston/code.html.

[49] Sultanova, N.; Kasarova, S.; Nikolov, I. Dispersion properties of optical polymers. *Acta Phys. Pol. A* **2009**, *116*, 585–587.

Chapter 4

The wavelength-dependent complex refractive index of hygroscopic aerosol particles and other aqueous media: an effective oscillator model

Chapter Preface

In the previous chapter it was shown that the complex refractive index of a sphere having discrete absorption bands in the scattering spectrum can be determined by modeling these absorption bands with Lorentzian oscillators. Here, the oscillator model is extended in order to model the refractive index of weakly absorbing particles having no absorption bands in the visible region. Now, effective oscillator parameters describing far-UV absorption are determined for a number of atmospherically relevant solutes. These oscillator parameters will allow the complex refractive index of weakly absorbing aerosol to be determined over the full visible spectrum.

4.1 Abstract

We present an effective oscillator model for the wavelength-dependent complex refractive index of weakly absorbing aqueous solutions. The model is derived using the causal connection between the real and imaginary parts of the refractive index that is described through the Kramers-Kronig relation. Using cavity-enhanced Raman spectroscopy, we measure both the real and imaginary parts of the refractive index of several aqueous solutions whose optical properties are relevant to seawater, aqueous sea-salt particles, and aqueous organic aerosol. It is demonstrated that the effective oscillator model accurately describes both the real and imaginary parts of the refractive index of aqueous solutions across a wide range of water activities and optical wavelengths. Finally, through a comparison with measurements, we verify that mixing rule calculations utilizing oscillator parameters from solutions containing a single solute and water can be used to predict the optical properties of aqueous solutions containing multiple solutes.

4.2 Plain language summary

The interaction of light with waters such as oceans, rivers, lakes, and airborne droplets is affected by dissolved chemical species. A key quantity in our understanding of how light travels through these aqueous systems is the refractive index. Here, we develop a model that can accurately calculate the refractive index across a range of optical wavelengths. This model is validated using high-precision measurements from optically trapped droplets. Our

results will greatly improve the accuracy with which we can calculate the attenuation and scattering of solar radiation in the atmosphere and the ocean.

4.3 Introduction

A quantitative description of the propagation of light in aqueous media is important to many disciplines within atmospheric and oceanic sciences. Examples of well-studied problems range from the calculation of aerosol radiative forcing efficiency in climate models[1,2] to the analysis of the attenuation of light in natural waters[3,4]. The cases of greatest interest in these applications are ones where the aqueous solution is weakly absorbing across the visible region of the spectrum. For such solutions, the complex refractive index of the medium will have a real part that is between 1.3 and 1.6 and an imaginary part that is typically on the order of 10^{-9} to 10^{-6} at optical frequencies. Important as well is that both the real and imaginary parts vary with wavelength due to the phenomenon of dispersion.

A main goal of any theory of solution is to predict the properties of a homogeneous mixture from its pure components. The aerosol community has developed several mixing rules that can be used to calculate the real part of the refractive index of a solution of water and solutes[5]. However, the measured parameters that are used in such expressions are normally only tabulated for a single wavelength (most commonly the sodium D-line) and cannot be considered accurate at other wavelengths. The imaginary part of the refractive index is largely ignored when discussing aqueous atmospheric aerosol particles and is usually set to zero in calculations[6]. In contrast, oceanographic studies have focused a significant amount

of attention on wavelength-dependent absorption as a function of salinity[7]. Researchers can access large sample volumes in both the lab and field, thus long optical path lengths are practical and it is possible to achieve the necessary precision for attenuation measurements of weakly absorbing aqueous media[8]. Of note, the solute concentrations in these measurements would be considered to be very small by researchers interested in aqueous aerosol particles.

Spectrophotometric measurements on systems such as aqueous alkali metal nitrates, bromides, chlorides, and sulfates (e.g. $NaNO_3$, NaBr, $MgCl_2$, Na_2SO_4) have shown that, when moving from visible wavelengths into the ultraviolet (UV), significant absorption does not occur until $\lambda < 250$ nm and often not until $\lambda < 200$ nm[9,10]. Similar observations have been reported for various organic molecules (e.g. alkanes, ketones, alcohols, amides, organic acids) where Rydberg and π-π^* transitions can lead to strong absorption in the UV[10–12]. In these cases, the tail of UV absorption bands can have a significant effect on the refractive index in the visible region of the spectrum. It is currently impractical to characterize all of these electronic transitions, but what is feasible and what we show here is that their contribution to the complex refractive index at visible wavelengths can be accurately described by a single effective oscillator. The contribution of each solute to the wavelength-dependent complex refractive index of the solution can be calculated using its mass density and three oscillator parameters (strength, linewidth, and natural frequency).

Aerosol optical tweezers have enabled the retrieval of the wavelength-dependent real part of the refractive index from optically trapped droplets at various water activities[13,14]. This has primarily been made possible by fitting sharp morphology-dependent resonances (MDRs)

that appear in the optical spectra of single particles and are extremely sensitive to droplet size and refractive index[15,16]. Excellent parameterizations for the wavelength-dependent real part of the refractive index now exist for a limited number of atmospherically relevant aqueous systems[14]. The contact-free, relative humidity (RH) controlled environment that a pico- or femtoliter droplet can be held in using optical tweezers is well suited for characterizing the physical properties of aqueous solutions across a range of stable and metastable states (many of which cannot be cannot be accessed through bulk measurements). Recently, we have a developed a technique that utilizes MDRs in cavity-enhanced Raman spectra to simultaneously retrieve (i) the wavelength-dependent real part of the refractive index and (ii) the imaginary part of the refractive index at a fixed wavelength[17]. In the present study, we demonstrate how these measurements are sufficient to determine all of the parameters in the effective oscillator model mentioned above and described in detail below. Oscillator parameters are determined and tabulated for several aqueous solutes of key atmospheric interest.

4.4 The effective oscillator model for a weakly absorbing aqueous solution

For the formalism developed here, it is convenient to utilize the wavenumber, $\nu = 1/\lambda$, where λ is the vacuum wavelength of light. In a medium whose wavenumber-dependent complex refractive index is $m(\nu) = n(\nu) + ik(\nu)$, the real and imaginary parts of the refractive index

are connected through the Kramers-Kronig relations[19]:

$$n(\nu) = 1 + \frac{2}{\pi}\mathcal{P}\int_0^\infty \frac{\nu' k(\nu')}{\nu'^2 - \nu^2} d\nu', \tag{4.1}$$

$$k(\nu) = -\frac{2\nu}{\pi}\mathcal{P}\int_0^\infty \frac{n(\nu') + 1}{\nu'^2 - \nu^2} d\nu', \tag{4.2}$$

where $\mathcal{P}$ indicates that the Cauchy principal value of the integral is taken. The medium which is considered here is an aqueous solution, so $n(\nu)$ is the real part of the refractive index of the aqueous solution and $k(\nu)$ is the imaginary part of the refractive index of the aqueous solution.

In a solution with a molar concentration c_α of species α the relationship between the molar attenuation coefficient, $\varepsilon_\alpha(\nu)$, and its imaginary part of the refractive index, $k_\alpha(\nu)$, is[20]

$$k_\alpha(\nu) = \varepsilon_\alpha(\nu) c_\alpha \frac{\ln 10}{4\pi\nu}. \tag{4.3}$$

The mass concentration of species α with a molar mass M_α is defined as $\rho_\alpha = M_\alpha c_\alpha$. The imaginary part of the refractive index of the pure species α is

$$k^{(\alpha)}(\nu) = \varepsilon_\alpha(\nu) \frac{\rho^{(\alpha)}}{M_\alpha} \frac{\ln 10}{4\pi\nu}, \tag{4.4}$$

where $\rho^{(\alpha)}$ is the density of the pure component of species α.

For a solution containing N species, the total absorbance, $A(\nu)$, according to the Beer-

Lambert law, is

$$A(\nu) = \sum_{\alpha=1}^{N} A_\alpha(\nu), \tag{4.5}$$

where the individual absorbances are $A_\alpha(\nu) = \varepsilon_\alpha(\nu) b c_\alpha$ and b is the path length of the sample. We will first consider a binary solution containing water, w, and a solute, s. Therefore, the total absorbance is $A(\nu) = A_\mathrm{s}(\nu) + A_\mathrm{w}(\nu)$. Applying the definition of the individual absorbances, mass concentration, and Eq. 4.4 to the total absorbance yields the following expression for the imaginary part of the refractive index of an aqueous solution:

$$k(\nu) = \phi_\mathrm{s} k^{(\mathrm{s})}(\nu) + \phi_\mathrm{w} k^{(\mathrm{w})}(\nu), \tag{4.6}$$

where $\phi_\mathrm{s} = \rho_\mathrm{s}/\rho^{(\mathrm{s})}$ is the ratio of the mass concentration of solute to the density of pure solute and $\phi_\mathrm{w} = \rho_\mathrm{w}/\rho^{(\mathrm{w})}$ is the ratio of the mass concentration of water to the density of pure water.

We will initially treat the optical attenuation that is associated with the solute in our aqueous system with a multiple-oscillator model. In this model, each jth oscillator will contribute $k_{L,j}(\nu)$ to the imaginary part of the refractive index of the aqueous solute. The total imaginary part of the refractive index of the aqueous solute will be the summation of all $k_{L,j}(\nu)$ from a total of J oscillators. An antisymmetric Lorentzian function[21],

$$k_{L,j}(\nu) = \frac{B_j}{\pi}\left(\frac{\Gamma_j/2}{(\nu_{0,j}-\nu)^2 + (\Gamma_j/2)^2} - \frac{\Gamma_j/2}{(\nu_{0,j}+\nu)^2 + (\Gamma_j/2)^2}\right), \tag{4.7}$$

is used to model the contribution of each oscillator to the imaginary part of the refractive

index, where the parameters of the jth oscillator are the resonant wavenumber $\nu_{0,j}$, the full-width at half-maximum Γ_j, and the constant B_j. The antisymmetric Lorentzian function was chosen because (i) the imaginary part of the refractive index associated with optical transitions is well-characterized by a Lorentzian line shape and (ii) it satisfies the symmetry requirements of the Kramers-Kronig relations[22].

For J oscillators the imaginary part of the refractive index of the aqueous solute will be

$$k^{(\mathrm{s})}(\nu) = \sum_{j=1}^{J} \frac{B_j}{\pi} \left(\frac{\Gamma_j/2}{(\nu_{0,j} - \nu)^2 + (\Gamma_j/2)^2} - \frac{\Gamma_j/2}{(\nu_{0,j} + \nu)^2 + (\Gamma_j/2)^2} \right). \tag{4.8}$$

To determine expressions for both $n(\nu)$ and $k(\nu)$ we proceed as follows. First, Eq. 4.6 is inserted into Eq. 4.1 to yield

$$n(\nu) = 1 + \frac{2}{\pi} \left(\phi_{\mathrm{s}} \mathcal{P} \int_0^\infty \frac{\nu' k^{(\mathrm{s})}(\nu')}{\nu'^2 - \nu^2} d\nu' + \phi_{\mathrm{w}} \mathcal{P} \int_0^\infty \frac{\nu' k^{(\mathrm{w})}(\nu')}{\nu'^2 - \nu^2} d\nu' \right). \tag{4.9}$$

Using Eq. 4.8, the solution to the first integral on the right-hand side of Eq. 4.9 is

$$\mathcal{P} \int_0^\infty \frac{\nu' k^{(\mathrm{s})}(\nu')}{\nu'^2 - \nu^2} d\nu' = \sum_{j=1}^{J} \frac{B_j \nu_{0,j} (\nu_{0,j}^2 - \nu^2 + (\Gamma_j/2)^2)}{(\nu_{0,j}^2 - \nu^2 + (\Gamma_j/2)^2)^2 + (\nu\Gamma_j)^2}. \tag{4.10}$$

Additionally, we recognize that the real part of the refractive index of pure water, $n^{(\mathrm{w})}(\nu)$, will be

$$n^{(\mathrm{w})}(\nu) = 1 + \frac{2}{\pi} \mathcal{P} \int_0^\infty \frac{\nu' k^{(\mathrm{w})}(\nu')}{\nu'^2 - \nu^2} d\nu', \tag{4.11}$$

and this allows the second integral on the right-hand side of Eq. 4.9 to be set equal to

$n^{(\mathrm{w})}(\nu)$. Therefore, the real part of the refractive index of the aqueous solution will be

$$n(\nu) = 1 + \phi_{\mathrm{s}} \frac{2}{\pi} \sum_{j=1}^{J} \frac{B_j \nu_{0,j} (\nu_{0,j}^2 - \nu^2 + (\Gamma_j/2)^2)}{(\nu_{0,j}^2 - \nu^2 + (\Gamma_j/2)^2)^2 + (\nu\Gamma_j)^2} + \phi_{\mathrm{w}} (n^{(\mathrm{w})}(\nu) - 1). \tag{4.12}$$

When the definition of $k^{(\mathrm{s})}(\nu)$ from Eq. 4.8 is applied to Eq. 4.6, the imaginary part of the refractive index of the aqueous solution can be written as

$$k(\nu) = \phi_{\mathrm{s}} \sum_{j=1}^{J} \frac{B_j}{\pi} \left(\frac{\Gamma_j/2}{(\nu_{0,j} - \nu)^2 + (\Gamma_j/2)^2} - \frac{\Gamma_j/2}{(\nu_{0,j} + \nu)^2 + (\Gamma_j/2)^2} \right) + \phi_{\mathrm{w}} k^{(\mathrm{w})}(\nu). \tag{4.13}$$

Our interest here is in the refractive index of aqueous solutions that are weakly absorbing in the visible region of the spectrum. We will assume that the aqueous solute only strongly absorbs light at UV and higher frequencies ($\nu_{0,j} - \Gamma_j \gg \nu$) or in the infrared (IR) and far-IR ($\nu_{0,j} + \Gamma_j \ll \nu$). These conditions mean that any contributions from the aqueous solute in the IR and far-IR have a negligible effect on the refractive index in the visible region and that only high-energy absorption bands need to be considered. This should be satisfactory for many aqueous systems that are weakly absorbing in the visible region of the spectrum and, after considerable manipulation, Eqs. 4.12 and 4.13 can be approximated as

$$n(\nu) = 1 + \phi_{\mathrm{s}} \frac{2}{\pi} \frac{\tilde{B}\tilde{\nu}_0}{\tilde{\nu}_0^2 - \nu^2} + \phi_{\mathrm{w}} (n^{(\mathrm{w})}(\nu) - 1), \tag{4.14}$$

$$k(\nu) = \phi_{\mathrm{s}} \frac{2\nu}{\pi} \frac{\tilde{B}\tilde{\nu}_0\tilde{\Gamma}}{(\tilde{\nu}_0^2 - \nu^2)^2} + \phi_{\mathrm{w}} k^{(\mathrm{w})}(\nu), \tag{4.15}$$

where $\tilde{B}$ is a constant, $\tilde{\nu}_0$ is the characteristic wavenumber, and $\tilde{\Gamma}$ is the full-width at half-

maximum of the single effective oscillator that is now being used to describe all absorption that occurs at frequencies greater than those in the visible range of the spectrum.

Eqs. 4.14 and 4.15 can be generalized to aqueous media with more than two components. The resulting expressions are

$$n(\nu) = 1 + \frac{2}{\pi} \sum_{\alpha=1}^{N-1} \phi_\alpha \frac{\tilde{B}_\alpha \tilde{\nu}_{0,\alpha}}{\tilde{\nu}_{0,\alpha}^2 - \nu^2} + \phi_{\mathrm{w}}(n^{(\mathrm{w})}(\nu) - 1), \tag{4.16}$$

$$k(\nu) = \frac{2\nu}{\pi} \sum_{\alpha=1}^{N-1} \phi_\alpha \frac{\tilde{B}_\alpha \tilde{\nu}_{0,\alpha} \tilde{\Gamma}_\alpha}{(\tilde{\nu}_{0,\alpha}^2 - \nu^2)^2} + \phi_{\mathrm{w}} k^{(\mathrm{w})}(\nu), \tag{4.17}$$

where the Nth species, water, has been removed from the summation.

4.5 Materials and methods

4.5.1 Experimental

The detailed experimental procedure and schematic is presented in Text S1 and Fig. A.1 in Appendix A. Briefly, single aqueous aerosol particles were held using a dual-beam optical trap in a RH-controlled cell. Cavity-enhanced Raman spectra were collected at a fixed cell temperature and RH as the laser power was increased. Fitting the measured MDR peak positions in the Raman spectra allowed for the retrieval of $n(\nu)$ and the particle radius. The particle radius as a function of laser power was then fitted using a model for the electromagnetic heating of an aqueous droplet and a previously derived equilibrium condition[17]. The best-fit yielded k at the wavelength of the trapping laser ($\lambda = 0.532$ μm).

4.5.2 Fitting effective oscillator parameters to refractive index measurements

In Eqs. 4.14 and 4.15, both ϕ_s and ϕ_w can be determined using the measured RH in the trapping cell, calculated or parameterized water activity, and a second-order polynomial fit to tabulated density measurements for the aqueous solution. Data from reference 23 was used for the aqueous densities and the AIOMFAC model[24,25] or existing parameterizations[26] were used when determining water activities.

The complex refractive index of pure water is known from previous studies[27–30]. For instance, both $n^{(w)}$ and $k^{(w)}$ have been tabulated from $\lambda = 10$ nm to 10 m[27]. However, more accurate measurements of $n^{(w)}$ across the visible region of the spectrum will be used here[30]. Therefore, $n^{(w)}$ in Eq. 4.14 is calculated using the parameterization from reference 30 and $k^{(w)}$ in Eq. 4.15 is found through interpolation of the tabulated measurements in reference 27. For convenience, the pure water refractive index data is also presented in Text S2 and Table S1.

For each binary aqueous solution studied here, the effective oscillator parameters in Eqs. 4.14 and 4.15 were retrieved from the measured wavelength-dependent n and the measured k at a single, fixed wavelength ($\lambda = 0.532$ μm) as follows: The wavelength-dependent n that was measured at various RHs was fitted using Eq. 4.14, with $\tilde{\nu}_0$ and $\tilde{B}$ being the two fitting parameters. The third effective oscillator parameter, $\tilde{\Gamma}$, was then the only remaining unknown and was found by fitting the RH-dependent k measurements using Eq. 4.15. This methodology was thoroughly tested using synthetic refractive index data sets that were gen-

erated using Eqs. 4.12 and 4.13 with physically plausible parameters. In the visible region of the spectrum, n and k calculated using Eqs. 4.14 and 4.15 and the effective oscillator parameters of best-fit were always in excellent agreement with the refractive index calculated using Eqs. 4.12 and 4.13 (the true values for this test). This verification was also important because, unlike Eqs. 4.12 and 4.13, Eqs. 4.14 and 4.15 do not strictly satisfy the Kramers-Kronig relations.

4.6 Results and discussion

Five aqueous inorganic systems and one aqueous organic system of atmospheric relevance were investigated here. The inorganic salts, NaCl, $NaNO_3$, $(NH_4)_2SO_4$, and $MgSO_4$, were selected as they all contain species that form a significant percentage of the salt mass in seawater and aqueous sea-salt particles[32]. The aqueous organic system that was chosen, citric acid and water, has often been used as a surrogate for aqueous organic aerosol[33–35]. Using the methodology outlined in Section 4.5.1, the wavelength-dependent n and the fixed wavelength k were measured using cavity-enhanced Raman scattering from single aerosol droplets across a range of water activities. For the binary aqueous solutions, the effective oscillator parameters were then determined from these refractive index measurements following the procedure in Section 4.5.2. The parameters of best-fit are listed in Table 4.1.

For the purpose of comparison with previously reported measurements, in Fig. 4.1a-e the measured values of n are plotted at $\lambda = 0.589$ μm along with n that were calculated using the effective oscillator model. It can be seen that the measured and calculated n agree

Table 4.1: Effective oscillator parameters of best-fit for the binary aqueous solutions studied here.

Solute	$\tilde{B}$ (μm^{-1})	$\tilde{\nu}_0$ (μm^{-1})	$\tilde{\Gamma}$ (μm^{-1})
NaCl	6.86	8.51	1.66×10^{-6}
$NaNO_3$	5.69	8.41	1.20×10^{-6}
$(NH_4)_2SO_4$	7.92	10.9	2.23×10^{-6}
$MgSO_4$	8.74	10.9	2.51×10^{-6}
Citric acid	8.05	10.3	1.13×10^{-6}

well with both each other and the literature data across a large range of water activities. It is also important to emphasize that Fig. 4.1a-e clearly demonstrates the validity of the effective oscillator model in accurately describing n as a function of water activity. In Fig. 4.1f, the measured n for a ternary aqueous solution containing NaCl and $NaNO_3$ in a 1:1 molar mixture is compared to n calculated using the effective oscillator model with the fitted parameters from the respective binary aqueous solutions (i.e. the relevant parameters in Table 4.1). For this calculation we assumed that ϕ_α and ϕ_w in Eq. 4.12 could be replaced with their respective mass fractions. This simplifies the calculation as we no longer need a mass density function for the ternary solution. Even with this approximation, it can be seen in Fig. 4.1f that n calculated using the oscillator model mixing rules from Section 4.4 is in excellent agreement with the measurements.

Fig. 4.2 shows the values of k that were measured at $\lambda = 0.532$ μm and k that were calculated using the effective oscillator model at the same wavelength for the six aqueous solutions. When fitting the binary aqueous solution measurements for k, the only free parameter is $\tilde{\Gamma}$ as both $\tilde{B}$ and $\tilde{\nu}_0$ were first determined when fitting the n measurements.

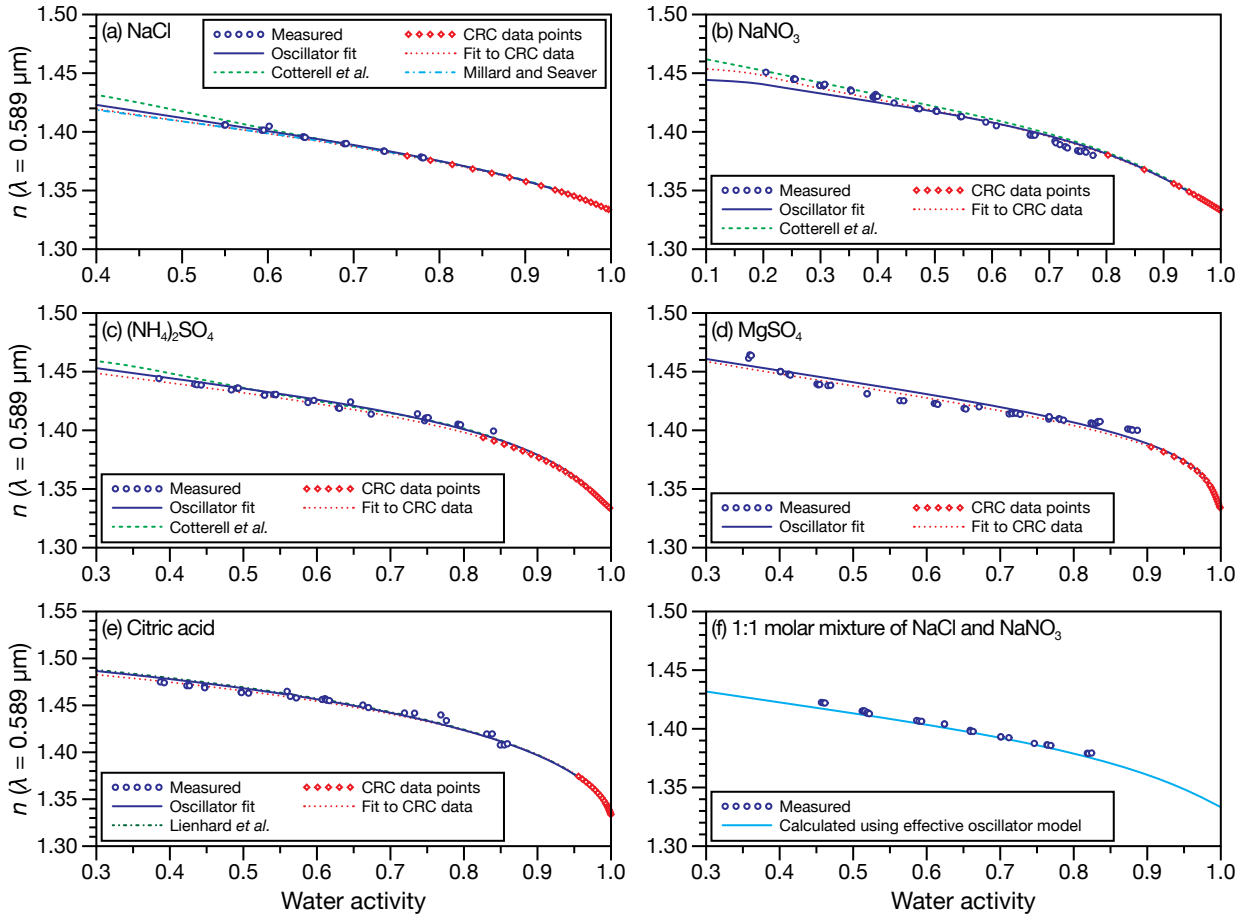

Figure 4.1: Measured and fitted real part of the refractive index, n, at $\lambda = 0.589$ μm for aqueous (a) NaCl, (b) $NaNO_3$, (c) $(NH_4)_2SO_4$, (d) $MgSO_4$, and (e) citric acid. Measurements were fitted using the effective oscillator model following the procedure described in Section 4.5.2. The fitted oscillator parameters are listed in Table 4.1. In (f), measurements of n for an aqueous 1:1 molar mixture of NaCl and $NaNO_3$ are compared to n calculated using the effective oscillator model for a ternary mixture with the fitted oscillator parameters from the binary mixtures of aqueous NaCl and aqueous $NaNO_3$. Data points from the CRC handbook[23] are shown in panels (a-e). Polynomial fits to the CRC data points as a function of mass fraction of solute are also plotted in (a-e) as a function of water activity. For further comparison, parameterizations from reference 14 are plotted in (a-c), from reference 36 in (a) and from reference 26 in (e). For the measurements shown here, error bars are smaller than the point size.

Agreement between the measurements and the oscillator model is overall good, although at low water activities the measured values of k for aqueous $MgSO_4$ (Fig. 4.2d) appear to increase much more rapidly than is predicted by the oscillator model. This rise takes place near a water activity region where gel formation is known to occur upon drying aqueous $MgSO_4$ droplets[37,38]. Therefore, it is likely the case that the refractive index calculation becomes inaccurate when the aqueous solution is not in a liquid phase state. At the very least, there is no longer any physical justification for using the refractive index of pure liquid water in a calculation where the phase state of the medium is not a liquid. In Fig. 4.2f we see that the effective oscillator mixing rule is able to accurately predict the water activity dependent k for a ternary solution. This result, along with the agreement between the experimental data and oscillator model for n, shows that it is possible to obtain the complex refractive index of a ternary solution from the oscillator parameters of a binary solution.

Next we consider the wavelength-dependent complex refractive index. Fig. 4.3 shows n (left column) and k (right column) that were calculated using the effective oscillator parameters from Table 4.1 between $\lambda = 0.3$ and 1.0 μm for the binary aqueous systems at several different water activities. In Fig. 4.3a, c, and e the activity and wavelength-dependent effective oscillator calculations are compared to the parameterizations reported by reference 14. Both results show good agreement except at high water activities in Fig. 4.3a and c and short wavelengths in Fig. 4.3e. For reference, we have also analyzed the parameterizations from reference 14 using the effective oscillator model. The resulting oscillator parameters are listed in Table 4.2.

The behaviour of k in Fig. 4.3 is straightforward to understand: at wavelengths that

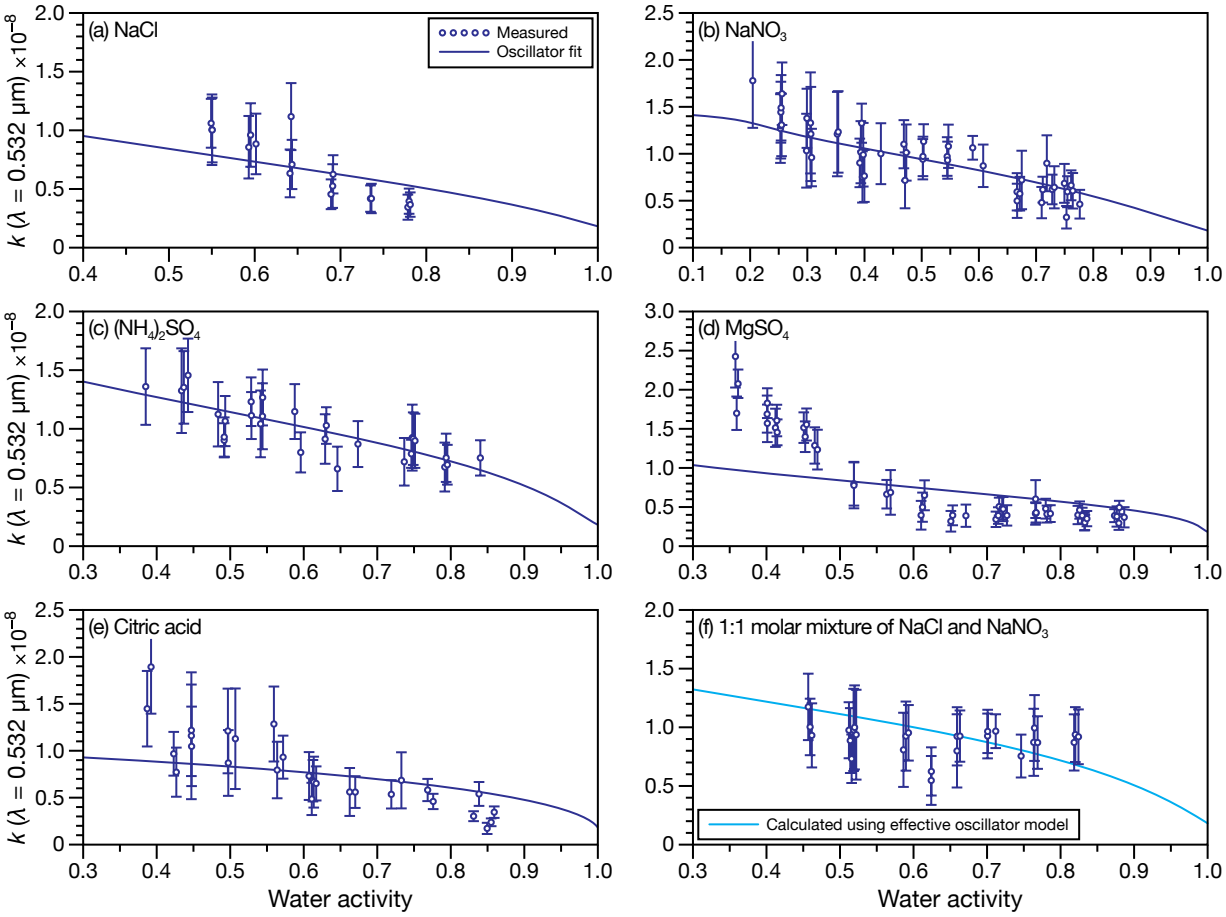

Figure 4.2: Measured and fitted imaginary part of the refractive index, k, at $\lambda = 0.532$ μm for aqueous (a) NaCl, (b) $NaNO_3$, (c) $(NH_4)_2SO_4$, (d) $MgSO_4$, and (e) citric acid. Measurements were fitted using the effective oscillator model following the procedure described in Section 4.5.2. The fitted oscillator parameters are listed in Table 4.1. In (f), measurements of k for an aqueous 1:1 molar mixture of NaCl and $NaNO_3$ are compared to k calculated using the effective oscillator model for a ternary mixture with the fitted oscillator parameters from the binary mixtures of aqueous NaCl and aqueous $NaNO_3$.

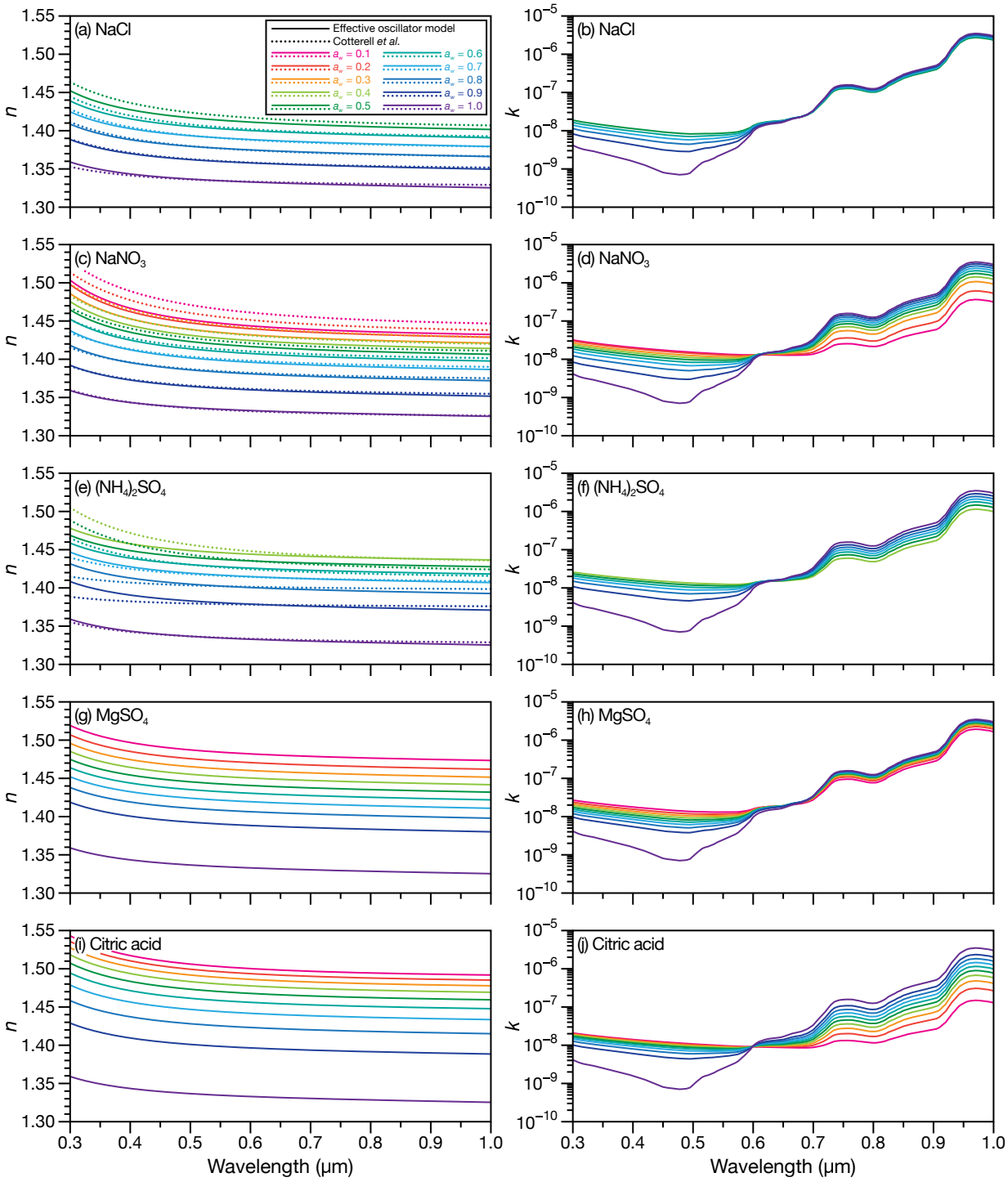

Figure 4.3: The calculated wavelength-dependent real part, n, and imaginary part, k, of the refractive index for aqueous (a and b) NaCl, (c and d) $NaNO_3$, (e and f) $(NH_4)_2SO_4$, (g and h) $MgSO_4$, and (i and j) citric acid. Both n and k were calculated at various water activities, a_w, using the effective oscillator parameters listed in Table 4.1. The wavelength and water activity-dependent n parameterizations from reference 14 are plotted in panels (a), (c) and (e).

Table 4.2: Effective oscillator parameters of best-fit for the binary aqueous solutions studied by reference 14. Note that only the real part of the refractive index was measured in that study so $\tilde{\Gamma}$ cannot be determined.

Solute	$\tilde{B}$ (μm^{-1})	$\tilde{\nu}_0$ (μm^{-1})
NaCl	5.76	7.19
$NaNO_3$	5.71	8.27
$(NH_4)_2SO_4$	8.95	12.4
NH_4HSO_4	3.91	5.56
Na_2SO_4	2.43	4.15

are close to the UV, the tail of strong UV absorption bands associated with the solute cause k to increase with increasing solute concentration (decreasing water activity), while at longer wavelengths, the strong absorption of water in the near-IR dominates, leading to a decrease in k as the water activity decreases. Unfortunately, previous wavelength-dependent k measurements for these aqueous systems are very limited and those that are available are restricted to high water activities making any meaningful comparison with our results difficult. For instance, the k measurements of aqueous NaCl presented in reference 39 are only for solutions with water activities between 0.87 and 1.0. Measurements from reference 40 were performed over the entire bulk solubility range for NaCl in water but appear to be several times too large in the region between $\lambda = 0.3$ and 0.6 μm. However, the qualitative wavelength and activity-dependent behaviour in both of those works is similar to what is observed in Fig. 4.3.

4.7 Conclusion

We have derived an effective oscillator model that describes the activity and wavelength-dependent complex refractive index of weakly absorbing aqueous media. The accuracy of the model was verified using the measured complex refractive index of several atmospherically relevant systems across a range of water activities. Measurements were taken using individual microdroplets that were held using a dual-beam optical trap in a RH-controlled cell. When possible, measurements were cross-validated with existing data from the literature. It was also demonstrated that the model can readily be used to predict the complex refractive index of mixtures with more than two components once the oscillator parameters for the pure aqueous solutes are known. Overall, the effective oscillator model and the tabulated oscillator parameters presented here should be of great use to researchers that are interested in accurate calculations of wavelength-dependent optical properties of aqueous media.

References

[1] Stier, P.; Seinfeld, J. H.; Kinne, S.; Boucher, O. Aerosol absorption and radiative forcing. *Atmos. Chem. Phys.* **2007**, *7*, 5237–5261.

[2] Turnock, S. T.; Mann, G. W.; Woodhouse, M. T.; Dalvi, M.; O'Connor, F. M.; Carslaw, K. S.; Spracklen, D. V. The impact of changes in cloud water pH on aerosol radiative forcing. *Geophys. Res. Lett.* **2019**, *46*, 4039–4048.

[3] Markager, S.; Vincent, W. F. Spectral light attenuation and the absorption of UV and blue light in natural waters. *Limnol. Oceanogr.* **2000**, *45*, 642–650.

[4] Jaffe, J. S. Underwater Optical Imaging: The Past, the Present, and the Prospects. *IEEE J. Ocean. Eng.* **2015**, *40*, 683–700.

[5] Liu, Y.; Daum, P. H. Relationship of refractive index to mass density and self-consistency of mixing rules for multicomponent mixtures like ambient aerosols. *J. Aerosol Sci.* **2008**, *39*, 974–986.

[6] Freedman, M. A.; Hasenkopf, C. A.; Beaver, M. R.; Tolbert, M. A. Optical properties of internally mixed aerosol particles composed of dicarboxylic acids and ammonium sulfate. *J. Phys. Chem. A* **2009**, *13*, 13584–13592.

[7] Pegau, W. S.; Gray, D.; Zaneveld, J. R. V. Absorption and attenuation of visible and near-infrared light in water: dependence on temperature and salinity. *Appl. Opt.* **1997**, *36*, 6035–6046.

[8] Twardowski, M. S.; Sullivan, J. M.; Donaghay, P. L.; Zaneveld, J. R. V. Microscale quantification of the absorption by dissolved and particulate material in coastal waters with an ac-9. *J. Atmospheric Ocean. Technol.* **1999**, *16*, 691–707.

[9] Ikehata, A.; Mitsuoka, M.; Morisawa, Y.; Kariyama, N.; Higashi, N.; Ozaki, Y. Effect of cations on absorption bands of first electronic transition of liquid water. *J. Phys. Chem. A* **2010**, *114*, 8319–8322.

[10] Ozaki, Y.; Tanabe, I. Far-ultraviolet spectroscopy of solid and liquid states: characteristics, instrumentation, and applications. *Analyst* **2016**, *141*, 3962–3981.

[11] Higashi, N.; Yokota, H.; Hiraki, S.; Ozaki, Y. Direct Determination of Peracetic Acid, Hydrogen Perox-

ide, and Acetic Acid in Disinfectant Solutions by Far-Ultraviolet Absorption Spectroscopy. *Anal. Chem.* **2005**, *77*, 2272–2277.

[12] Lund Myhre, C. E.; Nielsen, C. J. Optical properties in the UV and visible spectral region of organic acids relevant to tropospheric aerosols. *Atmos. Chem. Phys.* **2004**, *4*, 1759–1769.

[13] Bain, A.; Rafferty, A.; Preston, T. C. Determining the size and refractive index of single aerosol particles using angular light scattering and Mie resonances. *J. Quant. Spectrosc. Rad. Transf.* **2018**, *221*, 61–70.

[14] Cotterell, M. I.; Willoughby, R. E.; Bzdek, B. R.; Orr-Ewing, A. J.; Reid, J. P. A complete parameterisation of the relative humidity and wavelength dependence of the refractive index of hygroscopic inorganic aerosol particles. *Atmos. Chem. Phys.* **2017**, *17*, 9837–9851.

[15] Preston, T. C.; Reid, J. P. Accurate and efficient determination of the radius, refractive index, and dispersion of weakly absorbing spherical particle using whispering gallery modes. *J. Opt. Soc. Am. B* **2013**, *30*, 2113–2122.

[16] Preston, T. C.; Reid, J. P. Determining the size and refractive index of microspheres using the mode assignments from Mie resonances. *J. Opt. Soc. Am. A* **2015**, *32*, 2210–2217.

[17] Rafferty, A.; Preston, T. C. Measuring the size and complex refractive index of an aqueous aerosol particle using electromagnetic heating and cavity-enhanced Raman scattering. *Phys. Chem. Chem. Phys.* **2018**, *20*, 17038–17047.

[18] Lucarini, V.; Saarinen, J. J.; Peiponen, K.-E.; Vartiainen, E. M. *Kramers-Kronig relations in optical materials research*; Springer Science & Business Media, 2005; Vol. 110.

[19] Ref.18, p. 35.

[20] Hill, S. C.; Williamson, C. C.; Doughty, D. C.; Pan, Y.-L.; Santarpia, J. L.; Hill, H. H. Size-dependent fluorescence of bioaerosols: Mathematical model using fluorescing and absorbing molecules in bacteria. *J. Quant. Spectrosc. Rad. Transf.* **2015**, *157*, 54–70.

[21] Bain, A.; Preston, T. C. Mie scattering from strongly absorbing airborne particles in a photophoretic trap. *J. Appl. Phys.* **2019**, *125*, 093101.

[22] Gienger, J.; Groß, H.; Neukammer, J.; Bär, M. Determining the refractive index of human hemoglobin

solutions by Kramers–Kronig relations with an improved absorption model. *Appl. Opt.* **2016**, *55*, 8951–8961.

[23] Lide, D. R. *CRC handbook of chemistry and physics*, 82nd ed.; CRC Press, 2002.

[24] Zuend, A.; Marcolli, C.; Luo, B. P.; Peter, T. A thermodynamic model of mixed organic-inorganic aerosols to predict activity coefficients. *Atmos. Chem. Phys.* **2008**, *8*, 4559–4593.

[25] Zuend, A. Aerosol Inorganic-Organic Mixtures Functional groups Activity Coefficients (AIOMFAC) website and online model. 2019; https://aiomfac.lab.mcgill.ca, last accessed: 2019-06-23.

[26] Lienhard, D. M.; Bones, D. L.; Zuend, A.; Krieger, U. K.; Reid, J. P.; Peter, T. Measurements of thermodynamic and optical properties of selected aqueous organic and organic - inorganic mixtures of atmospheric relevance. *J. Phys. Chem. A* **2012**, *116*, 9954–9968.

[27] Segelstein, D. J. The complex refractive index of water (M.Sc. Thesis, University of Missouri). 1981.

[28] Pope, R. M.; Fry, E. S. Absorption spectrum (380-700 nm) of pure water. II. Integrating cavity measurements. *Appl. Opt.* **1997**, *36*, 8710–8723.

[29] Fry, E. S. Reply to criticisms of the Pope and Fry paper on pure water absorption made in a comment by Quickenden et al. *Appl. Opt.* **2000**, *39*, 5843–5846.

[30] Daimon, M.; Masumura, A. Measurement of the refractive index of distilled water from the near-infrared region to the ultraviolet region. *Appl. Opt.* **2007**, *46*, 3811–3820.

[31] Seinfeld, J. H.; Pandis, S. N. *Atmospheric chemistry and physics: from air pollution to climate change*, 3rd ed.; John Wiley & Sons, 2016.

[32] Ref.31, pp. 352–354.

[33] Murray, B. J. Inhibition of ice crystallisation in highly viscous aqueous organic acid droplets. *Atmos. Chem. Phys.* **2008**, *8*, 5423–5433.

[34] Murray, B. J.; Wilson, T. W.; Dobbie, S.; Cui, Z.; Al-Jumur, S. M. R. K.; Möhler, O.; Schnaiter, M.; Wagner, R.; Benz, S.; Niemand, M.; Saathoff, H.; Ebert, V.; Wagner, S.; Kärcher, B. Heterogeneous nucleation of ice particles on glassy aerosols under cirrus conditions. *Nat. Geosci.* **2010**, *3*, 233–237.

[35] Wallace, B. J.; Preston, T. C. Water uptake and loss in viscous aerosol particles with concentration-dependent diffusivities. *J. Phys. Chem. A* **2019**, *123*, 3374–3382.

[36] Millard, R.; Seaver, G. An index of refraction algorithm for seawater over temperature, pressure, salinity, density, and wavelength. *Deep Sea Res. Part 1 Oceanogr. Res. Pap.* **1990**, *37*, 1909–1926.

[37] Cai, C.; Tan, S.; Chen, H.; Ma, J.; Wang, Y.; Reid, J. P.; Zhang, Y. Slow water transport in $MgSO_4$ aerosol droplets at gel-forming relative humidities. *Phys. Chem. Chem. Phys.* **2015**, 29753–29763.

[38] Davies, J. F.; Wilson, K. R. Raman spectroscopy of isotopic water diffusion in ultraviscous, glassy, and gel states in aerosol by use of optical tweezers. *Anal. Chem.* **2016**, *88*, 2361–2366.

[39] Wang, C. C.; Tan, J.; Liu, L. Wavelength and concentration-dependent optical multi-component mixed-salt solutions. *Appl. Opt.* **2017**, *56*, 7662–7671.

[40] Li, X.; Liu, L.; Zhao, J.; Tan, J. Optical properties of sodium chloride solution within the spectral range from 300 to 2500 nm at room temperature. *Appl. Spectrosc.* **2015**, *69*, 635–640.

Chapter 5

The wavelength-dependent optical properties of weakly absorbing aqueous aerosol particles

Chapter Preface

In the previous chapter it was shown that the complex refractive index of weakly absorbing aerosol can be determined by modeling the core electron transitions of a solute with an effective Lorentzian oscillator characterized by three parameters. It was also shown that using mixing rules, the refractive index of ternary solutions can be determined using these oscillator parameters. To further extend the model, here, effective oscillator parameters are determined for individual ions, making it possible to determine the refractive index from easily measured ion mass fractions. Finally, the effect of temperature on the refractive index in the oscillator model is explored.

5.1 Abstract

The refractive index (RI) is a key quantity in calculating many aerosol properties required for climate models. To accurately describe the RI of aerosol, the wavelength and temperature dependence as well as the variation with aerosol water content must be considered. Aside from water, aged ambient aerosol can contain both inorganic salts and a myriad of organic molecules. Determining the optical properties of each organic molecule and their contribution to the aerosol as a whole would be an incredibly time consuming and, in many cases, intractable task. Using single aerosol particle spectroscopy measurements and an effective oscillator model, we are able to measure parameters that can be used to accurately calculate the wavelength-dependent RI of mixed organic-inorganic aqueous aerosol particles. Measured oscillator parameters are presented for a number of atmospherically relevant inorganic ions and surrogate organic species. Finally, the effect of temperature on the oscillator parameters is investigated.

5.2 An effective oscillator model for individual ions and organics

Hygroscopic aerosol in the atmosphere undergoes changes in composition as it travels through air of varying relative humidity (RH) by taking up or losing water to remain in equilibrium with its surroundings. This change in composition alters aerosol optical properties as the concentration of solute changes.[1] Refractive index (RI) is an important parameter when

calculating the scattering and absorption of electromagnetic radiation by aerosol. Due to the broad spectrum of the Sun, it is necessary to ascertain the RI over the full visible spectrum.[2] Although the RI is a complex quantity with the real part describing scattering and the imaginary part describing absorption, the imaginary part of the RI for weakly absorbing hygroscopic aerosol in the visible region is often on the order of 10^{-9} – 10^{-8} and is commonly approximated as zero.[3,4]

The real and imaginary parts of the RI are linked through a causal connection described by the Kramers-Kronig relation.[5] Even in a weakly absorbing medium, the real part of the RI is tied to absorption. For instance, it is the tail of strong electron transitions in the far-ultraviolet (UV) which gives rise to the RI in the visible region for weakly absorbing aqueous solutions.[3,6] These far-UV transitions can be observed spectroscopically thanks to advances in far-UV spectroscopy which overcome the strong absorption at short wavelengths (140–200 nm) and allow for the characterization of electronic transitions, e.g. Rydberg and $\pi - \pi^*$ transitions in liquids and solids.[7] We have previously shown that for the purposes of calculating the RI of aqueous solutions in the visible region, all of these transitions can be accurately represented with a single effective oscillator that describes absorption of light at UV energies or greater. For solute α, the oscillator is characterized by a resonant wavenumber, $\tilde{\nu}_{0,\alpha}$, a constant, $\tilde{B}_\alpha$, and a full-width at half-maximum, $\tilde{\Gamma}_\alpha$. Only $\tilde{\nu}_{0,\alpha}$ and $\tilde{B}_\alpha$ are required to calculate the real part of the RI, $n(\nu)$, which, for an aqueous solution containing J solutes, is

$$n(\nu) = 1 + \sum_{\alpha=1}^{J} \phi_\alpha \frac{2}{\pi} \frac{\tilde{B}_\alpha \tilde{\nu}_{0,\alpha}}{\tilde{\nu}_{0,\alpha}^2 - \nu^2} + \phi_{\mathrm{w}}(n^{(\mathrm{w})}(\nu) - 1), \tag{5.1}$$

where the wavenumber is $\nu = 1/\lambda$, λ is the vacuum wavelength of light, and $n^{(w)}(\nu)$ is the real part of the RI for pure water. Here, we simplify the model by approximating ϕ_w and ϕ_α to be the mass fractions of the water and solute, respectively (technically they are relative densities but this mass fraction approximation was found to be excellent for the aqueous systems considered here). For inorganic solutes, we also allow each cation and anion to be separately characterized by an effective oscillator. As will be shown, this increases the flexibility of the model when dealing with multicomponent mixtures and mixtures for which no measurements exist.

Mie resonance spectroscopy measurements on single, optically trapped particles were taken using two previously described setups[4,8] and used here to determine the wavelength-dependent RI of many different binary aqueous droplets across a range of RHs. Experimental details are provided in Appendix B. Mie resonance peaks from either broadband scattering or cavity-enhanced Raman scattering (CERS) spectra were fitted to obtain droplet size and RI using the MRFIT algorithm.[9] With these single particle RI measurements, we were able to fit oscillator parameters for inorganic ions by simultaneously minimizing the error across all measurements using a modified version of our previous fitting scheme.[3] Hygroscopic and low volatility solutes of either direct atmospheric relevance or relevance as surrogates were chosen for this study. The retrieved parameters for both organic solutes and inorganic ions are tabulated in Table 5.1. With the exception of Li^+, all of the ions in Table 5.1 are of tropospheric relevance.[10]

In Fig. 5.1, we compare the $n(\nu)$ calculated using Eq. 5.1 and the appropriate $\tilde{\nu}_{0,\alpha}$ and $\tilde{B}_\alpha$ from Table 5.1 to a wide range of measurements,[11,12] including those taken here, at

Table 5.1: Measured effective oscillator parameters for aqueous ions and organic solutes. Parameters were measured at $T = 295$ K.

Species	$\tilde{B}_\alpha$ (μm^{-1})	$\tilde{\nu}_{0,\alpha}$ (μm^{-1})	Species	$\tilde{B}_\alpha$ (μm^{-1})	$\tilde{\nu}_{0,\alpha}$ (μm^{-1})
NH_4^+	3.75	5.93	Br^-	7.10	8.69
Ca^{2+}	8.81	8.95	NO_3^-	5.86	8.41
Li^+	4.96	7.30	H^+	0.00	0.00
Mg^{2+}	7.41	7.12	Malonic acid	6.82	9.76
Na^+	6.40	9.70	Glutaric acid	6.99	9.64
K^+	5.79	9.60	Citric acid	7.80	10.37
Cl^-	9.59	11.10	Tartaric acid	7.83	10.35
HSO_4^-	5.19	7.48	Sucrose	9.26	11.49
SO_4^{2-}	12.37	15.95	Mannose	8.80	10.91

$\lambda = 0.589$ μm (the sodium D-line, the wavelength where the RI is typically measured with an Abbe refractometer). The agreement is excellent, although in some cases discrepancies are seen between the calculation and the single particle measurements at high mass fractions. As these cases are above the bulk solubility limit, these metastable droplets may have undergone a phase change and the measurements may no longer be representative of a well-mixed solution leading to the observed differences. For example, KNO_3 has been found to dry slowly, never undergoing efflorescence but becoming highly concentrated and $MgSO_4$ forms a gel under low RH conditions.[13,14]

Evaluating the accuracy of the wavelength-dependent calculations is more challenging as there is a dearth of suitable measurements in the literature. However, aqueous NaCl is the exception and its wavelength-dependent RI has been well-studied. In Fig. 5.2a, we

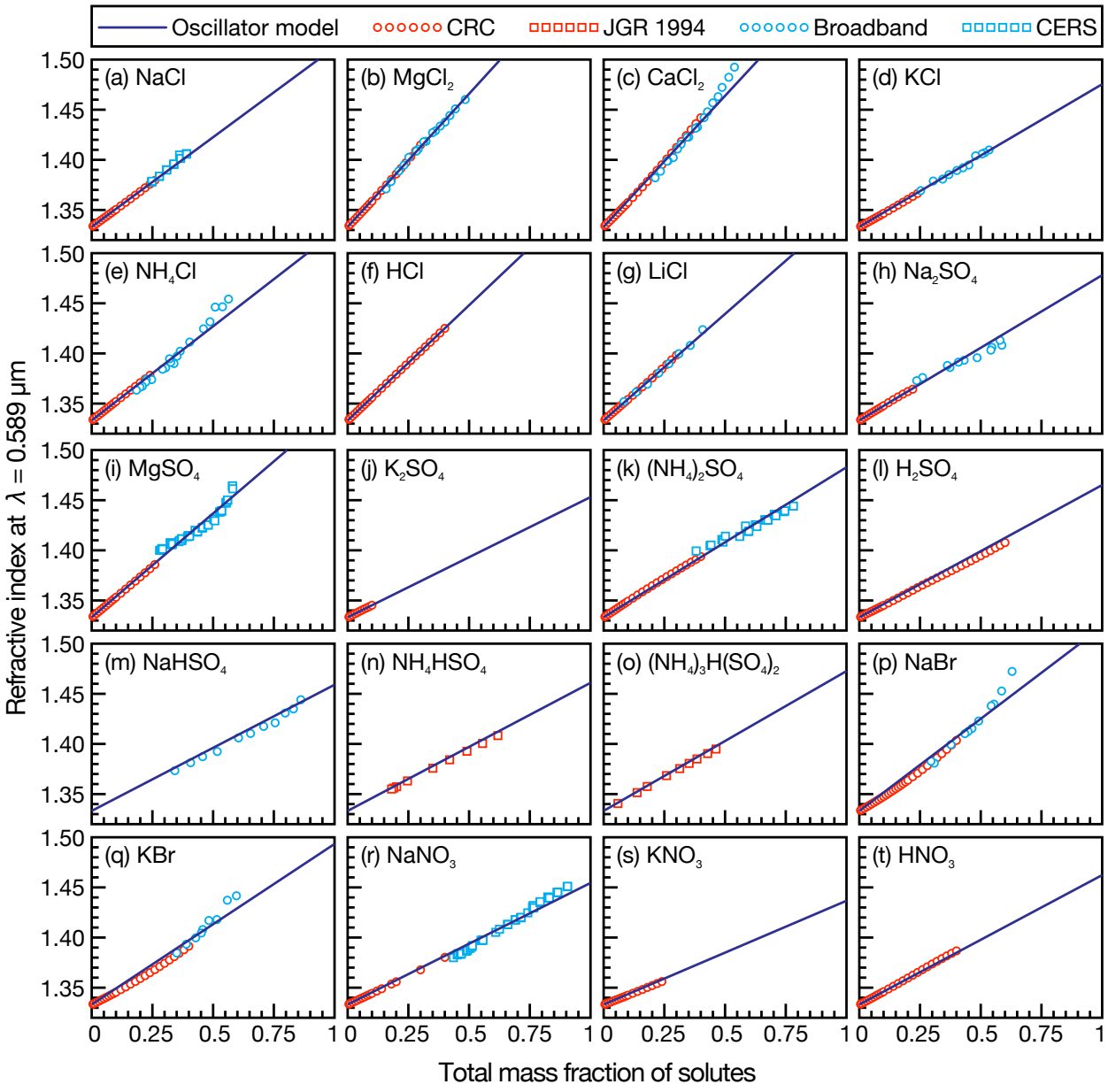

Figure 5.1: Comparison between bulk refractometer measurements (red points), single particle measurements (blue points), and effective oscillator calculation (solid line) for various aqueous inorganic solutions as a function of mass fraction of solute. All RI measurements are at $\lambda = 0.589$ μm. Bulk measurements are from either Ref. 11 (labeled 'CRC') or Ref. 12 (labeled 'JGR 1994').

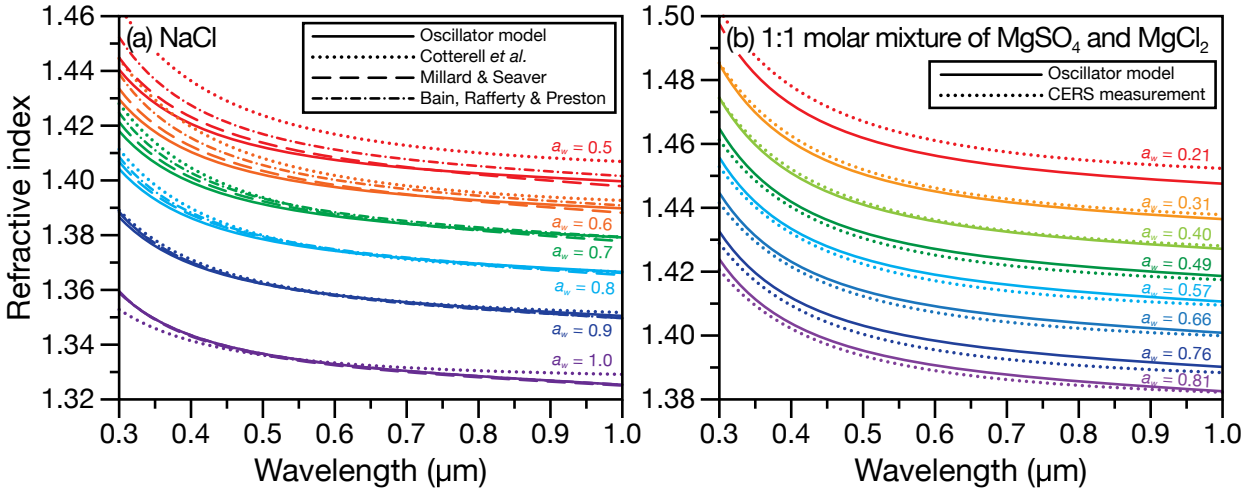

Figure 5.2: Comparison between the wavelength-dependent RI at various water activities, a_w, for (a) aqueous NaCl calculated using the effective oscillator model and parameterizations from Refs. 3, 15, and 16, and (b) aqueous 1:1 molar mixture of $MgSO_4$ and $MgCl_2$ calculated using the effective oscillator model and single particle CERS measurements. For the effective oscillator calculation, mass fractions here and in Fig. 5.3c were determined from water activities using the AIOMFAC model.[17,18]

compare the RI of aqueous NaCl calculated using the effective oscillator model (Eq. 5.1 and the parameters for Na^+ and Cl^- in Table 5.1) to previous RI results for the same system. Fig. S2 in Appendix B shows the percent difference between the previous results and the oscillator model. Discrepancies appear at low water activities (high mass fractions of solute) and at short wavelengths. With the exception of the parameterization from Cotterell *et al.* at water activities of 0.5 and 0.6, the oscillator model agrees with the previous aqueous NaCl results to within 1%. In Fig. 5.2b, we consider a solution with more species present (a 1:1 molar mixture of $MgSO_4$ and $MgCl_2$). The oscillator model calculation matches extremely well with our CERS measurements over a wide range of water activities, demonstrating its potential for wavelength-dependent RI calculations of complex multicomponent inorganic mixtures using mass fractions and parameters from Table 5.1.

Next, we consider organic solutes. It has been estimated that more than 10,000 unique organic compounds have been measured in the atmosphere.[19] Volatile organic compounds (VOCs) emitted either biogenically or anthropogenically undergo oxidation in the atmosphere principally by hydroxyl radicals, ozone, nitrate radicals or photolysis. The oxidant, as well as the temperature and RH all play a role in the subsequent reaction pathway; with different conditions often leading to different products. The oxidation of VOCs generates more polar organic molecules containing functional groups such as alcohols, aldehydes, carboxylic acids and ketones making these molecules less volatile and more water soluble than their precursors. These oxidized organics can then condense to form secondary organic aerosol (SOA).[20] As thousands of unique oxidized molecules can make up the organic fraction of aerosol,[21] it is a near impossible task to determine how each of these molecules affects aerosol properties, including the aerosol optical properties necessary for climate modeling. Aerosol mass spectrometry allows for the rapid determination of aerosol properties, but detailed structural information requires time consuming molecular separation.[20]

Attenuated total reflection far-UV (ATR-FUV) spectra of linear hydrocarbons and isomers of C_6H_{14} (see Fig. 4 in Ref. 7) show maximum absorptions at wavelengths $\approx$ 150 nm with a slight red shift and increase in peak intensity with increased molar mass. ATR-FUV spectra of aliphatic and branched ketones show a shift in peak intensity to $\approx$ 160 nm as does methanol. Unfortunately, there are only examples of ATR-FUV spectra for few classes of organic molecules. Nevertheless, these examples demonstrate that the far-UV transitions of organic molecules of similar size and functionality are alike. As these transitions govern RI in the visible region, this observation suggests that they will also have similar RIs. Ef-

forts have previously been made to predict the RI of SOA based on quantitative structural properties[22] and to predict the RI of pure component organics using group contribution models.[23–25] However, these models predict the RI at a single wavelength, neglecting dispersion, and consider only dry conditions. It would be beneficial to determine the RI of the organic fraction over a range of water contents and over the full visible spectrum using only these predictors routinely determined for ambient aerosol.

In Fig. 5.3a, the RI at $\lambda = 0.589$ μm for three classes of organic molecules are plotted as function of solute mass fraction in water. Many of the molecules in the three groups highlighted in Fig. 5.3a are often chosen as surrogate species for the organic material that is present in SOA.[26–28] When their RIs are plotted as a function of solute mass fraction, these molecules become grouped by their listed classes (with a couple of exceptions). Fig. 5.3b indicates that this should also apply to the wavelength-dependent RI. We compare oscillator calculations using parameters from aqueous sucrose and aqueous mannose measured here and see that, when their mass fractions are the same, the plotted curves are nearly identical. However, in Fig. 5.3a we also see that tartaric and malic acid are not grouped with the other 12 dicarboxylic acids. This is likely because, unlike those other dicarboxylic acids, tartaric and malic acid also contain hydroxyl groups. Therefore, using representative species for groups of components in a complex organic mixture can be a suitable approach for RI calculations but the classification of molecules needs to be carefully considered. Alternatively, a group contribution approach could be developed but that is beyond the scope of the current work. Fig. 5.3c shows the measured and calculated wavelength-dependent RI of an aqueous organic-inorganic droplet (containing sucrose, Na^+, and Cl^-). There is a very close match

between the measurement and the effective oscillator calculation when the correct sucrose-NaCl mixing ratio is used in the model. The calculated RI for both aqueous sucrose and aqueous NaCl are also shown to emphasize that ignoring either the organic or inorganic component in the aqueous organic-inorganic calculation will not yield an accurate prediction of the RI.

We now apply the effective oscillator model to waters found in oceans and atmospheric aerosol by considering the specific examples of brine and polar stratospheric aerosol. In both cases, we will need to consider the effect of temperature on the RI. If we assume that its main effect will be on $\tilde{B}_\alpha$ rather than $\tilde{\nu}_{0,\alpha}$, then we can expand $\tilde{B}_\alpha$ as a first-order Taylor series around the temperature where the oscillator parameter was measured, T_0, to yield $\tilde{B}_\alpha(T) = \tilde{B}_\alpha(T_0) + \tilde{B}'_\alpha(T_0)(T - T_0)$, where $\tilde{B}_\alpha(T_0)$ corresponds to the values listed in Table 5.1 and, in this work, $\tilde{B}'_\alpha(T_0)$ will simply be set to $\tilde{B}'_\alpha(T_0) = \kappa\tilde{B}_\alpha(T_0)$ where κ is a constant. As will be demonstrated, for the atmospheric and oceanic systems considered here, this is the only modification to the oscillator model that is needed to satisfactorily account for the effect of temperature on the calculated RI .

In Fig. 5.4, the composition[29] and RI[30] of sea ice brine at sub-zero temperatures are shown. The multicomponent solution contains six different ions whose mass fractions change with temperature (Fig. 5.4a). In Fig. 5.4b, it can be seen that if the temperature dependence is ignored, the oscillator model calculations are systematically too small. However, if a temperature dependence is included in the model, the agreement is excellent.

Polar stratospheric clouds are primarily composed of supercooled particles containing H_2O, H_2SO_4, and HNO_3.[31] Fig. 5.5 compares measurements[32] for one such ternary solution

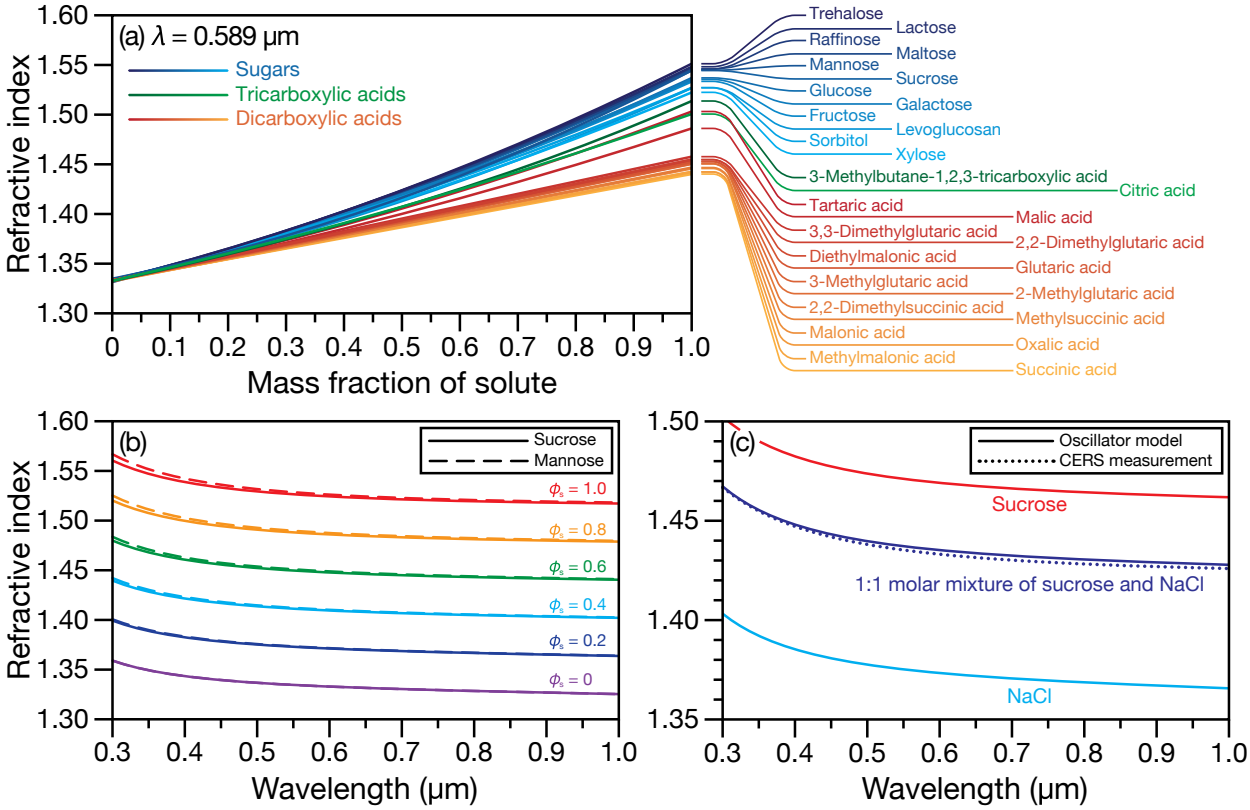

Figure 5.3: (a) Comparison between the RI at $\lambda = 0.589$ μm for organic solutes in water. Measurements in (a) were taken from various sources [11,26–28] and were either plotted using the reported parameterization or fitted here as a function of solute mass fraction. Comparison between the wavelength-dependent RI for (b) aqueous sucrose and aqueous mannose at various solute mass fractions, ϕ_s, and (c) aqueous 1:1 molar mixture of sucrose and NaCl calculated using the effective oscillator model and single particle CERS measurements at a water activity of 0.81.

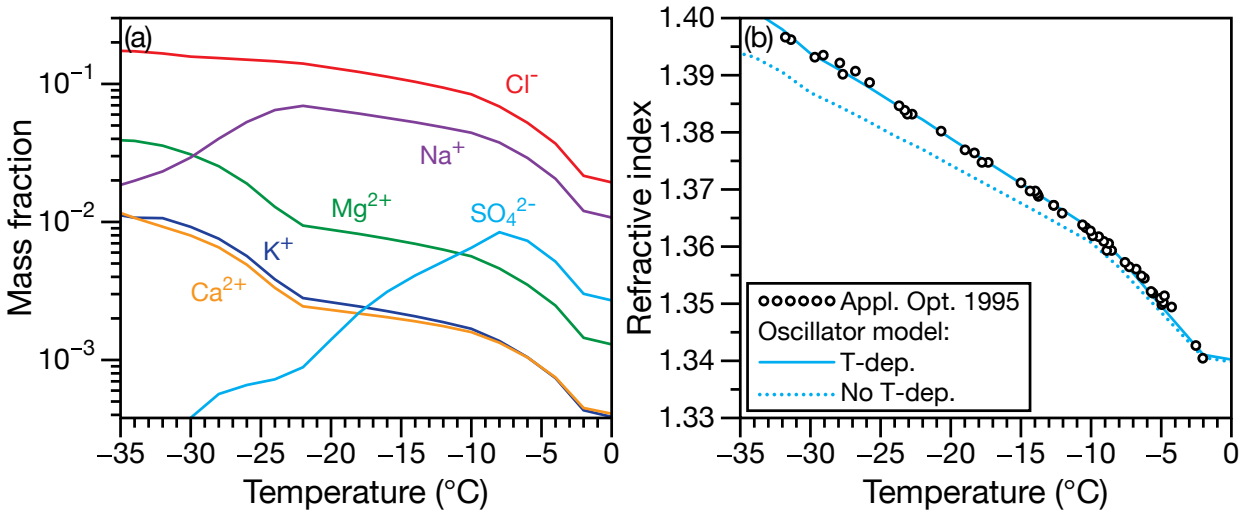

Figure 5.4: (a) Mass fraction of inorganic ions in sea-water[29] and (b) corresponding RI measurements at $\lambda = 0.589$ μm.[30] In (b) the RI calculated using the effective oscillator model is shown without (dotted line) and with (solid line) a temperature dependence ($\kappa = -0.0010$ K^{-1}).

at four different wavelengths to oscillator calculations for temperatures from -60°C to 30°C. The model has satisfactory agreement with the experimental data in the visible region but becomes inaccurate in the UV (similar to the results in Fig. 5.2a).

In summary, with oscillator parameters that are measured using Mie resonance spectroscopy and presented here, the effective oscillator model can be used to accurately calculate the wavelength-dependent and temperature-dependent RI for weakly absorbing aqueous media containing both inorganic ions and organic solutes. Mixing rules based on mass fractions allow for the straightforward calculation of the wavelength-dependent RI of multicomponent aqueous inorganic-organic solutions. The focus of our attention and results has been on aqueous systems that are relevant to hygroscopic tropospheric and stratospheric aerosol particles but we have also considered one case that is relevant to the liquid water phase in

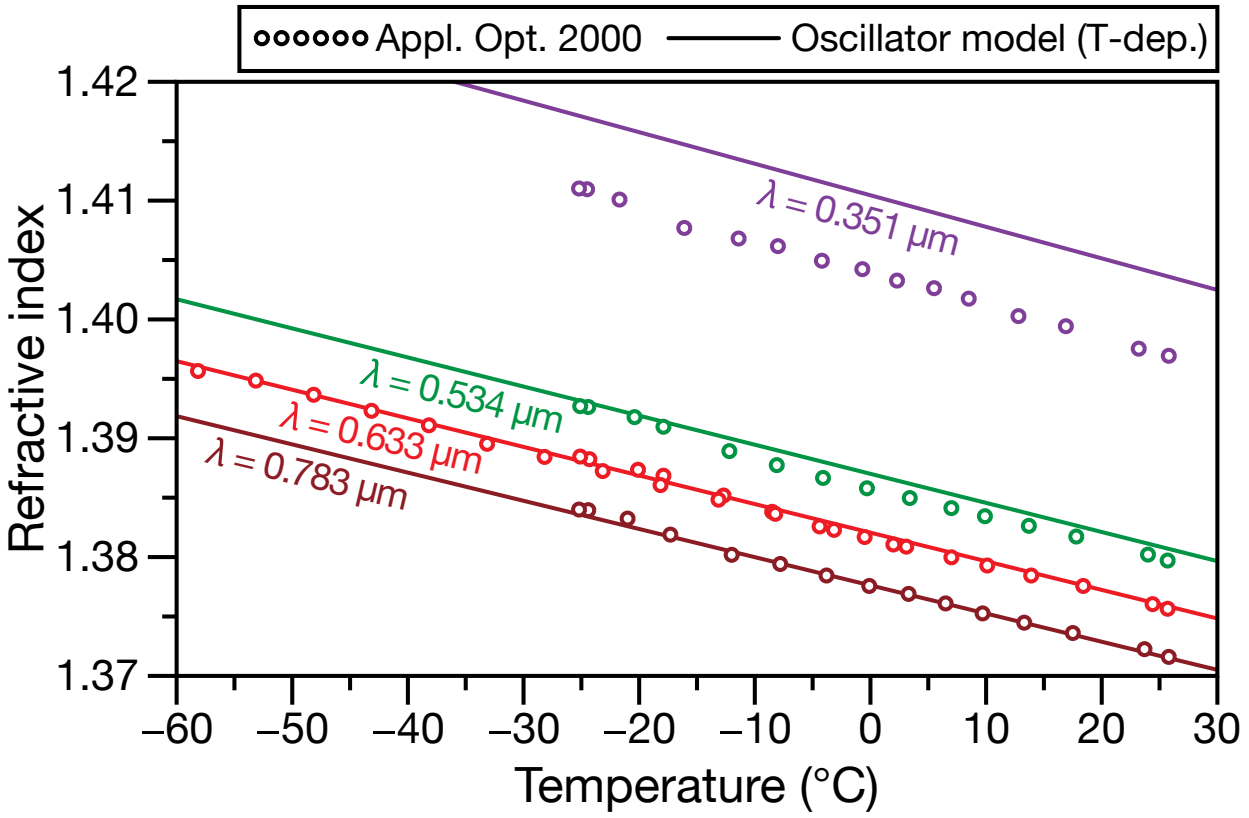

Figure 5.5: RI measurements at four different wavelengths for an aqueous solution containing H_2SO_4 and HNO_3 ($\phi_{H_2SO_4} = 0.1741$ and $\phi_{HNO_3} = 0.1741$) from Ref. 32 compared to the temperature-dependent effective oscillator model ($\kappa = -0.0015$ K^{-1}).

sea ice. Therefore, the effective oscillator model from this work could also be applied without any modifications to waters in oceans, rivers, and lakes. We plan to more fully explore temperature effects on the RI in future work.

References

[1] Walker, J. S.; Wills, J. B.; Reid, J. P.; Wang, L.; Topping, D. O.; Butler, J. R.; Zhang, Y. H. Direct comparison of the hygroscopic properties of ammonium sulfate and sodium chloride aerosol at relative humidities approaching saturation. *J. Phys. Chem. A* **2010**, *114*, 12682–12691.

[2] Alvarado, M. J.; Lonsdale, C. R.; MacIntyre, H. L.; Bian, H.; Chin, M.; Ridley, D. A.; Heald, C. L.; Thornhill, K. L.; Anderson, B. E.; Cubison, M. J.; Jimenez, J. L.; Kondo, Y.; Sahu, L. K.; Dibb, J. E.; Wang, C. Evaluating model parameterizations of submicron aerosol scattering and absorption with in situ data from ARCTAS 2008. *Atmos. Chem. Phys.* **2016**, *16*, 9435–9455.

[3] Bain, A.; Rafferty, A.; Preston, T. C. The Wavelength-Dependent Complex Refractive Index of Hygroscopic Aerosol Particles and Other Aqueous Media: An Effective Oscillator Model. *Geophys. Res. Lett.* **2019**, *46*, 10636–10645.

[4] Rafferty, A.; Preston, T. C. Measuring the size and complex refractive index of an aqueous aerosol particle using electromagnetic heating and cavity-enhanced Raman scattering. *Phys. Chem. Chem. Phys.* **2018**, *20*, 17038–17047.

[5] Lucarini, V.; Saarinen, J. J.; Peiponen, K.-E.; Vartiainen, E. M. *Kramers-Kronig relations in optical materials research*; Springer Science & Business Media, 2005; Vol. 110.

[6] Gienger, J.; Groß, H.; Neukammer, J.; Bär, M. Determining the refractive index of human hemoglobin solutions by Kramers–Kronig relations with an improved absorption model. *Appl. Opt.* **2016**, *55*, 8951–8961.

[7] Ozaki, Y.; Tanabe, I. Far-ultraviolet spectroscopy of solid and liquid states: Characteristics, instrumentation, and applications. *Analyst* **2016**, *141*, 3962–3981.

[8] Lew, L. J. N.; Ting, M. V.; Preston, T. C. Determining the size and refractive index of homogeneous spherical aerosol particles using Mie resonance spectroscopy. *Appl. Opt.* **2018**, *57*, 4601–4609.

[9] Preston, T. C.; Reid, J. P. Determining the size and refractive index of microspheres using the mode assignments from Mie resonances. *J. Opt. Soc. Am. A* **2015**, *32*, 2210–2217.

[10] Stelson, A. W. Urban aerosol refractive index prediction by partial molar refraction approach. *Environ. Sci. Technol.* **1990**, *24*, 1676–1679.

[11] Rumble, J. R. *CRC handbook of chemistry and physics*, 100th ed.; CRC Press, 2019.

[12] Tang, I. N.; Munkelwitz, H. R. Water activities, densities and refractive indices of aqueous sulfates and sodium nitrate droplets of atmospheric importance. *J. Geophys. Res.* **1994**, *99*, 18801–18808.

[13] Freney, E. J.; Martin, S. T.; Buseck, P. R. Deliquescence and efflorescence of potassium salts relevant to biomass-burning aerosol particles. *Aerosol Sci. Technol.* **2009**, *43*, 799–807.

[14] Davies, J. F.; Wilson, K. R. Raman Spectroscopy of Isotopic Water Diffusion in Ultraviscous, Glassy, and Gel States in Aerosol by Use of Optical Tweezers. *Anal. Chem.* **2016**, *88*, 2361–2366.

[15] Millard, R.; Seaver, G. An index of refraction algorithm for seawater over temperature, pressure, salinity, density, and wavelength. *Deep Sea Res. Part 1 Oceanogr. Res. Pap.* **1990**, *37*, 1909–1926.

[16] Cotterell, M. I.; Willoughby, R. E.; Bzdek, B. R.; Orr-Ewing, A. J.; Reid, J. P. A complete parameterisation of the relative humidity and wavelength dependence of the refractive index of hygroscopic inorganic aerosol particles. *Atmos. Chem. Phys.* **2017**, *17*, 9837–9851.

[17] Zuend, A.; Marcolli, C.; Luo, B. P.; Peter, T. A thermodynamic model of mixed organic-inorganic aerosols to predict activity coefficients. *Atmos. Chem. Phys.* **2008**, *8*, 4559–4593.

[18] Zuend, A. Aerosol Inorganic-Organic Mixtures Functional groups Activity Coefficients (AIOMFAC) website and online model. 2019; https://aiomfac.lab.mcgill.ca, last accessed: 2019-11-28.

[19] Goldstein, A. H.; Galbally, I. E. Known and unexplored organic constituents in the earth's atmosphere. *Environ. Sci. Technol.* **2007**, *41*, 1514–1521.

[20] Hallquist, M. et al. The formation, properties and impact of secondary organic aerosol: Current and emerging issues. *Atmos. Chem. Phys.* **2009**, *9*, 5155–5236.

[21] George, C.; Ammann, M.; D'Anna, B.; Donaldson, D. J.; Nizkorodov, S. A. Heterogeneous photochemistry in the atmosphere. *Chem. Rev.* **2015**, *115*, 4218–4258.

[22] Redmond, H.; Thompson, J. E. Evaluation of a quantitative structure-property relationship (QSPR)

for predicting mid-visible refractive index of secondary organic aerosol (SOA). *Phys. Chem. Chem. Phys.* **2011**, *13*, 6872–6882.

[23] Gharagheizi, F.; Ilani-Kashkouli, P.; Kamari, A.; Mohammadi, A. H.; Ramjugernath, D. Group contribution model for the prediction of refractive indices of organic compounds. *J. Chem. Eng. Data* **2014**, *59*, 1930–1943.

[24] Cai, C.; Marsh, A.; Zhang, Y. H.; Reid, J. P. Group contribution approach to predict the refractive index of pure organic components in ambient organic aerosol. *Environ. Sci. Technol.* **2017**, *51*, 9683–9690.

[25] Bouteloup, R.; Mathieu, D. Improved model for the refractive index: Application to potential components of ambient aerosol. *Phys. Chem. Chem. Phys.* **2018**, *20*, 22017–22026.

[26] Lienhard, D. M.; Bones, D. L.; Zuend, A.; Krieger, U. K.; Reid, J. P.; Peter, T. Measurements of thermodynamic and optical properties of selected aqueous organic and organic - inorganic mixtures of atmospheric relevance. *J. Phys. Chem. A* **2012**, *116*, 9954–9968.

[27] Lienhard, D. M. et al. Viscous organic aerosol particles in the upper troposphere: Diffusivity-controlled water uptake and ice nucleation? *Atmos. Chem. Phys.* **2015**, *15*, 13599–13613.

[28] Cai, C.; Miles, R. E.; Cotterell, M. I.; Marsh, A.; Rovelli, G.; Rickards, A. M.; Zhang, Y. H.; Reid, J. P. Comparison of methods for predicting the compositional dependence of the density and refractive index of organic-aqueous aerosols. *J. Phys. Chem. A* **2016**, *120*, 6604–6617.

[29] Richardson, C. Phase Relationships in Sea Ice as a Function of Temperature. *J. Glaciol.* **1976**, *17*, 507–519.

[30] Maykut, G. A.; Light, B. Refractive-index measurements in freezing sea-ice and sodium chloride brines. *Appl. Opt.* **1995**, *34*, 950–961.

[31] Schreiner, J.; Voigt, C.; Kohlmann, A.; Arnold, F.; Mauersberger, K.; Larsen, N. Chemical analysis of polar stratospheric cloud particles. *Science* **1999**, *283*, 968–970.

[32] Krieger, U. K.; Peter, T.; Luo, B.; Weers, U.; Mössinger, J. C. Measurement of the refractive indices of h_2so_4-hno_3-h_2o solutions to stratospheric temperatures. *Appl. Opt.* **2000**, *39*, 3691–3703.

Chapter 6

Conclusions and future work

6.1 Conclusions

In this thesis, models for the refractive index (RI) were developed for both aerosol with strong absorption bands in the visible region and for aerosol which weakly absorbs light in the visible region. We utilized single particle spectroscopy from optically trapped particles to provide the measurements to construct RI models. In Chapter 2, retrieval algorithms for determining the RI and size of single aerosol particles based on fitting phase functions and fitting the scattering spectra were compared in order to find the most accurate and precise method of RI determination. It was demonstrated that fitting the morphology-dependent resonance (MDR) positions produced more accurate best-fits than fitting phase functions. MDR fitting was then used in subsequent chapters to determine aerosol RI.

All of the wavelength-dependent RI models presented in this thesis used Lorentzian oscillators to describe molecular absorption and model the imaginary part of the RI. The real part of the RI was then determined using the Kramers-Kronig relations. The oscillator model was first used in Chapter 3. Dye-doped beads were trapped in a photophoretic trap and the broadband scattering spectra of the beads was collected. These spectra clearly showed the attenuation of Mie scattering from regions of strong and moderate absorbance. A sum of Lorentzian oscillators, each characterized by three parameters (a constant, B, a center frequency, ν_0 and a full-width-at-half-maximum, Γ), was used to model absorption in the visible region. An offset, n_∞, was used to approximate the core electron transitions in the far-UV. Successful fitting of the scattering spectra allowed both the size and the wavelength-dependent complex RI of these particles to be accurately determined.

Next, in Chapter 4, for weakly absorbing aerosol having no absorption bands in the visible region, the far-UV transitions were modelled with a single, effective oscillator. Complex RIs were determined at a number of relative humidities by heating a trapped particle in a dual-beam optical trap. Using the MDRs, the real part of the RI was determined. Fitting the change in particle size with increasing laser power then provided the imaginary part of the RI at the laser wavelength. It was shown that the complex RI of a solute (e.g. citric acid, NaCl or $(NH_4)_2SO_4$) can be described by a single effective oscillator, characterized by a constant, $\tilde{B}$, a center frequency, $\tilde{\nu_0}$ and its full-width at half-max, $\tilde{\Gamma}$. The RI as a function of both water content and optical frequency was then determined using these oscillator parameters and tabulated literature values for the RI of water. It was also demonstrated that mixing rules allow for the complex RI of ternary solution to be determined.

Finally, in Chapter 5, the RI of a mixture as a function of both water content and optical frequency was described using effective oscillators for individual ions (e.g. SO_4^{2-} and Na^+). The prediction of aerosol RI with ion oscillator parameters is especially useful as characterization of ambient aerosol often produces fractions of ions present. The effect of temperature on the RI in the oscillator model framework was also investigated. The temperature dependence of the oscillator parameters was shown to require only one additional term to damp the oscillator as a function of temperature.

6.2 Future work

Although through this work progress has been made in the prediction of the RI of weakly absorbing aqueous aerosol as a function of solute concentration and wavelength, there is still much work to be done in regards to absorbing aerosol. In Chapter 3, it was shown that the RI of a particle with discrete absorption bands in the visible region can be modeled with a sum of Lorentzian oscillators. However, only a small fraction of ambient aerosol have absorption bands in the visible region similar to the model system studied in Chapter 3.[1,2] In fact, most brown carbon aerosol absorbs strongly in the near-UV with absorbance tailing off into the visible region.[3] This absorption is expected to also be accurately described by an effective Lorentzian oscillator.

Using a medical nebulizer to create brown carbon aerosol and trapping in the photophoretic trap results in particles too small and/or too absorbing to be characterized by MDRs. Alternatively, the imaginary part of the RI of a bulk solution could be determined by UV-vis spectroscopy,[4,5] but the dark colour of aqueous brown carbon aerosol inhibits the retrieval of the real part of the RI with an Abbe refractometer. Spectroscopic ellipsometry can provide both the real and imaginary parts of the RI for thin films, but does not work well for liquid samples as any vibration results in surface waves making accurate measurements impossible without specialized liquid cells. Thus, we have not been able to collect the necessary RI measurements for these aqueous systems for analysis with our oscillator model.

An alternative trapping method to optical trapping is the electrodynamic balance (EDB) which utilizes an electric field to trap a charged particle. Since an EDB does not utilize light

to confine particles, absorbing particles can be readily trapped.[6,7] Bluvshtein *et al.* recently showed the imaginary part of the RI of an absorbing particle held in an EDB can be determined by photophoretic spectroscopy.[6] A combination of photophoretic spectroscopy at a short wavelength and Mie scattering spectroscopy at long wavelengths could be utilized to determine the real and imaginary parts of the RI for brown carbon aerosol. An oscillator model, with oscillators positioned in the near-UV could then be used to model the wavelength-dependent complex RI. Finally, a model for the RI of internally mixed strongly and weakly absorbing aerosol would allow for the prediction of ambient aerosol optical properties.

Another question that requires further investigation is the temperature dependence of the RI. The temperature in the atmosphere varies greatly with altitude (e.g. from 20 °C at Earth's surface to −51 °C at the tropopause).[8] Their small volume allows aqueous aerosol particles to become supercooled in the atmosphere and may remain in the liquid phase until −35 to −40 °C when homogeneous freezing occurs.[9] To accurately predict the RI of ambient aerosol, the effect of temperature must also be considered. The temperature dependence of the RI is usually accounted for with a temperature-dependent solution density,[10] bust since densities are measured for bulk solutions, this method cannot be used over the full range of atmospherically relevant temperatures. In Chapter 5, the temperature dependence of the RI in the effective oscillator framework was included using one additional term to damp the effective oscillator and applied to the examples of sea ice brine and the H_2SO_4-HNO_3-H_2O system.

There are many other possible components to ambient aerosol for which the temperature

dependence over an atmospherically relevant temperature range is still unknown. In the lab, it is difficult to cool single particles as it requires specialized cooling cells that inhibit water vapor deposition on the cell walls and windows. Nevertheless, there are a few examples of single particle experiments that have been performed under low temperatures.[10–12] Single particle experiments to determine the temperature-dependent RI should be performed in order to more fully explore the role of temperature in the effective oscillator model developed in this thesis.

References

[1] Montoya-Aguilera, J.; Horne, J. R.; Hinks, M. L.; Fleming, L. T.; Perraud, V.; Lin, P.; Laskin, A.; Laskin, J.; Dabdub, D.; Nizkorodov, S. A. Secondary organic aerosol from atmospheric photooxidation of indole. *Atmos. Chem. Phys.* **2017**, *17*, 11605–11621.

[2] Lee, H. J.; Aiona, P. K.; Laskin, A.; Laskin, J.; Nizkorodov, S. A. Effect of solar radiation on the optical properties and molecular composition of laboratory proxies of atmospheric brown carbon. *Environ. Sci. Technol.* **2014**, *48*, 10217–10226.

[3] Andersson, A. A Model for the Spectral Dependence of Aerosol Sunlight Absorption. *ACS Earth Space Chem.* **2017**, *1*, 533–539.

[4] Moosmüller, H.; Chakrabarty, R. K.; Ehlers, K. M.; Arnott, W. P. Absorption Ångström coefficient, brown carbon, and aerosols: Basic concepts, bulk matter, and spherical particles. *Atmos. Chem. Phys.* **2011**, *11*, 1217–1225.

[5] Moosmüller, H.; Chakrabarty, R. K.; Arnott, W. P. Aerosol light absorption and its measurement: A review. *J. Quant. Spectrosc. Rad. Transf.* **2009**, *110*, 844–878.

[6] Bluvshtein, N.; Krieger, U. K.; Peter, T. Photophoretic spectroscopy in atmospheric chemistry – high sensitivity measurements of light absorption by a single particle. *Atmos. Meas. Tech.* **2020**, *25*, 1–21.

[7] Price, C. L.; Bain, A.; Wallace, B. J.; Preston, T. C.; Davies, J. F. Simultaneous Retrieval of the Size and Refractive Index of Suspended Droplets in a Linear Quadrupole Electrodynamic Balance. *J. Phys. Chem. A* **2020**, *124*, 1811–1820.

[8] Seinfeld, J. H.; Pandis, S. N. *Atmospheric Chemistry and Physics: From Air Pollution to Climate Change*, 2nd ed.; John Wiley & Sons, Inc.: Hoboken, New Jersey, 2006.

[9] Knopf, D. A.; Alpert, P. A.; Wang, B. The Role of Organic Aerosol in Atmospheric Ice Nucleation: A Review. *ACS Earth Space Chem.* **2018**, *2*, 168–202.

[10] Krieger, U. K.; Mössinger, J. C.; Luo, B.; Weers, U.; Peter, T. Measurement of the refractive indices of H_2SO_4–HNO_3–H_2O solutions to stratospheric temperatures. *Appl. Opt.* **2000**, *39*, 3691.

[11] Suzuki, H.; Matsuzaki, Y.; Muraoka, A.; Tachikawa, M. Raman spectroscopy of optically levitated supercooled water droplet. *J. Chem. Phys.* **2012**, *136*, 234508.

[12] Lu, J. W.; Isenor, M.; Chasovskikh, E.; Stapfer, D.; Signorell, R.; Lu, J. W.; Isenor, M.; Chasovskikh, E.; Stapfer, D.; Signorell, R. Low-temperature Bessel beam trap for single submicrometer aerosol particle studies. *Rev. Sci. Instrum.* **2016**, *85*, 095107.

Appendix A

Supplementary information for Chapter 4

A.1 Introduction

Text A.2 is a detailed procedure of the single particle experiments used here to determine the complex refractive index of aerosol. Text A.3 provides a parameterization of the real part of the refractive index of pure water used in our calculations. Table A.1 lists the complex refractive index of pure water used in our calculations. Figure A.1 shows a schematic of the optical trap, and an example of data collected for an aqueous $(NH_4)_2SO_4$ particle. Tables A.2 to A.6 contain the experimental data shown in Figs. 4.1 and 4.2.

A.2 Experimental

1M solutions were made from one of NaCl (ACP Chemicals Inc.), $(NH_4)_2SO_4$ (Fisher Scientific), citric acid (Fisher Scientific), $MgSO_4$ (Sigma-Aldrich) or NaNO3 (Sigma-Aldrich) dissolved in deionized water. Solutes were all at a minimum of 99.0% purity and no further purification steps were taken. A 1:1 mole ratio NaCl:$NaNO_3$ solution was made by mixing equal volumes of the 1M single solute solutions. Single particles were characterized in a dual-beam optical trap[1] Aerosol particle plumes were generated by a medical nebulizer (Micro-Air, Omron or TurboBOY SX, PARI) and were drawn into the trapping cell. A single particle was trapped at a shared focal point of two counterpropagating laser beams, $\lambda = 0.532$ μm (Opus 532, Laser Quantum). The relative humidity (RH) in the cell was controlled by mixing saturated and dry nitrogen with two mass flow controllers (MF-1, MKS Instruments). The RH and temperature were monitored in the cell using a sensor (SHT75, Sensirion).

Once trapped, a particle was allowed equilibrate with its RH-controlled surroundings. After reaching equilibrium, the particle was heated by changing the laser power; achieved by rotating a half-wave plate (HWP) using a stepper motor with Kinesis software (K10CR1, Thorlabs). The combination of the rotating HWP and a stationary Glan-Taylor polarizer (GTP) allowed us to rapidly change the incident power on the particle while maintaining equal power in both arms of the trap. The power was ramped up from 100 to either 300 or 500 mW. This was achieved by turning the rotating HWP at a constant rate until reaching the final power. The forward and backward Raman scattering from the particle was collected during this heating through one of the trapping objectives (SLMPLN50X, Olympus) and directed into a spectrograph (Isoplane SCT-320, Princeton Instruments) containing a CCD camera (PIXIS:100B_eXcelon, Princeton Instruments). Cavity-enhanced Raman spectroscopy (CERS) spectra were acquired at a rate of 1 spectrum/s while RH and temperatures were measured every 5 seconds. A schematic of the optical trap is shown in Fig. A.1 (a). Peaks from CERS spectra associated with morphology dependent resonances (MDRs) were fitted using MRFIT in order to retrieve the measured radius and real part of the refractive index, n, of the optically trapped droplets.[2] Fig. A.1 (b) and (c) show an exemplary CERS spectrum and the positions of the MDRs with changing power. The refractive index model used during the fitting was a two-term Cauchy expression,

$$n(\nu) = n_0 + n_1\nu^2, \tag{A.1}$$

where n0 and n1 are found with MRFIT. The particle radius was plotted as a function of incident laser power. Following the method outlined by Rafferty & Preston[1] the imaginary part of the refractive index, k at 0.532 μm was determined by minimizing the root mean square error (RMSE) between the experimental and calculated radii over a one-dimensional grid search. Fig. A.1 (d) shows an example of such a fit.

A.3 Refractive index of pure water

For the real part of the refractive index of pure water, $n_{\mathrm{w}}(\lambda)$, we used

$$n_{\mathrm{w}}(\lambda) = \left(1 + \sum_{j=1}^{4} \frac{A_j \lambda^2}{\lambda^2 - \lambda_j^2}\right)^{1/2}, \tag{A.2}$$

where, at 21.5 °C, $A_1 = 0.5689093832$, $A_2 = 0.1719708856$, $A_3 = 0.02062501582$, $A_4 = 0.1123965424$, $\lambda_1^2 = 0.005110301794$, $\lambda_2^2 = 0.01825180155$, $\lambda_3^2 = 0.02624158904$, $\lambda_4^2 = 10.67505178$, and λ is in μm.

For the complex part of the refractive index of pure water, $k_{\mathrm{w}}(\lambda)$, the tabulated data from reference 3 was used. For reference, the values between $\lambda = 0.3$ and 1.0 μm are shown in Table A.1.

Table A.1: Tabulated imaginary refractive index, k, for pure water for wavelengths, λ, spanning 0.3 to 1.0 μm. Data is taken from reference 3.

λ (μm)	k ($\times 10^{-9}$)	λ (μm)	k ($\times 10^{-9}$)	λ (μm)	k ($\times 10^{-9}$)
0.3048	3.826	0.5395	2.098	0.7745	147.8
0.3097	3.546	0.5445	2.269	0.7798	140.9
0.3148	3.325	0.5495	2.442	0.7852	133.9
0.3199	3.190	0.5546	2.659	0.7907	128.2
0.3251	3.082	0.5598	2.869	0.7943	125.8
0.3304	2.984	0.5649	3.132	0.7998	125.0
0.3350	2.883	0.5702	3.434	0.8054	127.0
0.3396	2.766	0.5754	3.844	0.8091	133.0
0.3451	2.653	0.5794	4.434	0.8147	144.8
0.3499	2.528	0.5848	5.221	0.8204	162.1
0.3548	2.420	0.5902	6.365	0.8241	181.9
0.3597	2.316	0.5957	7.723	0.8299	204.1
0.3648	2.217	0.5998	9.634	0.8356	224.3
0.3698	2.117	0.6053	11.32	0.8395	245.9
0.3750	2.031	0.6095	12.38	0.8453	269.0
0.3802	1.940	0.6152	13.30	0.8492	292.9
0.3846	1.840	0.6194	13.99	0.8551	315.3
0.3899	1.761	0.6252	14.72	0.8590	334.8
0.3954	1.663	0.6295	15.02	0.8650	354.6
0.3999	1.580	0.6353	15.52	0.8710	374.8
0.4046	1.489	0.6397	15.70	0.8750	390.7
0.4102	1.422	0.6457	16.06	0.8790	405.3
0.4150	1.339	0.6501	16.74	0.8851	423.4
0.4198	1.258	0.6546	17.77	0.8892	440.3
0.4246	1.169	0.6607	19.40	0.8954	462.2
0.4295	1.088	0.6653	20.31	0.8995	486.2
0.4345	1.018	0.6699	20.98	0.9057	515.0
0.4395	0.9393	0.6745	21.77	0.9099	569.9
0.4446	0.8685	0.6808	23.00	0.9141	669.6
0.4498	0.8087	0.6855	24.71	0.9204	830.4
0.4550	0.7795	0.6902	26.53	0.9247	1060
0.4603	0.7600	0.6950	29.63	0.9290	1368

Table A.1: Continued.

λ (μm)	k ($\times 10^{-9}$)	λ (μm)	k ($\times 10^{-9}$)	λ (μm)	k ($\times 10^{-9}$)
0.4645	0.7495	0.6998	33.48	0.9354	1771
0.4699	0.7291	0.7047	41.00	0.9397	2169
0.4753	0.7011	0.7096	49.98	0.9441	2557
0.4797	0.7092	0.7145	59.95	0.9506	2932
0.4853	0.7158	0.7194	72.91	0.9550	3190
0.4898	0.7342	0.7345	134.8	0.9594	3358
0.4955	0.7849	0.7244	91.37	0.9661	3464
0.5000	0.9243	0.7295	115.0	0.9705	3502
0.5047	1.078	0.7396	145.8	0.9750	3480
0.5105	1.267	0.7447	153.0	0.9795	3418
0.5152	1.461	0.7499	155.9	0.9840	3336
0.5200	1.570	0.7551	158.0	0.9908	3253
0.5248	1.640	0.7603	158.0	0.9954	3131
0.5297	1.757	0.7656	157.0	1.0000	3000
0.5346	1.887	0.7691	152.7		

Table A.2: Tabulated experimental data for the complex refractive index of aqueous NaCl.

RH (%)	k ($\times 10^{-8}$)	n_0	n_1 ($\times 10^{-3} \mu m^2$)
54.9	1.06	1.39244	4.64438
55.0	1.01	1.39255	4.72353
55.0	1.00	1.39235	4.66685
59.3	0.856	1.38859	4.42977
59.5	0.960	1.38811	4.64420
60.1	0.884	1.38934	5.35780
64.1	0.633	1.38343	4.30860
64.2	1.12	1.38281	4.38597
64.3	0.709	1.38263	4.37599
68.8	0.455	1.37774	4.20642
69.0	0.525	1.37782	4.23356
69.1	0.625	1.37779	4.24555
73.4	0.418	1.37098	4.41802
73.6	0.419	1.37106	4.28275
77.8	0.345	1.36643	4.22852
77.9	0.396	1.36577	4.20801
78.1	0.367	1.36565	4.25719

Table A.3: Tabulated experimental data for the complex refractive index of aqueous $NaNO_3$.

RH (%)	k ($\times 10^{-8}$)	n_0	n_1 ($\times 10^{-3} \mu m^2$)
20.4	1.78	1.43293	6.19675
25.2	1.27	1.42804	5.88819
25.3	1.30	1.42803	5.85498
25.3	1.44	1.42792	5.92292
25.4	1.49	1.42792	5.91736
25.4	1.31	1.42789	5.92482
25.5	1.64	1.42779	5.91040
29.8	1.03	1.42281	5.81211
29.9	1.38	1.42295	5.73193
30.5	1.33	1.42405	5.29601
30.6	1.21	1.42420	5.48264
30.7	0.960	1.42420	5.66294
35.2	1.21	1.41876	5.91341
35.4	1.23	1.41883	5.58412
39.1	0.903	1.41363	5.58853
39.3	1.02	1.41337	5.59719
39.5	1.33	1.41384	5.52084
39.6	0.753	1.41457	6.00842
39.7	0.990	1.41386	5.82318
39.9	0.764	1.41393	5.67427
42.8	1.00	1.40892	5.45502
46.8	1.10	1.40418	5.50588
47.0	0.717	1.40397	5.53752
47.3	1.01	1.40386	5.47858
50.1	0.942	1.40233	5.33648
50.2	0.972	1.40239	5.39916
50.3	1.13	1.40208	5.32252
54.4	0.971	1.39782	5.24949
54.5	0.932	1.39778	5.27634
54.6	1.08	1.39775	5.28234
58.9	1.06	1.39406	4.92921
60.7	0.872	1.39102	4.92321
66.6	0.595	1.38346	4.83399

Table A.3: Continued.

RH (%)	k ($\times 10^{-8}$)	n_0	n_1 ($\times 10^{-3} \mu m^2$)
66.6	0.499	1.38328	4.89887
67.1	0.575	1.38339	4.74434
67.4	0.721	1.38316	4.86038
70.9	0.480	1.37720	5.13694
71.1	0.618	1.37740	4.58151
71.8	0.899	1.37581	4.61108
72.8	0.620	1.37426	4.54290
73.1	0.643	1.37320	4.53763
74.9	0.685	1.37083	4.55119
75.3	0.324	1.37005	4.57236
75.4	0.596	1.37008	4.68784
76.1	0.664	1.37107	4.48023
76.4	0.606	1.36897	4.75871
77.6	0.463	1.36691	4.52581

Table A.4: Tabulated experimental data for the complex refractive index of aqueous $(NH_4)_2SO_4$.

RH (%)	k ($\times 10^{-8}$)	n_0	n_1 ($\times 10^{-3} \mu m^2$)
38.5	1.36	1.43281	3.93293
43.3	1.33	1.42871	3.70868
43.6	1.35	1.42799	3.77176
44.2	1.46	1.42761	3.80106
48.3	1.12	1.42375	3.71086
49.1	0.902	1.42529	3.70252
49.1	0.930	1.42525	3.69418
49.3	1.07	1.42526	3.70212
52.8	1.23	1.41926	3.77776
52.8	1.11	1.41906	3.77913
54.1	1.04	1.41965	3.77185
54.3	1.11	1.41948	3.77379
54.4	1.27	1.41969	3.79779
58.7	1.15	1.41280	3.78089
59.5	0.799	1.41354	4.15064
62.9	0.913	1.40846	3.69466
63.0	1.03	1.40813	3.69549
64.5	0.659	1.41003	4.93000
67.3	0.870	1.40305	3.73914
73.6	0.719	1.39801	5.57532
74.6	0.787	1.39740	3.74044
74.7	0.925	1.40009	3.53528
74.8	0.916	1.39981	3.71912
75.1	0.898	1.39971	3.84870
79.1	0.674	1.39457	3.70924
79.3	0.753	1.39416	3.63737
79.5	0.694	1.39427	3.62317
84.0	0.752	1.38883	3.66159

Table A.5: Tabulated experimental data for the complex refractive index of aqueous $MgSO_4$.

RH (%)	k ($\times 10^{-8}$)	n_0	n_1 ($\times 10^{-3} \mu m^2$)
35.7	2.43	1.44919	4.24014
35.9	1.70	1.45237	4.15521
36.1	2.08	1.45022	4.69055
40.0	1.69	1.43852	4.06271
40.1	1.83	1.43823	4.08231
40.1	1.57	1.43830	4.06362
41.2	1.51	1.43595	4.17214
41.4	1.61	1.43598	3.95623
41.4	1.46	1.43611	3.81068
45.0	1.52	1.42836	3.85273
45.2	1.40	1.42761	3.86956
45.4	1.56	1.42781	3.89871
46.5	1.29	1.42593	4.24400
46.9	1.23	1.42590	4.32199
51.8	0.798	1.42013	3.81251
51.8	0.777	1.42003	3.88083
56.3	0.664	1.41347	4.09423
56.8	0.687	1.41407	3.86456
61.0	0.395	1.41121	4.06624
61.2	0.498	1.41103	4.08040
61.4	0.650	1.41012	4.16187
65.0	0.318	1.40631	4.30950
65.3	0.394	1.40615	4.16616
67.1	0.389	1.40697	4.52940
71.2	0.343	1.40282	3.87573
71.5	0.391	1.40327	3.97617
71.6	0.506	1.40265	4.03815
72.0	0.486	1.40327	3.99274
72.1	0.474	1.40317	3.96518
72.7	0.393	1.40241	3.88971
76.5	0.416	1.40009	3.94530
76.6	0.602	1.39841	3.87045
76.6	0.425	1.39989	3.94772

Table A.5: Continued.

RH (%)	k ($\times 10^{-8}$)	n_0	n_1 ($\times 10^{-3} \mu m^2$)
76.6	0.428	1.40020	3.93760
77.9	0.479	1.39866	3.90807
78.1	0.410	1.39822	3.88578
78.6	0.416	1.39731	3.94194
82.3	0.398	1.39531	3.82950
82.5	0.461	1.39423	3.95924
82.9	0.391	1.39452	3.94014
83.2	0.313	1.39414	4.27058
83.3	0.302	1.39424	4.59090
83.5	0.352	1.39358	4.83365
87.3	0.390	1.39014	3.81364
87.6	0.379	1.38979	3.82536
87.9	0.294	1.38966	3.74856
87.9	0.494	1.38857	4.01936
88.6	0.369	1.38858	3.96302

Table A.6: Tabulated experimental data for the complex refractive index of aqueous citric acid.

RH (%)	k ($\times 10^{-8}$)	n_0	n_1 ($\times 10^{-3} \mu m^2$)
38.7	1.44	1.46227	4.39713
39.2	1.89	1.46142	4.40066
42.3	0.968	1.45809	4.46606
42.6	0.772	1.45809	4.46606
44.7	1.16	1.45675	4.48778
44.7	1.21	1.45733	4.48746
44.7	1.04	1.45576	4.49677
49.6	1.21	1.45158	4.32095
49.7	0.870	1.45095	4.38978
50.6	1.12	1.45063	4.29036
55.9	1.28	1.45179	4.55602
56.3	0.795	1.44763	4.12911
57.1	0.932	1.44597	4.14395
60.7	0.731	1.44352	4.41527
61.0	0.487	1.44428	4.45255
61.2	0.681	1.44353	4.34628
61.3	0.666	1.44338	4.23641
61.6	0.652	1.44336	4.06505
66.2	0.561	1.43859	4.07434
67.0	0.560	1.43557	4.18690
71.9	0.536	1.42913	4.42493
73.2	0.685	1.42974	4.13484
76.8	0.820	1.42785	4.14202
77.6	0.460	1.42154	4.23119
83.1	0.303	1.40795	4.00893
83.8	0.540	1.40649	4.54022
84.9	0.173	1.39644	3.92342
85.4	0.238	1.39648	3.92323
85.9	0.346	1.39487	4.92876

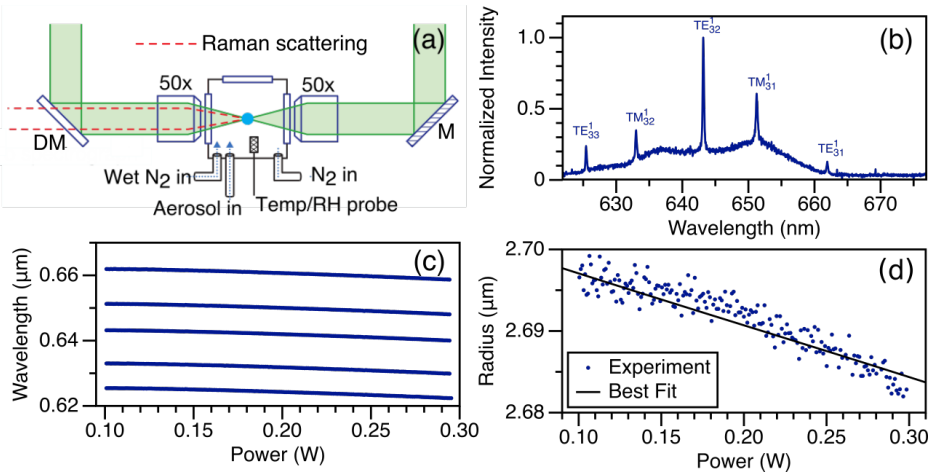

Figure A.1: (a) Schematic of the dual-beam optical trap. Laser light (green) is directed with a mirror (M) and dichroic mirror (DM) and focused into the trapping cell through two 50x objective. Raman scattering is collected through one of the 50x objectives and is directed to the spectrograph through the DM (b) CERS spectrum of an optically trapped $(NH_4)_2SO_4$ particle at $71.2 \pm 1.8\%$ RH and 100 mW trapping power. MDRs have been labeled with their mode assignments X_z^y where X is the mode polarization, y is the mode order and z is the mode number. (c) MDR positions for the $(NH_4)_2SO_4$ particle over a power ramp to 300 mW. (d) Experimental radius with power for the $(NH_4)_2SO_4$ particle and best fit for k.

References

[1] Rafferty, A.; Preston, T. C. Measuring the size and complex refractive index of an aqueous aerosol particle using electromagnetic heating and cavity-enhanced Raman scattering. *Phys. Chem. Chem. Phys.* **2018**, *20*, 17038–17047.

[2] Preston, T. C.; Reid, J. P. Determining the size and refractive index of microspheres using the mode assignments from Mie resonances. *J. Opt. Soc. Am. A* **2015**, *32*, 2210–2217.

[3] Segelstein, D. J. The complex refractive index of water (M.Sc. Thesis, University of Missouri). 1981.

Appendix B

Supplementary information for Chapter 5

B.1 Experimental

The following solutes were used with no further purification: Sucrose (Fisher Chemical), tartaric acid (BDH Inc.), D-mannose (Sigma Aldrich), citric acid (Fisher Chemical), NaCl (ACP Chemicals Inc.), $(NH_4)_2SO_4$ (Fisher Chemical), $NaNO_3$ (Sigma Aldrich), $MgSO_4$ (Sigma Aldrich), $NaHSO_4$ (anhydrous, $>$ 95% pure Sigma Aldrich), NaBr (ACP Chemicals Inc.), KBr (Sigma Aldrich), LiCl (MP Biomedicals, LLC), KCl (ACP Chemicals Inc.), Na_2SO_4 (Fisher Chemical), $CaCl_2$ (anhydrous, Fisher Chemical), NH_4Cl (ACP Chemicals Inc.), and $MgCl_2$ (Fisher Chemical). Solutes were dissolved in deionized water to make aqueous solutions. Concentration of the solution depended on the solute but ranged from 0.5 – 2 M. 1:1 by mole $MgSO_4$:$MgCl_2$ was made using the same solutes mentioned above, with each at a concentration of 1M in deionized water. Solutions were nebulized with a medical nebulizer (Micro-Air, Omron or TurboBOY SX, PARI) and drawn into the trapping cell.

Two different optical setups were used in these experiments, optical tweezers and a dual-beam optical trap (Fig. B.1). The optical setups for the optical tweezers[1] and the dual-beam optical trap[2] have both been previously reported.

The optical tweezers are formed using a $\lambda = 532$ nm laser (Laser Quantum Opus 532) that is focused into a trapping cell with a 100$\times$ oil immersion objective (Olympus PLN 100$\times$, NA = 1.25). Depending on their size, particles were trapped and held with laser powers from 5 – 30 mW. Elastic back scattering from a broadband light source (Ocean Optics HL-2000) introduced through the trapping objective is collected back through the same objective and directed towards a spectrometer (Princeton Instruments Isoplane 320) and CCD (Princeton

Instruments PIXIS 100). Spectra were collected from 550 – 800 nm with a 1200 groove/mm diffraction grating in five steps using the step & glue function in Princeton Instruments' LightField software. In this way, we are able to obtain high resolution spectra over a broad spectral range.

The dual-beam optical trap also uses a $\lambda = 532$ nm laser (Laser Quantum Opus 532) which is split along two beam paths with a polarizing beam splitter. The two beams are focus into the trapping cell with 50× long working distance objective lenses (Olympus SLM-PLN50X). The two co-axial objective lenses are aligned so that they share a common focal point. Particles were trapped with 100 mW total laser power. The forward and backward Raman scattering from the trapped particle was collected through one of the trapping objectives and directed into the spectrograph (Princeton Instruments Isoplane 320) and CCD (Princeton Instruments PIXIS 100). Cavity-enhanced Raman scattering (CERS) spectra were collected over the spontaneous Raman band of water with a 1200 groove/mm grating.

The relative humidity (RH) in either of the cells is adjusted using two mass flow controllers (MKS Instruments MF-1); mixing dry and saturated nitrogen. Air flow rates through the cell were typically between 30 – 50 sccm for the optical tweezers and 100 sccm for the dual-beam optical trap. Temperature and RH were measured in the trapping cell close to the trapped particle with a sensor (SHT75 Sensirion).

After becoming trapped, the aerosol particle was allowed to come to equilibrium with its RH-controlled surroundings. Once in equilibrium, five broadband scattering or CERS spectra were collected at constant RH. The RH in the cell was then adjusted and the particle was allowed equilibrate once again. In this way, broadband scattering and CERS spectra were

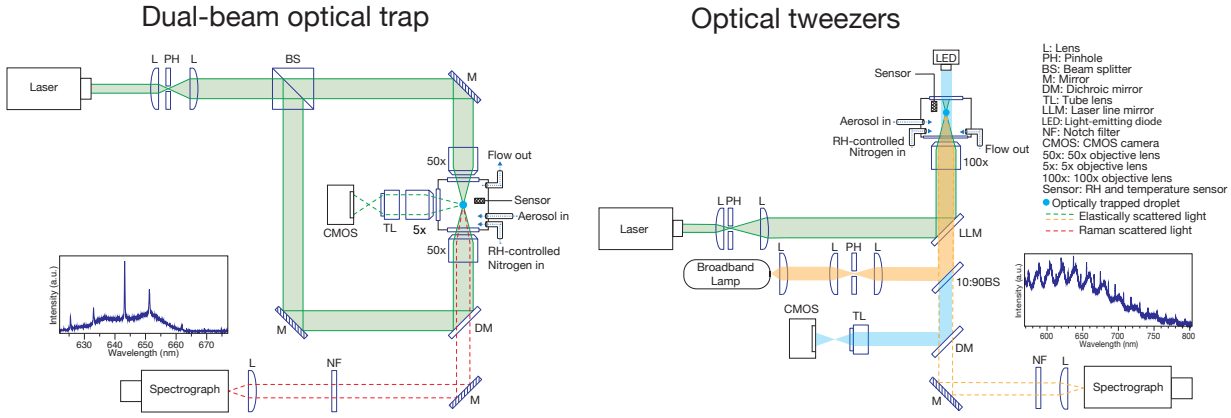

Figure B.1: Optical setups for dual-beam optical trap with CERS collection and optical tweezers with broadband Mie scattering collection. Sample spectra are shown as insets.

collected for each particle over a wide range of RHs.

Solutes that undergo efflorescence were measured until just above the efflorescence point and solutes that do not undergo efflorescence were measured down to RHs of about 20%.

For measurements taken in the optical tweezers, a background spectrum was taken by collecting the broadband light reflected off the coverslip after releasing the particle from the trap. This background spectrum was divided out of the scattering spectra in order to remove the background intensity. No background correction is required for CERS measurements.

B.2 Data fitting

Features in the broadband scattering and CERS spectra associated with morphology dependant resonances were used to determine the refractive index (RI) of the particle using the freely available software MRFIT.[3] These resonances can be observed in exemplary CERS and broadband Mie scattering spectra inset in Fig. B.1. The RI was fitted as a function of

wavenumber, ν, using a Cauchy expression of the form:

$$n(\nu) = n_0 + n_1\nu^2 + n_2\nu^4, \tag{B.1}$$

where $n(\nu)$ is the real part of the RI, n_0, n_1, and n_2 are found with MRFIT and $\nu = 1/\lambda$ where λ is the wavelength of light. Broadband scattering spectra were fit with all three terms while CERS spectra were fit with only two terms.

To determine the oscillator parameters for the organic and inorganic solutes we follow the procedure outlined by Bain *et al.*[4] For an aqueous solution, the real part of the RI is

$$n(\nu) = 1 + \sum_{\alpha=1}^{J} \phi_\alpha \frac{2}{\pi} \frac{\tilde{B}_\alpha \tilde{\nu}_{0,\alpha}}{\tilde{\nu}_{0,\alpha}^2 - \nu^2} + \phi_{\mathrm{w}}(n^{(\mathrm{w})}(\nu) - 1), \tag{B.2}$$

where J is the number of solutes, $n^{(\mathrm{w})}(\nu)$ is the RI of pure water (taken from Ref.5), and ϕ_α and ϕ_w are set to be the mass fractions of solute α and water, respectively. Each solute α is characterized by a resonant wavenumber $\tilde{\nu}_{0,\alpha}$ and constant $\tilde{B}_\alpha$. By fitting experimentally measured RIs as a function of aerosol water content with Eq. 5.1 we can determine the effective oscillator parameters for each solute. As noted in the main text, Eq. B.2 differs from the equation presented in Ref. 4 as ϕ_α and ϕ_w are mass fractions rather than relative densities. This change makes calculations much simpler as density functions are no longer required (often these functions are not known). For the aqueous systems studied here, this was found to be an excellent approximation since solution density is almost linear with solute mass fraction.

After fitting oscillator parameters for binary aqueous solutions (one solute + water, where the one solute would be, for example, NaCl), effective oscillator parameters for individual ions were subsequently determined for inorganic species by splitting each solute into contributions from anions and cations. We generated a list of equations where the RI of the solute from the solute effective oscillator parameters is equal to the RI from the ion effective oscillator parameters. As we have already found the solute effective oscillator parameters, the only unknowns were the effective oscillator parameters for the individual ions in the resulting system of equations. In our measured dataset, a number of the ions are present in more than one solute. We solved this system of equations using the `NMinimize` function in the off-the-shelf software Mathematica and simultaneously found effective oscillator parameters for 11 ions listed in Table 5.1 in the main text (H^+ has no core electrons so it was assumed that $\tilde{B}_{H^+}$ and $\tilde{\nu}_{0,H^+}$ were both equal to zero).

B.3 Comparing refractive index calculations

The percent difference between the effective oscillator predictions and parameterizations or models from Bain, Rafferty and Preston[4] Millard and Seaver,[6] and Cotterell *et al.*[7] for aqueous NaCl across the range of water activities shown in Fig. 5.2 were calculated using the following equation:

$$\text{Percent Difference} = \frac{n(\lambda)_{\text{lit}} - n(\lambda)_{\text{osc}}}{(n(\lambda)_{\text{lit}} + n(\lambda)_{\text{osc}})/2} \times 100\% \tag{B.3}$$

where subscripts ‘lit’ and ‘osc’ refer to the RI from a model or parameterization from the literature and the oscillator model, respectively. The percent difference is plotted as a function of wavelength for several water activities in Fig. B.2.

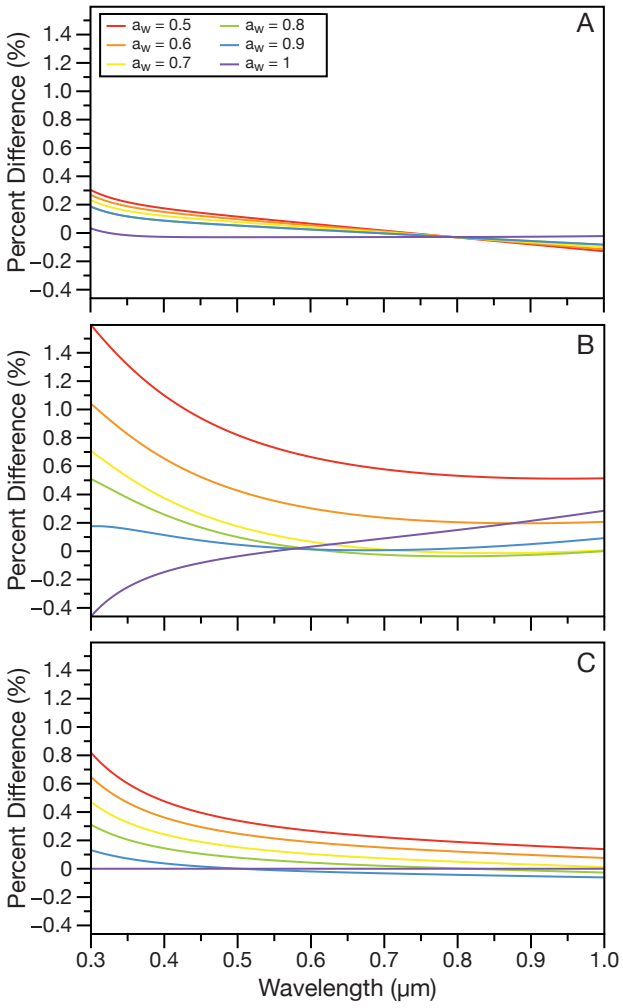

Figure B.2: Percent differences between the oscillator model used here and models or parameterizations from A) Millard and Seaver[6] B) Cotterell *et al.*[7] and C) Bain, Rafferty and Preston[4] for NaCl at a range of water activities.

References

[1] Lew, L. J. N.; Ting, M. V.; Preston, T. C. Determining the size and refractive index of homogeneous spherical aerosol particles using Mie resonance spectroscopy. *Appl. Opt.* **2018**, *57*, 4601–4609.

[2] Rafferty, A.; Preston, T. C. Measuring the size and complex refractive index of an aqueous aerosol particle using electromagnetic heating and cavity-enhanced Raman scattering. *Phys. Chem. Chem. Phys.* **2018**, *20*, 17038–17047.

[3] Mie Resonance Fitting (MRFIT). http://www.meteo.mcgill.ca/~tpreston/code.html.

[4] Bain, A.; Rafferty, A.; Preston, T. C. The Wavelength-Dependent Complex Refractive Index of Hygroscopic Aerosol Particles and Other Aqueous Media: An Effective Oscillator Model. *Geophys. Res. Lett.* **2019**, *46*, 10636–10645.

[5] Daimon, M.; Masumura, A. Measurement of the refractive index of distilled water from the near-infrared region to the ultraviolet region. *Appl. Opt.* **2007**, *46*, 3811–3820.

[6] Millard, R.; Seaver, G. An index of refraction algorithm for seawater over temperature, pressure, salinity, density, and wavelength. *Deep Sea Res. Part 1 Oceanogr. Res. Pap.* **1990**, *37*, 1909–1926.

[7] Cotterell, M. I.; Willoughby, R. E.; Bzdek, B. R.; Orr-Ewing, A. J.; Reid, J. P. A complete parameterisation of the relative humidity and wavelength dependence of the refractive index of hygroscopic inorganic aerosol particles. *Atmos. Chem. Phys.* **2017**, *17*, 9837–9851.

Water Uptake and Hygroscopic Growth of Organosulfate Aerosol

Author: Armando D. Estillore, Anusha P. S. Hettiyadura, Zhen Qin, et al

Publication: Environmental Science & Technology

Publisher: American Chemical Society

Date: Apr 1, 2016

Quick Price Estimate

This service provides permission for reuse only. If you do not have a copy of the portion you are using, you may copy and paste the content and reuse according to the terms of your agreement. Please be advised that obtaining the content you license is a separate transaction not involving RightsLink.

If credit is given to another source for the material you requested from RightsLink, permission must be obtained from that source.

Note: Individual Scheme and Structure reuse is free of charge and does not require a license. If the scheme or structure is identified as a "Figure" in the article, permission is required.

Permission for this particular request is granted for print and electronic formats, and translations, at no charge. Figures and tables may be modified. Appropriate credit should be given. Please print this page for your records and provide a copy to your publisher. Requests for up to 4 figures require only this record. Five or more figures will generate a printout of additional terms and conditions. Appropriate credit should read: "Reprinted with permission from {COMPLETE REFERENCE CITATION}. Copyright {YEAR} American Chemical Society." Insert appropriate information in place of the capitalized words.

If credit is given to another source for the material you requested, permission must be obtained from that source.

I would like to...	reuse in a Thesis/Dissertation	Format	Electronic
Requestor Type	Non-profit	Select your currency	CAD - $
Portion	Table/Figure/Micrograph	Quick Price	Click Quick Price
Number of Table/Figure/Micrograph	1		

QUICK PRICE CONTINUE

To request permission for a type of use not listed, please contact the publisher directly.

Copyright Clearance Center Marketplace™

Royal Society of Chemistry - License Terms and Conditions

This is a License Agreement between Alison Bain ("You") and Royal Society of Chemistry ("Publisher") provided by Copyright Clearance Center ("CCC"). The license consists of your order details, the terms and conditions provided by Royal Society of Chemistry, and the CCC terms and conditions.

All payments must be made in full to CCC.

Order Date	24-Jan-2021	**Type of Use**	Republish in a thesis/dissertation
Order license ID	1092594-1		
ISSN	1463-9084	**Publisher**	ROYAL SOCIETY OF CHEMISTRY
		Portion	Chart/graph/table/figure

LICENSED CONTENT

Publication Title	Physical chemistry chemical physics	**Country**	United Kingdom of Great Britain and Northern Ireland
Author/Editor	Royal Society of Chemistry (Great Britain)	**Rightsholder**	Royal Society of Chemistry
Date	01/01/1999	**Publication Type**	e-Journal
Language	English	**URL**	http://firstsearch.oclc.org/journal=1463-9076;screen=info;ECOIP

REQUEST DETAILS

Portion Type	Chart/graph/table/figure	**Distribution**	Canada
Number of charts / graphs / tables / figures requested	1	**Translation**	Original language of publication
		Copies for the disabled?	No
Format (select all that apply)	Electronic	**Minor editing privileges?**	Yes
Who will republish the content?	Academic institution	**Incidental promotional use?**	No
Duration of Use	Life of current edition	**Currency**	CAD
Lifetime Unit Quantity	Up to 499		
Rights Requested	Main product		

NEW WORK DETAILS

Title	The refractive index of single aerosol particles: Measurements and models	**Institution name**	McGill University
		Expected presentation date	2021-04-30
Instructor name	Alison Bain		

ADDITIONAL DETAILS

Order reference number	N/A	**The requesting person / organization to appear on the license**	Alison Bain

REUSE CONTENT DETAILS

Title, description or numeric reference of the portion(s)	Figure 11 - Comparison of the Raman spectrum (red line, bottom) from an aqueous EAN droplet, and the broadband Mie scattering spectrum (blue line, top)	**Title of the article/chapter the portion is from**	Optical trapping and spectroscopic characterisation of ionic liquid solutions
		Author of portion(s)	Lee J. Moore, Michael D. Summers and Grant A. D. Ritchie
Editor of portion(s)	N/A	**Issue, if republishing an article from a serial**	N/A
Volume of serial or monograph	15		
Page or page range of portion	13497	**Publication date of portion**	2013-06-25

CCC Republication Terms and Conditions

1. Description of Service; Defined Terms. This Republication License enables the User to obtain licenses for republication of one or more copyrighted works as described in detail on the relevant Order Confirmation (the "Work(s)"). Copyright Clearance Center, Inc. ("CCC") grants licenses through the Service on behalf of the rightsholder identified on the Order Confirmation (the "Rightsholder"). "Republication", as used herein, generally means the inclusion of a Work, in whole or in part, in a new work or works, also as described on the Order Confirmation. "User", as used herein, means the person or entity making such republication.

2. The terms set forth in the relevant Order Confirmation, and any terms set by the Rightsholder with respect to a particular Work, govern the terms of use of Works in connection with the Service. By using the Service, the person transacting for a republication license on behalf of the User represents and warrants that he/she/it (a) has been duly authorized by the User to accept, and hereby does accept, all such terms and conditions on behalf of User, and (b) shall inform User of all such terms and conditions. In the event such person is a "freelancer" or other third party independent of User and CCC, such party shall be deemed jointly a "User" for purposes of these terms and conditions. In any event, User shall be deemed to have accepted and agreed to all such terms and conditions if User republishes the Work in any fashion.

3. Scope of License; Limitations and Obligations.

    3.1. All Works and all rights therein, including copyright rights, remain the sole and exclusive property of the Rightsholder. The license created by the exchange of an Order Confirmation (and/or any invoice) and payment by User of the full amount set forth on that document includes only those rights expressly set forth in the Order Confirmation and in these terms and conditions, and conveys no other rights in the Work(s) to User. All rights not expressly granted are hereby reserved.

    3.2. General Payment Terms: You may pay by credit card or through an account with us payable at the end of the month. If you and we agree that you may establish a standing account with CCC, then the following terms apply: Remit Payment to: Copyright Clearance Center, 29118 Network Place, Chicago, IL 60673-1291. Payments Due: Invoices are payable upon their delivery to you (or upon our notice to you that they are available to you for downloading). After 30 days, outstanding amounts will be subject to a service charge of 1-1/2% per month or, if less, the maximum rate allowed by applicable law. Unless otherwise specifically set forth in the Order Confirmation or in a separate written agreement signed by CCC, invoices are due and payable on "net 30" terms. While User may exercise the rights licensed immediately upon issuance of the Order Confirmation, the license is automatically revoked and is null and void, as if it had never been

issued, if complete payment for the license is not received on a timely basis either from User directly or through a payment agent, such as a credit card company.

3.3. Unless otherwise provided in the Order Confirmation, any grant of rights to User (i) is "one-time" (including the editions and product family specified in the license), (ii) is non-exclusive and non-transferable and (iii) is subject to any and all limitations and restrictions (such as, but not limited to, limitations on duration of use or circulation) included in the Order Confirmation or invoice and/or in these terms and conditions. Upon completion of the licensed use, User shall either secure a new permission for further use of the Work(s) or immediately cease any new use of the Work(s) and shall render inaccessible (such as by deleting or by removing or severing links or other locators) any further copies of the Work (except for copies printed on paper in accordance with this license and still in User's stock at the end of such period).

3.4. In the event that the material for which a republication license is sought includes third party materials (such as photographs, illustrations, graphs, inserts and similar materials) which are identified in such material as having been used by permission, User is responsible for identifying, and seeking separate licenses (under this Service or otherwise) for, any of such third party materials; without a separate license, such third party materials may not be used.

3.5. Use of proper copyright notice for a Work is required as a condition of any license granted under the Service. Unless otherwise provided in the Order Confirmation, a proper copyright notice will read substantially as follows: "Republished with permission of [Rightsholder's name], from [Work's title, author, volume, edition number and year of copyright]; permission conveyed through Copyright Clearance Center, Inc. " Such notice must be provided in a reasonably legible font size and must be placed either immediately adjacent to the Work as used (for example, as part of a by-line or footnote but not as a separate electronic link) or in the place where substantially all other credits or notices for the new work containing the republished Work are located. Failure to include the required notice results in loss to the Rightsholder and CCC, and the User shall be liable to pay liquidated damages for each such failure equal to twice the use fee specified in the Order Confirmation, in addition to the use fee itself and any other fees and charges specified.

3.6. User may only make alterations to the Work if and as expressly set forth in the Order Confirmation. No Work may be used in any way that is defamatory, violates the rights of third parties (including such third parties' rights of copyright, privacy, publicity, or other tangible or intangible property), or is otherwise illegal, sexually explicit or obscene. In addition, User may not conjoin a Work with any other material that may result in damage to the reputation of the Rightsholder. User agrees to inform CCC if it becomes aware of any infringement of any rights in a Work and to cooperate with any reasonable request of CCC or the Rightsholder in connection therewith.

4. Indemnity. User hereby indemnifies and agrees to defend the Rightsholder and CCC, and their respective employees and directors, against all claims, liability, damages, costs and expenses, including legal fees and expenses, arising out of any use of a Work beyond the scope of the rights granted herein, or any use of a Work which has been altered in any unauthorized way by User, including claims of defamation or infringement of rights of copyright, publicity, privacy or other tangible or intangible property.

5. Limitation of Liability. UNDER NO CIRCUMSTANCES WILL CCC OR THE RIGHTSHOLDER BE LIABLE FOR ANY DIRECT, INDIRECT, CONSEQUENTIAL OR INCIDENTAL DAMAGES (INCLUDING WITHOUT LIMITATION DAMAGES FOR LOSS OF BUSINESS PROFITS OR INFORMATION, OR FOR BUSINESS INTERRUPTION) ARISING OUT OF THE USE OR INABILITY TO USE A WORK, EVEN IF ONE OF THEM HAS BEEN ADVISED OF THE POSSIBILITY OF SUCH DAMAGES. In any event, the total liability of the Rightsholder and CCC (including their respective employees and directors) shall not exceed the total amount actually paid by User for this license. User assumes full liability for the actions and omissions of its principals, employees, agents, affiliates, successors and assigns.

6. Limited Warranties. THE WORK(S) AND RIGHT(S) ARE PROVIDED "AS IS". CCC HAS THE RIGHT TO GRANT TO USER THE RIGHTS GRANTED IN THE ORDER CONFIRMATION DOCUMENT. CCC AND THE RIGHTSHOLDER DISCLAIM ALL OTHER WARRANTIES RELATING TO THE WORK(S) AND RIGHT(S), EITHER EXPRESS OR IMPLIED, INCLUDING

WITHOUT LIMITATION IMPLIED WARRANTIES OF MERCHANTABILITY OR FITNESS FOR A PARTICULAR PURPOSE. ADDITIONAL RIGHTS MAY BE REQUIRED TO USE ILLUSTRATIONS, GRAPHS, PHOTOGRAPHS, ABSTRACTS, INSERTS OR OTHER PORTIONS OF THE WORK (AS OPPOSED TO THE ENTIRE WORK) IN A MANNER CONTEMPLATED BY USER; USER UNDERSTANDS AND AGREES THAT NEITHER CCC NOR THE RIGHTSHOLDER MAY HAVE SUCH ADDITIONAL RIGHTS TO GRANT.

7. Effect of Breach. Any failure by User to pay any amount when due, or any use by User of a Work beyond the scope of the license set forth in the Order Confirmation and/or these terms and conditions, shall be a material breach of the license created by the Order Confirmation and these terms and conditions. Any breach not cured within 30 days of written notice thereof shall result in immediate termination of such license without further notice. Any unauthorized (but licensable) use of a Work that is terminated immediately upon notice thereof may be liquidated by payment of the Rightsholder's ordinary license price therefor; any unauthorized (and unlicensable) use that is not terminated immediately for any reason (including, for example, because materials containing the Work cannot reasonably be recalled) will be subject to all remedies available at law or in equity, but in no event to a payment of less than three times the Rightsholder's ordinary license price for the most closely analogous licensable use plus Rightsholder's and/or CCC's costs and expenses incurred in collecting such payment.

8. Miscellaneous.

    8.1. User acknowledges that CCC may, from time to time, make changes or additions to the Service or to these terms and conditions, and CCC reserves the right to send notice to the User by electronic mail or otherwise for the purposes of notifying User of such changes or additions; provided that any such changes or additions shall not apply to permissions already secured and paid for.

    8.2. Use of User-related information collected through the Service is governed by CCC's privacy policy, available online here:https://marketplace.copyright.com/rs-ui-web/mp/privacy-policy

    8.3. The licensing transaction described in the Order Confirmation is personal to User. Therefore, User may not assign or transfer to any other person (whether a natural person or an organization of any kind) the license created by the Order Confirmation and these terms and conditions or any rights granted hereunder; provided, however, that User may assign such license in its entirety on written notice to CCC in the event of a transfer of all or substantially all of User's rights in the new material which includes the Work(s) licensed under this Service.

    8.4. No amendment or waiver of any terms is binding unless set forth in writing and signed by the parties. The Rightsholder and CCC hereby object to any terms contained in any writing prepared by the User or its principals, employees, agents or affiliates and purporting to govern or otherwise relate to the licensing transaction described in the Order Confirmation, which terms are in any way inconsistent with any terms set forth in the Order Confirmation and/or in these terms and conditions or CCC's standard operating procedures, whether such writing is prepared prior to, simultaneously with or subsequent to the Order Confirmation, and whether such writing appears on a copy of the Order Confirmation or in a separate instrument.

    8.5. The licensing transaction described in the Order Confirmation document shall be governed by and construed under the law of the State of New York, USA, without regard to the principles thereof of conflicts of law. Any case, controversy, suit, action, or proceeding arising out of, in connection with, or related to such licensing transaction shall be brought, at CCC's sole discretion, in any federal or state court located in the County of New York, State of New York, USA, or in any federal or state court whose geographical jurisdiction covers the location of the Rightsholder set forth in the Order Confirmation. The parties expressly submit to the personal jurisdiction and venue of each such federal or state court.If you have any comments or questions about the Service or Copyright Clearance Center, please contact us at 978-750-8400 or send an e-mail to support@copyright.com.

v 1.1

Re: Permission Request Form [#483]

Gumbel, Erin <egumbel@ametsoc.org>
Wed 1/27/2021 1:41 PM

To: Alison Bain <alison.bain@mail.mcgill.ca>
Cc: permissions <permissions@ametsoc.org>

Dear Alison,

Thank you for your email. This signed message constitutes permission to use the material requested below.

You may include Figure 1 from Erlick, Abbatt, and Rudich's 2011 JAS article in your McGill dissertation with the following conditions:

1. Include the complete bibliographic citation of the original source.
2. Include the following statement with that citation: **© American Meteorological Society. Used with permission.**

Congratulations on nearing completion of your dissertation! If you have any questions or need additional information, please feel free to contact me.

Please note: If the material in an AMS journal is credited to another source, the requester must obtain permission or license from that source directly. That material may not be used without permission or license from the copyright holder.

Best,

Ms. Erin Gumbel, she/her/hers
Senior Peer Review Support Associate
Senior Permissions Specialist
egumbel@ametsoc.org
617-226-3926

On Sun, Jan 24, 2021 at 10:33 AM Wufoo <no-reply@wufoo.com> wrote:

Use requested (examples include: reuse in a thesis/dissertation, journal, book, or coursepack materials; translation; inclusion in an institutional repository, etc) *	thesis/dissertation
Journal *	Journal of the Atmospheric Sciences
Title of AMS journal article *	How different calculations of the refractive index affect estimates of the radiative forcing efficiency of ammonium sulfate aerosols

First author of AMS journal article *	Carynelisa Erlick
Year of Publication *	2011
If you are requesting permission to reuse figures/images: List the figure number, caption, and the page(s) on which the material appears.	FIG. 1. Real part of the refractive index at 0.633-um wavelength of a solution of AS with water as a function of the weight percentage of AS... page 1846
Requester name *	Alison Bain
Requester Email *	alison.bain@mail.mcgill.ca
Requester type *	Academic/Non-Commercial
Title of new work *	The refractive index of single aerosol particles: Measurements and models
Format *	Electronic
Are you requesting permission for language(s) other than English? *	No

JOHN WILEY AND SONS LICENSE
TERMS AND CONDITIONS

Jan 24, 2021

This Agreement between Ms. Alison Bain ("You") and John Wiley and Sons ("John Wiley and Sons") consists of your license details and the terms and conditions provided by John Wiley and Sons and Copyright Clearance Center.

License Number	4995370586105
License date	Jan 24, 2021
Licensed Content Publisher	John Wiley and Sons
Licensed Content Publication	Geophysical Research Letters
Licensed Content Title	The Wavelength−Dependent Complex Refractive Index of Hygroscopic Aerosol Particles and Other Aqueous Media: An Effective Oscillator Model
Licensed Content Author	Thomas C. Preston, Aidan Rafferty, Alison Bain
Licensed Content Date	Sep 6, 2019
Licensed Content Volume	46
Licensed Content Issue	17-18

Licensed Content Pages	10
Type of use	Dissertation/Thesis
Requestor type	Author of this Wiley article
Format	Electronic
Portion	Full article
Will you be translating?	No
Title	The refractive index of single aerosol particles: Measurements and models
Institution name	McGill University
Expected presentation date	Mar 2021
Order reference number	4883100196101
Requestor Location	Ms. Alison Bain 1375 Rue la Fontaine 34 Montreal, QC H2L 1T6 Canada Attn: Ms. Alison Bain
Publisher Tax ID	EU826007151
Total	0.00 CAD

Terms and Conditions

TERMS AND CONDITIONS

This copyrighted material is owned by or exclusively licensed to John Wiley & Sons, Inc. or one of its group companies (each a"Wiley Company") or handled on behalf of a society with which a Wiley Company has exclusive publishing rights in relation to a particular work (collectively "WILEY"). By clicking "accept" in connection with completing this licensing transaction, you agree that the following terms and conditions apply to this transaction (along with the billing and payment terms and conditions established by the Copyright Clearance Center Inc., ("CCC's Billing and Payment terms and conditions"), at the time that you opened your RightsLink account (these are available at any time at http://myaccount.copyright.com).

Terms and Conditions

- The materials you have requested permission to reproduce or reuse (the "Wiley Materials") are protected by copyright.

- You are hereby granted a personal, non-exclusive, non-sub licensable (on a stand-alone basis), non-transferable, worldwide, limited license to reproduce the Wiley Materials for the purpose specified in the licensing process. This license, **and any CONTENT (PDF or image file) purchased as part of your order,** is for a one-time use only and limited to any maximum distribution number specified in the license. The first instance of republication or reuse granted by this license must be completed within two years of the date of the grant of this license (although copies prepared before the end date may be distributed thereafter). The Wiley Materials shall not be used in any other manner or for any other purpose, beyond what is granted in the license. Permission is granted subject to an appropriate acknowledgement given to the author, title of the material/book/journal and the publisher. You shall also duplicate the copyright notice that appears in the Wiley publication in your use of the Wiley Material. Permission is also granted on the understanding that nowhere in the text is a previously published source acknowledged for all or part of this Wiley Material. Any third party content is expressly excluded from this permission.

- With respect to the Wiley Materials, all rights are reserved. Except as expressly granted by the terms of the license, no part of the Wiley Materials may be copied, modified, adapted (except for minor reformatting required by the new Publication), translated, reproduced, transferred or distributed, in any form or by any means, and no derivative works may be made based on the Wiley Materials without the prior permission of the respective copyright owner.**For STM Signatory Publishers clearing permission under the terms of the STM Permissions Guidelines only, the terms of the license are extended to include subsequent editions and for editions in other languages, provided such editions are for the work as a whole in situ and does not involve the separate exploitation of the permitted figures or extracts,** You may not alter, remove or suppress in any manner any copyright, trademark or other notices displayed by the Wiley Materials. You may not license, rent, sell, loan, lease, pledge, offer as security, transfer or assign the Wiley Materials on a stand-alone basis, or any of the rights granted to you hereunder to any other person.

- The Wiley Materials and all of the intellectual property rights therein shall at all times remain the exclusive property of John Wiley & Sons Inc, the Wiley Companies, or their respective licensors, and your interest therein is only that of having possession of and the right to reproduce the Wiley Materials pursuant to Section 2 herein during the

continuance of this Agreement. You agree that you own no right, title or interest in or to the Wiley Materials or any of the intellectual property rights therein. You shall have no rights hereunder other than the license as provided for above in Section 2. No right, license or interest to any trademark, trade name, service mark or other branding ("Marks") of WILEY or its licensors is granted hereunder, and you agree that you shall not assert any such right, license or interest with respect thereto

- NEITHER WILEY NOR ITS LICENSORS MAKES ANY WARRANTY OR REPRESENTATION OF ANY KIND TO YOU OR ANY THIRD PARTY, EXPRESS, IMPLIED OR STATUTORY, WITH RESPECT TO THE MATERIALS OR THE ACCURACY OF ANY INFORMATION CONTAINED IN THE MATERIALS, INCLUDING, WITHOUT LIMITATION, ANY IMPLIED WARRANTY OF MERCHANTABILITY, ACCURACY, SATISFACTORY QUALITY, FITNESS FOR A PARTICULAR PURPOSE, USABILITY, INTEGRATION OR NON-INFRINGEMENT AND ALL SUCH WARRANTIES ARE HEREBY EXCLUDED BY WILEY AND ITS LICENSORS AND WAIVED BY YOU.

- WILEY shall have the right to terminate this Agreement immediately upon breach of this Agreement by you.

- You shall indemnify, defend and hold harmless WILEY, its Licensors and their respective directors, officers, agents and employees, from and against any actual or threatened claims, demands, causes of action or proceedings arising from any breach of this Agreement by you.

- IN NO EVENT SHALL WILEY OR ITS LICENSORS BE LIABLE TO YOU OR ANY OTHER PARTY OR ANY OTHER PERSON OR ENTITY FOR ANY SPECIAL, CONSEQUENTIAL, INCIDENTAL, INDIRECT, EXEMPLARY OR PUNITIVE DAMAGES, HOWEVER CAUSED, ARISING OUT OF OR IN CONNECTION WITH THE DOWNLOADING, PROVISIONING, VIEWING OR USE OF THE MATERIALS REGARDLESS OF THE FORM OF ACTION, WHETHER FOR BREACH OF CONTRACT, BREACH OF WARRANTY, TORT, NEGLIGENCE, INFRINGEMENT OR OTHERWISE (INCLUDING, WITHOUT LIMITATION, DAMAGES BASED ON LOSS OF PROFITS, DATA, FILES, USE, BUSINESS OPPORTUNITY OR CLAIMS OF THIRD PARTIES), AND WHETHER OR NOT THE PARTY HAS BEEN ADVISED OF THE POSSIBILITY OF SUCH DAMAGES. THIS LIMITATION SHALL APPLY NOTWITHSTANDING ANY FAILURE OF ESSENTIAL PURPOSE OF ANY LIMITED REMEDY PROVIDED HEREIN.

- Should any provision of this Agreement be held by a court of competent jurisdiction to be illegal, invalid, or unenforceable, that provision shall be deemed amended to achieve as nearly as possible the same economic effect as the original provision, and the legality, validity and enforceability of the remaining provisions of this Agreement shall not be affected or impaired thereby.

- The failure of either party to enforce any term or condition of this Agreement shall not constitute a waiver of either party's right to enforce each and every term and condition of this Agreement. No breach under this agreement shall be deemed waived or excused by either party unless such waiver or consent is in writing signed by the party granting such waiver or consent. The waiver by or consent of a party to a breach of any provision of this Agreement shall not operate or be construed as a waiver of or

consent to any other or subsequent breach by such other party.

- This Agreement may not be assigned (including by operation of law or otherwise) by you without WILEY's prior written consent.
- Any fee required for this permission shall be non-refundable after thirty (30) days from receipt by the CCC.
- These terms and conditions together with CCC's Billing and Payment terms and conditions (which are incorporated herein) form the entire agreement between you and WILEY concerning this licensing transaction and (in the absence of fraud) supersedes all prior agreements and representations of the parties, oral or written. This Agreement may not be amended except in writing signed by both parties. This Agreement shall be binding upon and inure to the benefit of the parties' successors, legal representatives, and authorized assigns.
- In the event of any conflict between your obligations established by these terms and conditions and those established by CCC's Billing and Payment terms and conditions, these terms and conditions shall prevail.
- WILEY expressly reserves all rights not specifically granted in the combination of (i) the license details provided by you and accepted in the course of this licensing transaction, (ii) these terms and conditions and (iii) CCC's Billing and Payment terms and conditions.
- This Agreement will be void if the Type of Use, Format, Circulation, or Requestor Type was misrepresented during the licensing process.
- This Agreement shall be governed by and construed in accordance with the laws of the State of New York, USA, without regards to such state's conflict of law rules. Any legal action, suit or proceeding arising out of or relating to these Terms and Conditions or the breach thereof shall be instituted in a court of competent jurisdiction in New York County in the State of New York in the United States of America and each party hereby consents and submits to the personal jurisdiction of such court, waives any objection to venue in such court and consents to service of process by registered or certified mail, return receipt requested, at the last known address of such party.

WILEY OPEN ACCESS TERMS AND CONDITIONS

Wiley Publishes Open Access Articles in fully Open Access Journals and in Subscription journals offering Online Open. Although most of the fully Open Access journals publish open access articles under the terms of the Creative Commons Attribution (CC BY) License only, the subscription journals and a few of the Open Access Journals offer a choice of Creative Commons Licenses. The license type is clearly identified on the article.

The Creative Commons Attribution License

The Creative Commons Attribution License (CC-BY) allows users to copy, distribute and transmit an article, adapt the article and make commercial use of the article. The CC-BY license permits commercial and non-

Creative Commons Attribution Non-Commercial License

The Creative Commons Attribution Non-Commercial (CC-BY-NC)License permits use, distribution and reproduction in any medium, provided the original work is properly cited and is not used for commercial purposes.(see below)

Creative Commons Attribution-Non-Commercial-NoDerivs License

The Creative Commons Attribution Non-Commercial-NoDerivs License (CC-BY-NC-ND) permits use, distribution and reproduction in any medium, provided the original work is properly cited, is not used for commercial purposes and no modifications or adaptations are made. (see below)

Use by commercial "for-profit" organizations

Use of Wiley Open Access articles for commercial, promotional, or marketing purposes requires further explicit permission from Wiley and will be subject to a fee.

Further details can be found on Wiley Online Library
http://olabout.wiley.com/WileyCDA/Section/id-410895.html

Other Terms and Conditions:

v1.10 Last updated September 2015

Questions? customercare@copyright.com or +1-855-239-3415 (toll free in the US) or +1-978-646-2777.

Copyright Clearance Center Marketplace™

Royal Society of Chemistry - License Terms and Conditions

This is a License Agreement between Alison Bain ("You") and Royal Society of Chemistry ("Publisher") provided by Copyright Clearance Center ("CCC"). The license consists of your order details, the terms and conditions provided by Royal Society of Chemistry, and the CCC terms and conditions.

All payments must be made in full to CCC.

Order Date	25-Jan-2021	**Type of Use**	Republish in a thesis/dissertation
Order license ID	1092786-1		
ISSN	1364-548X	**Publisher**	ROYAL SOCIETY OF CHEMISTRY
		Portion	Chapter/article

LICENSED CONTENT

Publication Title	Chemical communications	**Country**	United Kingdom of Great Britain and Northern Ireland
Author/Editor	Royal Society of Chemistry (Great Britain)	**Rightsholder**	Royal Society of Chemistry
Date	01/01/1996	**Publication Type**	e-Journal
Language	English		

REQUEST DETAILS

Portion Type	Chapter/article	**Rights Requested**	Main product, any product related to main product, and other compilations/derivative products
Page range(s)	8928-8931		
Total number of pages	4		
Format (select all that apply)	Electronic	**Distribution**	Canada
Who will republish the content?	Academic institution	**Translation**	Original language of publication
Duration of Use	Life of current edition	**Copies for the disabled?**	No
Lifetime Unit Quantity	Up to 499	**Minor editing privileges?**	Yes
		Incidental promotional use?	No
		Currency	CAD

NEW WORK DETAILS

Title	The refractive index of single aerosol particles: Measurements and models	**Institution name**	McGill University
		Expected presentation date	2021-03-26
Instructor name	Alison Bain		

ADDITIONAL DETAILS

Order reference number	N/A	**The requesting person / organization to appear on the license**	Alison Bain

REUSE CONTENT DETAILS

Title, description or numeric reference of the portion(s)	The wavelength-dependent optical properties of weakly absorbing aqueous aerosol particles	**Title of the article/chapter the portion is from**	N/A
		Author of portion(s)	Alison Bain and Thomas C Preston
Editor of portion(s)	N/A	**Issue, if republishing an article from a serial**	N/A
Volume of serial or monograph	56		
Page or page range of portion	8928 - 8931	**Publication date of portion**	2020-06-26

PUBLISHER SPECIAL TERMS AND CONDITIONS

Permission is granted as long as the article is fully acknowledged and a link is given back to the article on our Platform. Please go to rsc.li/permissions for details. Please note that if the material specified above or any part of it appears with credit or acknowledgement to a third party then you must also secure permission from that third party before reproducing that material.

CCC Republication Terms and Conditions

1. Description of Service; Defined Terms. This Republication License enables the User to obtain licenses for republication of one or more copyrighted works as described in detail on the relevant Order Confirmation (the "Work(s)"). Copyright Clearance Center, Inc. ("CCC") grants licenses through the Service on behalf of the rightsholder identified on the Order Confirmation (the "Rightsholder"). "Republication", as used herein, generally means the inclusion of a Work, in whole or in part, in a new work or works, also as described on the Order Confirmation. "User", as used herein, means the person or entity making such republication.

2. The terms set forth in the relevant Order Confirmation, and any terms set by the Rightsholder with respect to a particular Work, govern the terms of use of Works in connection with the Service. By using the Service, the person transacting for a republication license on behalf of the User represents and warrants that he/she/it (a) has been duly authorized by the User to accept, and hereby does accept, all such terms and conditions on behalf of User, and (b) shall inform User of all such terms and conditions. In the event such person is a "freelancer" or other third party independent of User and CCC, such party shall be deemed jointly a "User" for purposes of these terms and conditions. In any event, User shall be deemed to have accepted and agreed to all such terms and conditions if User republishes the Work in any fashion.

3. Scope of License; Limitations and Obligations.

    3.1. All Works and all rights therein, including copyright rights, remain the sole and exclusive property of the Rightsholder. The license created by the exchange of an Order Confirmation (and/or any invoice) and payment by User of the full amount set forth on that document includes only those rights expressly set forth in the Order Confirmation and in these terms and conditions, and conveys no other rights in the Work(s) to User. All rights not expressly granted are hereby reserved.

    3.2. General Payment Terms: You may pay by credit card or through an account with us payable at the end of the month. If you and we agree that you may establish a standing account with CCC, then the following terms apply: Remit Payment to: Copyright Clearance Center, 29118 Network Place, Chicago, IL 60673-1291. Payments Due: Invoices are payable upon their delivery to you (or upon our notice to you that they are available to you for downloading). After 30 days, outstanding amounts will be subject to a service charge

of 1-1/2% per month or, if less, the maximum rate allowed by applicable law. Unless otherwise specifically set forth in the Order Confirmation or in a separate written agreement signed by CCC, invoices are due and payable on "net 30" terms. While User may exercise the rights licensed immediately upon issuance of the Order Confirmation, the license is automatically revoked and is null and void, as if it had never been issued, if complete payment for the license is not received on a timely basis either from User directly or through a payment agent, such as a credit card company.

3.3. Unless otherwise provided in the Order Confirmation, any grant of rights to User (i) is "one-time" (including the editions and product family specified in the license), (ii) is non-exclusive and non-transferable and (iii) is subject to any and all limitations and restrictions (such as, but not limited to, limitations on duration of use or circulation) included in the Order Confirmation or invoice and/or in these terms and conditions. Upon completion of the licensed use, User shall either secure a new permission for further use of the Work(s) or immediately cease any new use of the Work(s) and shall render inaccessible (such as by deleting or by removing or severing links or other locators) any further copies of the Work (except for copies printed on paper in accordance with this license and still in User's stock at the end of such period).

3.4. In the event that the material for which a republication license is sought includes third party materials (such as photographs, illustrations, graphs, inserts and similar materials) which are identified in such material as having been used by permission, User is responsible for identifying, and seeking separate licenses (under this Service or otherwise) for, any of such third party materials; without a separate license, such third party materials may not be used.

3.5. Use of proper copyright notice for a Work is required as a condition of any license granted under the Service. Unless otherwise provided in the Order Confirmation, a proper copyright notice will read substantially as follows: "Republished with permission of [Rightsholder's name], from [Work's title, author, volume, edition number and year of copyright]; permission conveyed through Copyright Clearance Center, Inc. " Such notice must be provided in a reasonably legible font size and must be placed either immediately adjacent to the Work as used (for example, as part of a by-line or footnote but not as a separate electronic link) or in the place where substantially all other credits or notices for the new work containing the republished Work are located. Failure to include the required notice results in loss to the Rightsholder and CCC, and the User shall be liable to pay liquidated damages for each such failure equal to twice the use fee specified in the Order Confirmation, in addition to the use fee itself and any other fees and charges specified.

3.6. User may only make alterations to the Work if and as expressly set forth in the Order Confirmation. No Work may be used in any way that is defamatory, violates the rights of third parties (including such third parties' rights of copyright, privacy, publicity, or other tangible or intangible property), or is otherwise illegal, sexually explicit or obscene. In addition, User may not conjoin a Work with any other material that may result in damage to the reputation of the Rightsholder. User agrees to inform CCC if it becomes aware of any infringement of any rights in a Work and to cooperate with any reasonable request of CCC or the Rightsholder in connection therewith.

4. Indemnity. User hereby indemnifies and agrees to defend the Rightsholder and CCC, and their respective employees and directors, against all claims, liability, damages, costs and expenses, including legal fees and expenses, arising out of any use of a Work beyond the scope of the rights granted herein, or any use of a Work which has been altered in any unauthorized way by User, including claims of defamation or infringement of rights of copyright, publicity, privacy or other tangible or intangible property.

5. Limitation of Liability. UNDER NO CIRCUMSTANCES WILL CCC OR THE RIGHTSHOLDER BE LIABLE FOR ANY DIRECT, INDIRECT, CONSEQUENTIAL OR INCIDENTAL DAMAGES (INCLUDING WITHOUT LIMITATION DAMAGES FOR LOSS OF BUSINESS PROFITS OR INFORMATION, OR FOR BUSINESS INTERRUPTION) ARISING OUT OF THE USE OR INABILITY TO USE A WORK, EVEN IF ONE OF THEM HAS BEEN ADVISED OF THE POSSIBILITY OF SUCH DAMAGES. In any event, the total liability of the Rightsholder and CCC (including their respective employees and directors) shall not exceed the total amount actually paid by User for this license. User assumes full liability for the actions and omissions of its principals, employees, agents, affiliates, successors and assigns.

6. Limited Warranties. THE WORK(S) AND RIGHT(S) ARE PROVIDED "AS IS". CCC HAS THE RIGHT TO GRANT TO USER THE RIGHTS GRANTED IN THE ORDER CONFIRMATION DOCUMENT. CCC AND THE RIGHTSHOLDER DISCLAIM ALL OTHER WARRANTIES RELATING TO THE WORK(S) AND RIGHT(S), EITHER EXPRESS OR IMPLIED, INCLUDING WITHOUT LIMITATION IMPLIED WARRANTIES OF MERCHANTABILITY OR FITNESS FOR A PARTICULAR PURPOSE. ADDITIONAL RIGHTS MAY BE REQUIRED TO USE ILLUSTRATIONS, GRAPHS, PHOTOGRAPHS, ABSTRACTS, INSERTS OR OTHER PORTIONS OF THE WORK (AS OPPOSED TO THE ENTIRE WORK) IN A MANNER CONTEMPLATED BY USER; USER UNDERSTANDS AND AGREES THAT NEITHER CCC NOR THE RIGHTSHOLDER MAY HAVE SUCH ADDITIONAL RIGHTS TO GRANT.

7. Effect of Breach. Any failure by User to pay any amount when due, or any use by User of a Work beyond the scope of the license set forth in the Order Confirmation and/or these terms and conditions, shall be a material breach of the license created by the Order Confirmation and these terms and conditions. Any breach not cured within 30 days of written notice thereof shall result in immediate termination of such license without further notice. Any unauthorized (but licensable) use of a Work that is terminated immediately upon notice thereof may be liquidated by payment of the Rightsholder's ordinary license price therefor; any unauthorized (and unlicensable) use that is not terminated immediately for any reason (including, for example, because materials containing the Work cannot reasonably be recalled) will be subject to all remedies available at law or in equity, but in no event to a payment of less than three times the Rightsholder's ordinary license price for the most closely analogous licensable use plus Rightsholder's and/or CCC's costs and expenses incurred in collecting such payment.

8. Miscellaneous.

    8.1. User acknowledges that CCC may, from time to time, make changes or additions to the Service or to these terms and conditions, and CCC reserves the right to send notice to the User by electronic mail or otherwise for the purposes of notifying User of such changes or additions; provided that any such changes or additions shall not apply to permissions already secured and paid for.

    8.2. Use of User-related information collected through the Service is governed by CCC's privacy policy, available online here:https://marketplace.copyright.com/rs-ui-web/mp/privacy-policy

    8.3. The licensing transaction described in the Order Confirmation is personal to User. Therefore, User may not assign or transfer to any other person (whether a natural person or an organization of any kind) the license created by the Order Confirmation and these terms and conditions or any rights granted hereunder; provided, however, that User may assign such license in its entirety on written notice to CCC in the event of a transfer of all or substantially all of User's rights in the new material which includes the Work(s) licensed under this Service.

    8.4. No amendment or waiver of any terms is binding unless set forth in writing and signed by the parties. The Rightsholder and CCC hereby object to any terms contained in any writing prepared by the User or its principals, employees, agents or affiliates and purporting to govern or otherwise relate to the licensing transaction described in the Order Confirmation, which terms are in any way inconsistent with any terms set forth in the Order Confirmation and/or in these terms and conditions or CCC's standard operating procedures, whether such writing is prepared prior to, simultaneously with or subsequent to the Order Confirmation, and whether such writing appears on a copy of the Order Confirmation or in a separate instrument.

    8.5. The licensing transaction described in the Order Confirmation document shall be governed by and construed under the law of the State of New York, USA, without regard to the principles thereof of conflicts of law. Any case, controversy, suit, action, or proceeding arising out of, in connection with, or related to such licensing transaction shall be brought, at CCC's sole discretion, in any federal or state court located in the County of New York, State of New York, USA, or in any federal or state court whose geographical jurisdiction covers the location of the Rightsholder set forth in the Order Confirmation. The parties expressly submit to the personal jurisdiction and venue of each such federal or state court.If you have any comments or questions about the Service or Copyright Clearance Center, please contact us at 978-750-8400 or send an e-mail to support@copyright.com.

v 1.1